EXPERIMENTAL INVESTIGATION AND COMPUTATIONAL MODELING OF VOIDS IN ADDITIVELY MANUFACTURED FUSED DEPOSITION MODELLING PARTS

BY

MOSA EISSA ALMUTAHHAR

A Thesis Presented to the

COLLEGE OF GRADUATE AND INTERDISCIPLINARY STUDIES

KING FAHD UNIVERSITY OF PETROLEUM & MINERALS

DHAHRAN, SAUDI ARABIA

In Partial Fulfillment of the
Requirements for the Degree of

MASTER OF SCIENCE

In

MECHANICAL ENGINEERING

MAY 2024

KING FAHD UNIVERSITY OF PETROLEUM & MINERALS

DHAHRAN- 31261, SAUDI ARABIA

DEANSHIP OF GRADUATE STUDIES

This thesis, written by **MOSA EISSA ALMUTAHHAR** under the direction of his thesis advisor and approved by his thesis committee, has been presented and accepted by the Dean of Graduate Studies, in partial fulfillment of the requirements for the degree of **MASTER OF SCIENCE IN MECHANICAL ENGINEERING.**

Dr. Usman Ali
(Advisor)

Dr. Mohammed Antar
Department Chairman

Dr. Jafar Albinmousa
(Member)

Dr. Suliman Al-Homidan
Dean of Graduate Studies

Dr. Abba Abubakar
(Member)

Date: May 2024

I dedicate this thesis to my beloved mother, whose unwavering love, encouragement, and sacrifices have been the guiding light throughout my academic journey. Her boundless support and belief in my abilities has fueled my determination to pursue excellence in every endeavor. From the earliest days of my education to the culmination of this thesis, her strength, wisdom, and enduring faith have been my greatest sources of inspiration. This thesis is a tribute to her enduring presence in my life, and I am forever grateful for her selfless devotion and endless love.

ACKNOWLEDGMENTS

I am deeply grateful to my family and friends whose unwavering support and encouragement have been instrumental in my academic journey. To my parents, brothers, and sisters, your love, guidance, and belief in my abilities have been my constant source of strength. Special thanks to my uncle, Dr. Faisal Almutahhar, for his mentorship and continuous support. Also, to my uncle Mr. Mohammed Almutahhar for his continuous support. In addition, I extend my heartfelt thanks to my dear friend, Engr. Abdulatif Alobaidan, for his constant encouragement and support during challenging times.

I extend my heartfelt appreciation to my advisor, Dr. Usman Ali, for his guidance, mentorship, and invaluable insights that have shaped this thesis. His expertise, patience, and unwavering support have been instrumental in my academic growth and success. In addition, I would like to express my gratitude to my committee members, Dr. Jafar Albinmousa and Dr. Abba Abubakar, for their valuable feedback, constructive criticism, and insightful suggestions that have enriched this thesis.

Special thanks to my collaborators in the lab work, Engr. Abdullah Almohammadali, Engr. Mohammed Abdulazim, and Engr. Abdulaziz Almudara, for their dedication and assistance. I am also grateful to our research group members, Tarig Mekki, Mohammed Shammu, Ali Alhajeri, and Areumu, for their collaboration, support, and valuable contributions to our collective endeavors.

Finally, I would like to acknowledge the support and resources provided by King Fahd University of Petroleum and Minerals (KFUPM). The conducive academic environment and opportunities for research and learning at KFUPM have been invaluable in shaping my academic and professional journey.

TABLE OF CONTENT

LIST OF FIGURES

LIST OF TABLES

LIST OF ABBREVIATIONS

ABS	Acrylonitrile Butadiene Styrene
AM	Additive Manufacturing
BJT	Binder Jetting
CAD	Computer Aided Design
CT	Computed Tomography
DED	Directed Energy Deposition
DLP	Digital Light Processing
E	Young’s Modulus
EB	Elongation at Break
FDM	Fused Deposition Modeling
FEA	Finite Element Analysis
FEM	Finite Element Methods
GT	Gurson-Tvergaard plasticity model
LOM	Laminated Object Manufacturing
MEX	Material Extrusion
MJF	Multi-jet Fusion
OM	Optical microscopy
PEEK	Polyether Ether Ketone
PLA	Polylactic Acid
RVE	Representative Volume Element
UAM	Ultrasonic Additive Manufacturing
VPP	Vat Photopolymerization
YS	Yield Strength

ABSTRACT

Full Name : Mosa Eissa Almutahhar

Thesis Title : Experimental Investigation and Computational Modeling of Voids in Additively Manufactured Fused Deposition Modeling Parts

Major Field : Mechanical Engineering

Date of Degree : May 2024

Additive Manufacturing (AM) has revolutionized modern manufacturing by enabling the fabrication of complex geometries with unprecedented flexibility and efficiency. Among the various AM techniques, FDM stands out for its widespread use owing to its affordability and ease of operation. However, FDM parts often exhibit inherent defects such as porosities, which can significantly impact their mechanical properties. This thesis investigates the influence of infill density on void formation and its effects on the mechanical properties of FDM parts through a combination of experimental, analytical, and computational analyses. PLA FDM samples with varying infill densities were manufactured and characterized to assess the part microstructures. Tensile testing was then conducted to analyze the mechanical properties of printed PLA FDM parts. A new analytical model was also proposed and compared to conventional analytical models to predict the stiffness of FDM porous parts. Various 2D and 3D computational models were developed to capture the tensile behavior of FDM parts based on dense and porous structures.

ملخص الرسالة

الاسم الكامل : موسى بن عيسى المطهر

عنوان الرسالة : دراسة تجريبية ونمذجة حوسبية للفجوات في الأجزاء المصنعة بالتصنيع الإضافي بواسطة تقنية النمذجة بالترسيب المنصهر

التخصص : الهندسة الميكانيكية

تاريخ الدرجة العلمية: مايو 2024

التصنيع بالإضافة قد غيّر مفهوم التصنيع الحديث من خلال تمكين تصنيع أشكال معقدة بمرونة وكفاءة لا مثيل لهما. ومن بين تقنيات التصنيع بالإضافة المتنوعة، تبرز تقنية النمذجة بالترسيب المنصهر نظرًا لانتشار استخدامها الواسع بفضل تكلفتها المنخفضة وسهولة تشغيلها. ومع ذلك، تظهر الأجزاء المصنعة بتقنية النمذجة بالترسيب المنصهر في كثير من الأحيان عيوبًا متأصلة مثل التجويفات، التي من الممكن أن تؤثر بشكل كبير على الخصائص الميكانيكية لهذه الأجزاء. تهدف هذه الأطروحة البحثية إلى استكشاف تأثير كثافة التعبئة على تكون التجويفات وتأثيرها على الخصائص الميكانيكية للأجزاء المصنعة بتقنية النمذجة بالترسيب المنصهر من خلال مجموعة من التحقيقات التجريبية و النماذج التحليلية و الحوسبية. تم تصنيع عينات باستخدام حمض البوليلاكتيك بكثافات تعبئة متفاوتة وتم توصيفها باستخدام مجهر المسح بالالكترونات لتقييم هياكلها الدقيقة. تم من ثم إجراء اختبار الشد لتحليل الخصائص الميكانيكية للأجزاء المطبوعة باستخدام حمض البوليلاكتيك. وقد تمت مقارنة نموذج تحليلي جديد مقترح في هذا البحث بنماذج تحليلية تقليدية لتوقع صلابة الأجزاء المسامية المصنعة بتقنية النمذجة بالترسيب المنصهر. وتم تطوير مجموعة من النماذج الحوسبية ثنائية وثلاثية الأبعاد لتصوير سلوك الأجزاء المصنعة بتقنية النمذجة بالترسيب المنصهر خلال ظروف الشد استنادًا على هياكل كثيفة ومسامية.

CHAPTER 1

INTRODUCTION

1.1 Background

Additive Manufacturing (AM) refers to the process of creating objects by adding successive layers of material to achieve the final shape. Currently, AM parts are utilized in various industries such as aerospace, healthcare, and oil & gas where the reliability of the AM parts is a significant factor of interest [1]. These high-end industries require standardized quality measures and certifications for critical applications. However, AM parts are not the first choice for many industries due to inherent process defects observed in AM parts [2]. As a result, researchers have focused on optimizing the process parameters by studying the relationship between the process-structure-properties of AM parts to reduce defects and increase the reliability of AM components. Optimization of the process-structure-property relationships involves various factors, such as the choice of material, the printing process, and post-processing procedures and therefore requires a systematic approach to achieve defect free parts [3].

There are several different classifications of AM, including PBF, BJT, DED, VPP, MJT, SHL, and MEX [4]. MEX, which is commonly known as FDM, is a widely used method that works by extruding, typically, a thermoplastic material through a nozzle and depositing it layer-by-layer to build the final object. FDM is particularly popular due to its relatively low cost and ease of use, making it accessible to a wide range of individual users as well as industrial manufacturers.

Tensile properties are of paramount importance in engineering and design as they provide information about materials strength and deformation behavior under tensile loads. As AM parts are built layer-by-layer, each layer's mechanical properties affect the overall product strength and durability [5]**.** YS, UTS, E, and elongation at break are some of the critical factors in the selection of suitable materials for AM applications. Additionally, tensile properties are influenced by the choice of AM processing parameters [6]. Hence, optimizing the process parameters mitigates the alteration of the desired feedstock material properties [7]**.** For instance, process-based porosities are inherent in AM parts, and they affect the mechanical properties and therefore require careful examination. Various researchers reported a deterioration in the quasi-static properties of FDM parts due to the presence of voids [8], [9], [10], [11]**.** Therefore, understanding the effect of voids on the mechanical properties is essential to ensure the structural integrity and reliability of the FDM parts.

Researchers have used various experimental and computational techniques such as FEA, and analytical models to study the mechanical properties of FDM parts [12], [13], [14]. Although experimental approaches are commonly used for their accuracy and reliability, they require extensive studies with enormous amounts of time and financial resources. In contrast, computational modeling and simulation techniques allow an efficient option to analyze the effect of voids in FDM parts [15]. As pores are one of the most commonly found defects in FDM parts, they act as stress risers and omitting their effect can lead to unrealistic simulation results [3]. However, most of the simulation models neglect pores and assume a full dense FDM part [9].

In this work, the tensile properties of FDM parts with in-built voids were analyzed using numerical (FEA) and analytical models. PLA FDM samples with varying voids levels were printed to analyze the material defects and response under tensile loading. Next, the FEM models were verified and validated with experimental results. Models for both 2D and 3D full-dense and porous parts were generated to study the effect of voids on tensile properties. Analytical approaches were also used to predict the performance of printed parts. The formulated effective tensile properties of the porous structure were then used in the material definition of the generated FEA models to facilitate the numerical simulations. The proposed work could be used as a framework to assure a reliable computational and analytical model for AM parts that accounts for internal defects such as porosity.

1.2 Motivation

Creating an accurate model to predict the mechanical properties of FDM parts presents several challenges and research gaps due to the complexity of the FDM process. Numerical models involving detailed process–structure-property relationships require extensive simulations to account for the voids present in AM parts. In addition, the physical phenomena used to describe these processes are not available. Therefore, most predictive models adopt model assumptions to simplify the problem resulting in inaccurate predictions. Therefore, efficient computational design tools are needed at multiple time and length scales.

FEM models can provide higher accuracy compared to analytical models, but require extensive resources. On the other hand, analytical models provide fast solutions, but a definitive analytical model that relates the material porosity to its mechanical properties has yet to be developed [16]. Therefore, current analytical models are unable to provide accurate predictions. Overall, there is a lack of numerical and analytical models that provide a link between the voids and mechanical properties of FDM parts.

1.3 Objectives

This thesis aims to investigate the impact of infill density on void formation and tensile properties of FDM PLA parts. Various 2D and 3D FEA computational models will be developed and validated with experimental results. Through a systematic approach, this study seeks to provide insights into optimizing the infill density for improved part quality and mechanical performance in FDM processes per the following objectives:

I. To enhance the quality of FDM parts by investigating the influence of infill density on tensile properties.

II. To study and propose analytical models that can predict the mechanical properties of FDM parts while accounting for voids presence.

III. To develop a 2D and 3D modeling framework that integrates analytical and computational methods to predict the tensile properties of FDM parts with varying infill densities.

1.4 Methodology

The methodology employed in this work combines experimental, analytical, and computational analyses to comprehensively study the impact of voids on the mechanical properties of FDM parts. Initially, PLA FDM samples with varying infill densities were manufactured to represent different levels of porosity. SEM analysis was utilized to assess the microstructures of the printed samples. Subsequently, the printed parts were tested under tensile loads to analyze their mechanical properties.

Various existing analytical models from literature were evaluated to predict the effect of porosity on part stiffness. These models were assessed across different porosity levels and served as a guide to propose a new analytical model with improved capabilities. The proposed model was verified with experimental results and showed good agreement.

In the computational modeling phase, material models were developed to capture the mechanical behavior of FDM parts. Both 2D and 3D geometrical models representing dense and porous structures were created. Several modeling approaches were employed to simulate the tensile response of FDM components with infill densities ranging between 50% to 100%.

The integrated methodology presented in this work combines experimental data from physical tests with analytical predictions and computational simulations to provide a comprehensive understanding of the mechanical properties of FDM parts (**Figure 1.1)**. By leveraging these approaches, the effects of processing parameters, material properties, and geometrical considerations on the final mechanical performance of the printed parts can be investigated thoroughly.

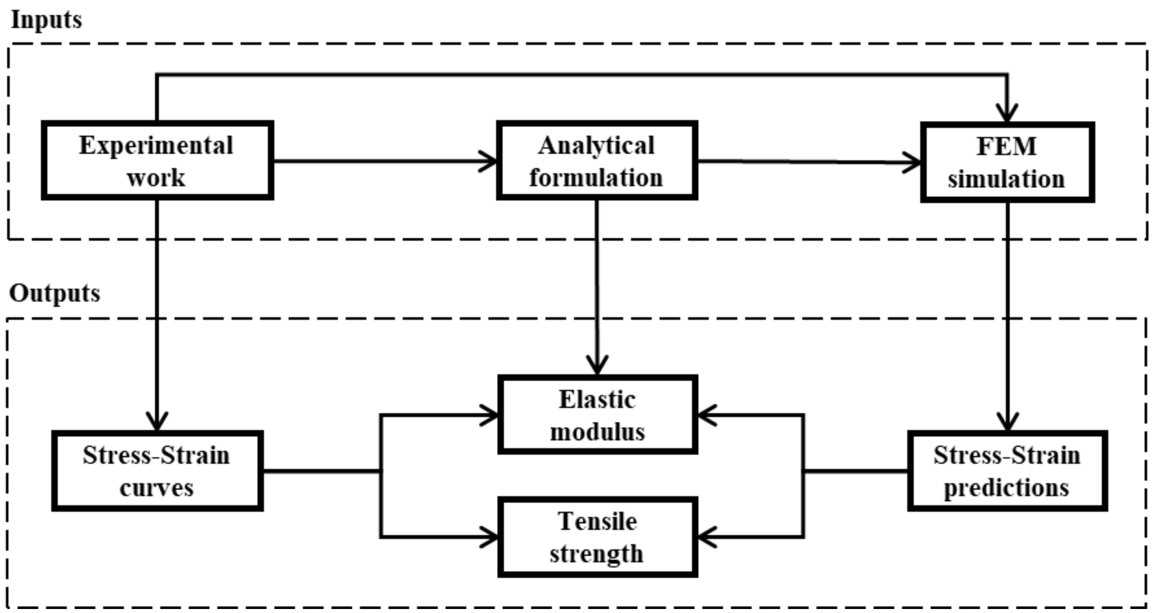

Figure 1.1: Graphical representation of the methodology followed in this thesis.

CHAPTER 2

LITERATURE REVIEW

2.1 Additive Manufacturing (AM)

AM has undergone a significant transformation in the last three decades and is considered a key enabler of Industry 4.0 [17]. This manufacturing process involves creating a three-dimensional object by adding layers of material to achieve the final part (ISO/ASTM 52900:2021) [4]. The typical AM process cycle, illustrated in **Figure 2.1**, involves several sequential steps. The first phase entails conceptualization and computer-aided design (CAD), wherein engineering CAD software are utilized to create the digital model of the intended part. Alternatively, reverse engineering methods can also be employed [18]. Following conceptualization, the digital model is transformed into the STL/AMF file format. Preprocessing is then employed to segment the object into slices that are suitable for AM machines. Additionally, these preprocessing tools generate support structures to maintain the desired geometries during the AM process. Subsequently, the STL/AMF file is transferred as a G-code file on the AM machine. Finally, the manufacturing of the part commences, followed by the removal of the finished part and subsequent post-processing, which includes cleanup activities to refine the manufactured component.

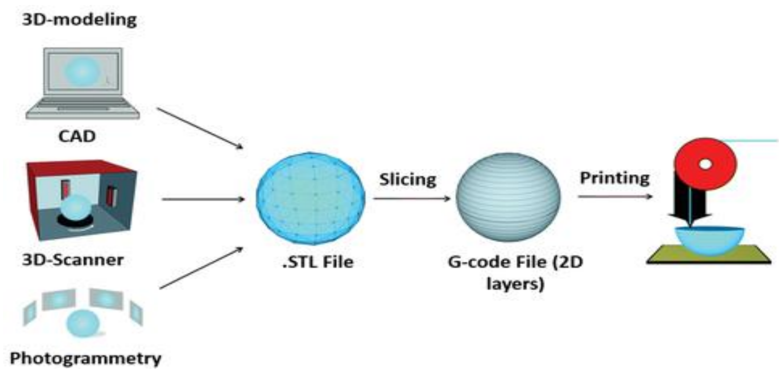

Figure 2.1: AM generic process cycle [19].

AM has been adopted in various industries and is being used for various applications due to design flexibility, reduced lead times and production of complex geometries [20]**.** Prototyping, product customization, and low-volume manufacturing are some of the most common uses for AM components [21]. In addition, the flexibility to use multiple types of materials has pushed AM as one of the most promising technologies for the future. As a result, AM has become increasingly popular in various industries, including aerospace [22], automotive [23], medical [24], and consumer goods [18].

2.1.1 Process classifications

The ISO/ASTM 52900:2021 standard categorizes all available AM processes into seven groups. These categories are DED, VPP, PBF, BJT, MJT, SHL, and MEX [4]. Each of these categories involves specific techniques and methods for creating three-dimensional objects by adding layers of material, as described below:

(a) Directed Energy Deposition (DED)

In this process, a focused energy source, such as a laser or electron beam, is used to melt and deposit powder or wire onto a substrate. Before melting, the feedstock material is fed through a nozzle [25]. **Figure 2.2** illustrates the working principle of DED process. DED is often used for repairing or for manufacturing large-scale structures. Examples of DED processes include laser metal deposition (LMD) [26] and laser engineered net shaping (LENS) [27].

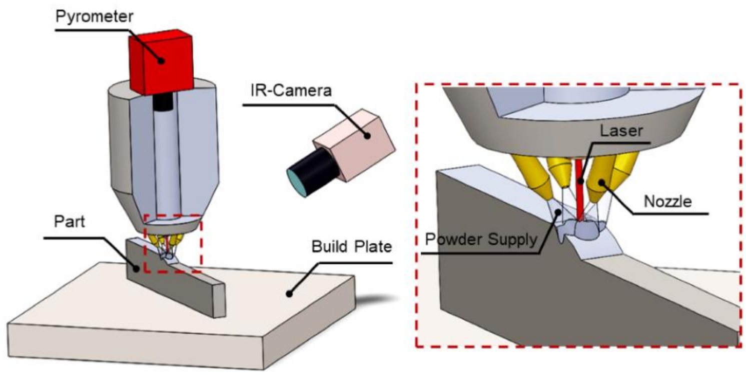

Figure 2.2: Working principle of DED process [25].

(b) Vat Photopolymerization (VPP)

This process uses a reservoir of liquid photopolymer that is selectively cured by a light source, such as a laser or a projector, to form the desired shape. VPP processes are commonly used for high-resolution parts, such as dental implants or jewelry. Examples of VPP processes include stereolithography (SLA) [17] and digital light processing (DLP) [28]. **Figure 2.3** shows the working principle for both SLA and DLP techniques.

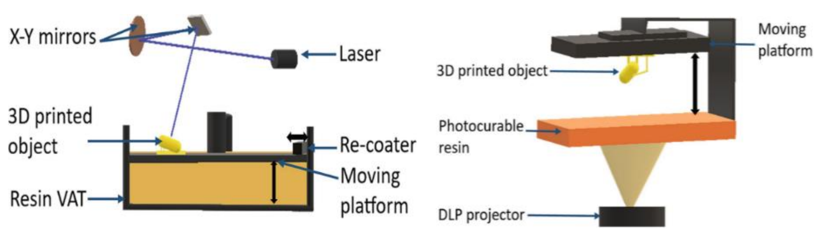

Figure 2.3: Working principle of VPP process for both SLA and DLP techniques [17].

(c) Powder-bed Fusion (PBF)

This process uses a powder-bed that is selectively fused together by a heat source, such as a laser or an electron beam, to create the desired part. The feedstock could be a metal or polymer powder [29]. **Figure 2.4** gives a basic representation of the PBF printing process. PBF processes are used for creating complex geometries with high accuracy and strength

[30]. Examples of PBF processes include laser powder-bed fusion (LPBF) [31], selective laser sintering (SLS) [32] and electron beam melting (EBM) [33].

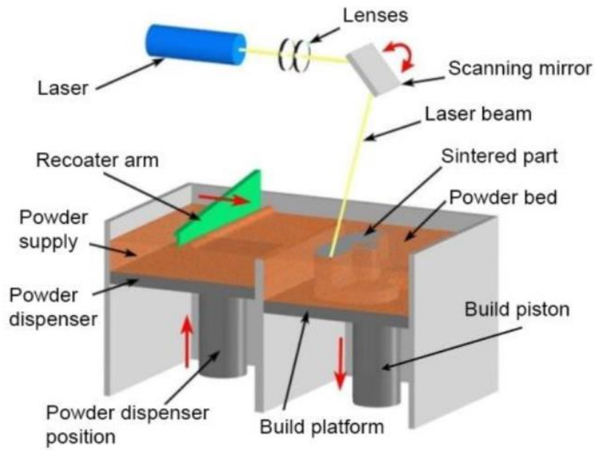

Figure 2.4: Basic representation of the PBF printing process [34].

(d) Binder Jetting (BJT)

This technology uses a powder material that is selectively bonded together by a liquid binder to create the desired shape. This process can also be used to manufacture metal and ceramic parts [30]. **Figure 2.5** illustrates the general schematic of the BJT printing process. BJT is commonly used for creating parts with high complexity and customization. Due to its low cost and high production rates, BJT is one of the most promising AM methods for mass-production [35].

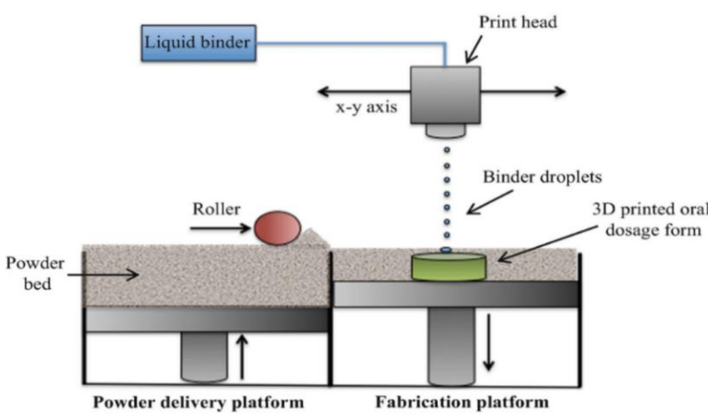

Figure 2.5: General schematic of the BJT printing process [35].

(e) Material Jetting (MJT)

MJT process uses a print head to deposit droplets of liquid material, such as wax or resin, that are then cured to form the desired shape [36]. The working principle is shown in **Figure 2.6** for MJT process. MJT processes are commonly used for creating high-resolution parts with complex geometries [29]. Examples of MJT processes include Polyjet fusion [37], and multi-jet fusion (MJF) [38].

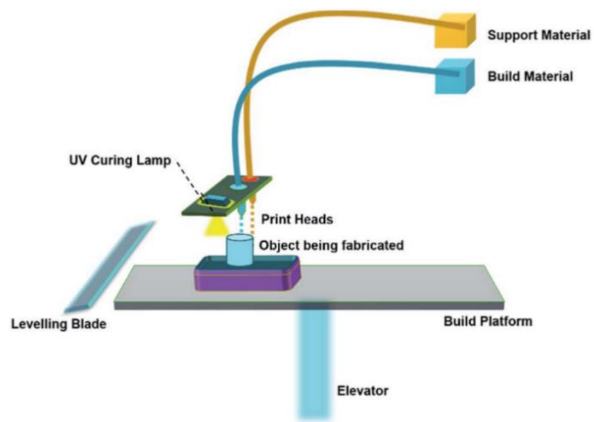

Figure 2.6: Working principle of MJT process [36].

(f) Sheet Lamination (SHL)

Unlike other AM technologies, SHL does not use a liquid or powder material as a feedstock material. Instead, SHL starts with thin sheets of material, such as paper, polymer, or metal foil, which are layered on top of each other and bonded together using an adhesive or heat. The layers are then cut or trimmed to achieve the final part [30]. SHL processes are commonly used for creating large scale models or prototypes [39]. Examples of SHL processes include laminated object manufacturing (LOM) [40] and ultrasonic AM (UAM) [41]. The basic working principle of SHL process is illustrated in **Figure 2.7**.

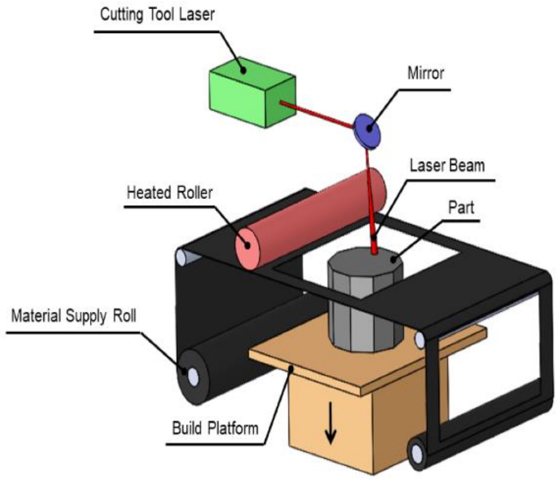

Figure 2.7: Working principle of SHL process [25].

(g) Material Extrusion (MEX)

MEX process uses a polymeric filament that is heated and extruded through a nozzle to create the desired shape [25]. **Figure 2.8** shows the working principle of MEX process. MEX processes are commonly used for creating large-scale parts or prototypes with low complexity [42]. The most common example of MEX processes is fused deposition modeling (FDM) [43].

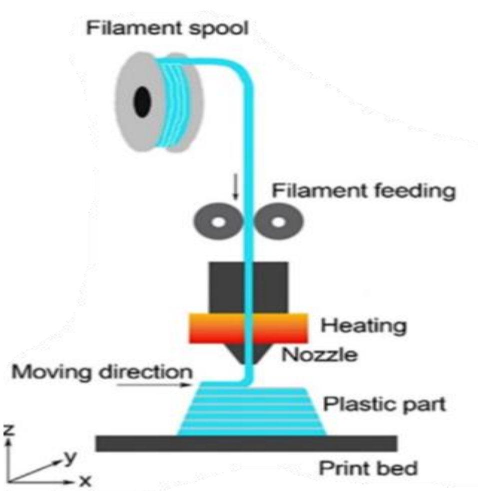

Figure 2.8: Working principle of MEX/FDM process [44].

2.1.2 Feedstock materials

AM Feedstock materials for the seven AM processes discussed previously can be delivered as resin [45], powder [46], wire [47], filament [48], and sheets [49]. The materials used in AM can be broadly classified into four categories: polymers, metals, ceramics, and composites [29]. Each category exhibits a unique set of properties and characteristics that make it suitable for specific applications. Polymers are the most commonly used materials in AM due to their low cost, flexibility, and ease of use [50]. Metals are ideal for producing high-strength, temperature-resistant parts with excellent mechanical properties [22]. Ceramics offer high-temperature stability, chemical resistance, and excellent electrical insulation properties [29]. Composites are used to create lightweight, high-strength parts with unique properties [23]. However, as AM technology continues to evolve, new materials are being developed rapidly.

2.1.3 Quality control and standardization

Reliability and repeatability are one of the biggest challenges for AM parts. Ensuring consistent quality allows the use of AM parts in various industries [1]. To address this challenge, quality control and standardization have become important areas of research [2]. Quality control in AM involves monitoring and controlling the manufacturing process to ensure that parts meet the required specifications. Several methods have been developed for quality control in AM. In-process monitoring has been adopted in several AM processes to study the temperature, pressure, and laser power to detect in-process issues [3]. Post-processing inspections are also conducted to study manufacturing defects. This can be done through various methods such as OM, X-ray CT, and SEM [14]. Lastly, non-destructive approaches such as ultrasonic testing, eddy current testing, and radiographic testing can also be used to study the part quality during operation [51].

Standardization involves developing guidelines and procedures as well as standards and certifications that ensure consistent quality of AM parts. Various standards have been developed for various aspects of the AM process, including design, materials, and manufacturing processes [1]. ISO/ASTM 52900 provides a framework for the entire AM process from design to post-processing. This standard covers various aspects of AM, including design rules, material properties, machine calibration, and post-processing. Other standards include ASTM F42, which cover various aspects of AM such as design, materials, and process control. ASME Y14.46 provides guidelines for the design of AM parts [29]. These standards were used in literature to refer to AM definitions, classifications, and methodologies [52]-[54].

ASTM and ISO also have a wide range of standards for mechanical testing of polymers. These standards cover various aspects of mechanical testing, such as tensile, compressive, flexural, shear, impact, and fatigue testing. These standards are essential for evaluating the performance of materials and ensuring their quality and safety in various applications as well as the reproducibility across different laboratories and testing facilities [50].

2.2 Fused Deposition Modeling (FDM)

FDM, commonly known as MEX, stands as the predominant and widely adopted AM method for the production of polymer-based products due to its versatility and cost-effectiveness [42]. In this process, a movable head deposits molten material onto a substrate, typically from a thermoplastic polymer filament [43]. Stratasys, Ultimaker, MakerBot, Ender and Rais3D are the most popular FDM manufacturers [29].

In FDM, the material is heated to a temperature slightly above its melting point within the print head and extruded through a nozzle on a substrate, where it solidifies and forms a layer [30]. The heating process in the nozzle ensures that the polymer is in a malleable state during extrusion but solidifies almost instantly upon deposition. This rapid solidification process is crucial for maintaining the structural integrity of the printed object. The process is repeated until the part is completed (**Figure 2.9**). Recently, multi-nozzle FDM systems have been developed that can create objects with unique properties as each nozzle deposits a different material [55].

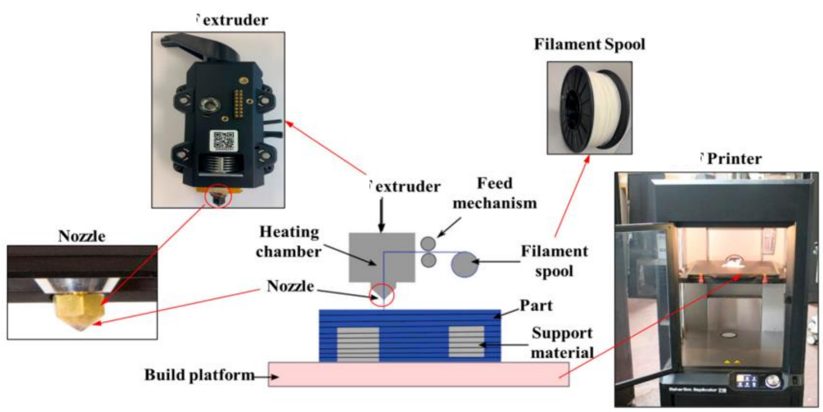

Figure 2.9: FDM printer components [12].

The success of the FDM process is contingent on the careful management of various printing parameters. Parameters such as layer thickness, printing orientation, raster angle, air gaps, and infill density play a vital role in determining the overall quality of the printed objects [6]. Other process parameters such as printing speed, extrusion rate, nozzle temperature, and the inherent properties of the polymers also affect the FDM process [56].

The intricate interplay of these variables highlights the need for a comprehensive understanding to achieve optimal outcomes in FDM process and emphasizes the continual need for research and development to refine the quality assurance framework for FDM technology.

2.2.1 Feedstock materials

Being a widely recognized AM technique, the FDM process employs thermoplastic filaments [57]. Furthermore, beyond utilizing pure thermoplastics, there is a growing interest in the use of composite filaments, particularly polymer matrix composites [43]. Exploring the combination of various reinforcements, including particles, nanoparticles, and fibers, with thermoplastics to create innovative composite filaments is an emerging trend in FDM research [58]. This has captured the attention of both researchers and industrial experts, highlighting the potential of composite materials in FDM due to their distinct properties and cost-effectiveness [59]. Bioplastics have also been used in FDM and various biomaterials have been documented in literature as suitable FDM feedstock materials [60].

The primary focus of this research revolves around comprehending the fundamental aspects and computational modeling of voids and their impact on the strength of FDM parts. The investigation specifically examines a commonly used pure thermoplastic material. The most commonly used FDM materials used in literature include thermoplastics such as ABS, PLA, PETG (Polyethylene Terephthalate Glycol), and Nylon [59]. ABS is a strong, durable material that is commonly used in automotive and industrial applications [61]. PLA is a biodegradable material that is used for its ease of manufacturing [62]. PETG is a flexible and tough material that is widely used in packaging and consumer products

[63]. Nylon is a strong and flexible material that is ideal for producing functional parts with high wear resistance [56]. In addition to these materials, special materials such as PEEK [60], HIPS (High impact polystyrene), and other materials are also used in literature [59].

2.2.2 Process parameters

As with other AM technologies, FDM process is affected by process parameters as they control the final part quality and mechanical properties. The mechanical properties and dimensional accuracy play vital roles in the reliance of printed FDM parts. Hence, understanding the effect of process parameters is essential for AM design. The most important process parameters with their effects on the quality of FDM parts are described below:

(a) Build orientation

The build orientation, defined as the positioning of a part relative to the horizontal axis of the build platform, is a crucial factor in FDM. Typically, the build platform is considered to be the x-y plane, with the z-axis denoting the height of the printed parts [64]. When selecting the printing orientation for a component, choices include flat, on-edge, or upright (**Figure 2.10**). The impact of build orientation on mechanical properties is notable, with flat and on-edge printing yielding significantly stronger samples compared to upright orientation for most of the thermoplastics including ABS and PLA [58], [65]. Durgun and Ertan [66] attribute the weakened performance of upright samples to the predominant load being borne across printed layers rather than along the length of the rasters. The inter-layer fusion bonds that connect adjacent layers exhibit much lower strength compared to the trans-raster strength along the length of the rasters, resulting in a substantial decrease in strength for samples printed in the upright direction [67].

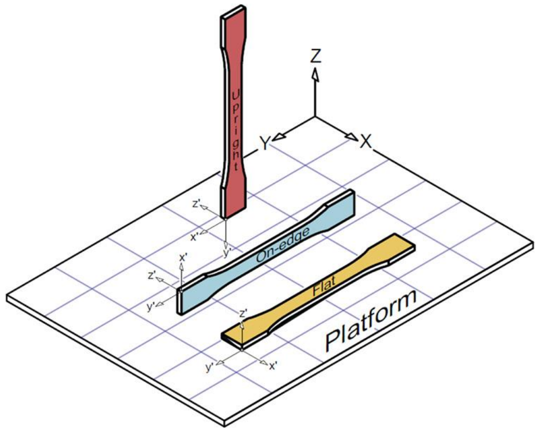

Figure 2.10: Build orientations in FDM [67].

(b) Layer thickness

During the printing process, the layer thickness influences the height of each printed layer and the time taken to complete the final part [64]. This parameter, closely associated with the build orientation of the printed component, plays a crucial role in achieving optimal surface roughness [68]. The influence of layer thickness on the strength of FDM parts has been studied extensively. Literature indicates that an increase in layer thickness results in a decrease in tensile strength for both PLA and ABS filaments [69]-[71] . This phenomenon is attributed to the compression of molten plastic extruded from the nozzle, causing deformation from a cylindrical to an oval shape, as shown in **Figure 2.11**. The compression of the molten plastic enhances fusion through increased contact area and bonding width, resulting in higher strength [72].

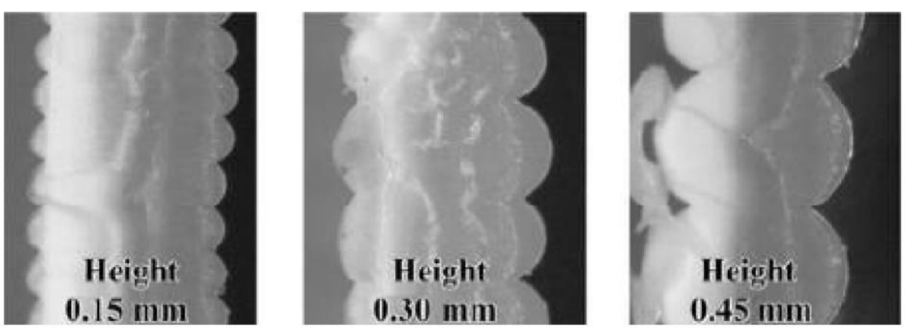

Figure 2.11: Effect of layer thickness on contact area [72].

Conversely, a direct correlation was observed between the impact resistance and enhancement in compressive strength with larger layer thicknesses [70]. However, this relationship may not hold true for low infill density parts due to large voids that may result in a potential reduction in compressive strength [59].

(c) Raster angle

The raster angle, referring to the orientation of the extruded filament during the layer-by-layer construction in the FDM process, plays a crucial role in the quality of FDM parts (**Figure 2.12**) [64]. Raster angle is typically adjustable to print at a fixed angle or alternate between angles for each layer to increase the quality of printed parts [69].

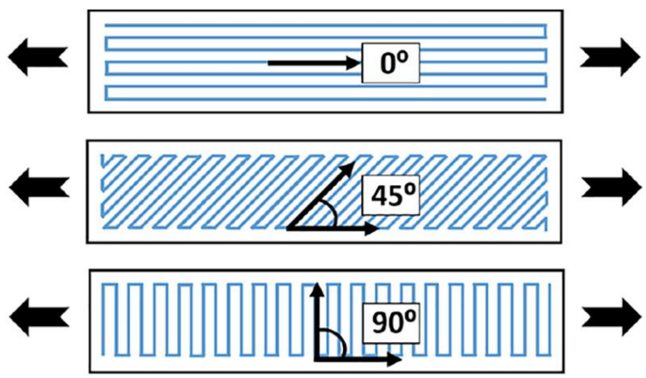

Figure 2.12: Raster angle and pattern (blue lines) in FDM parts. The black arrows identify the direction of tensile loading [64].

Notably, research on ABS suggested that a minimum raster angle of 0° enhanced the tensile strength of FDM parts, while a 45°/-45° (staggered raster) improved the impact strength [73]. Extending this understanding to PLA, Afrose et al. [74] discovered that a 0° raster angle resulted in the highest UTS, followed by 45° and then 90°. The alignment of the tensile load along the rasters was identified as the primary factor contributing to the superior tensile performance of parts printed with 0° rasters [64]. This observation was supported by Wu et al. [75], who demonstrated enhanced strength in PEEK when printed with a 0° raster angle, and Hill and Haghi [76], who drew similar conclusions for Polycarbonate samples.

(d) Air gaps and raster width

Certain printing parameters, such as air gap and raster width, can exert comparable influences on the resulting printed specimens [68]. In the printing process, the designated air gap represents the distance maintained between the deposited rasters, while the raster width specifies the width of the deposited rasters (**Figure 2.13**). It is essential to optimize these two variables collectively to achieve the desired overlap or gap between neighboring rasters. Moreover, the selection of raster angles also influences air gaps levels [64].

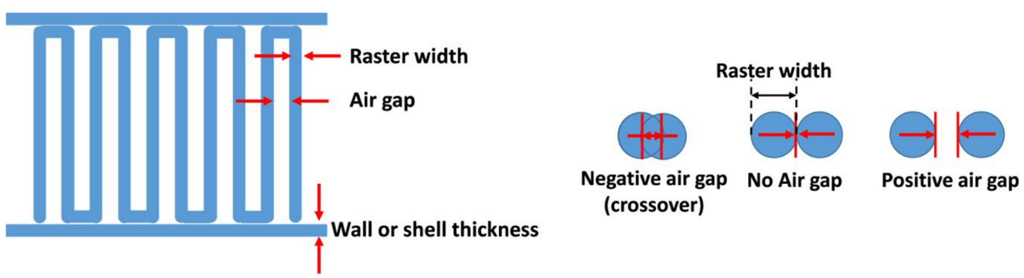

Figure 2.13: Air gap and raster width in FDM printing [64].

Rezayat et al. [77] explored the impact of various factors on the tensile strength of ABS samples with three air gaps (-0.05 mm, 0.0 mm, and 0.05 mm). They observed that an increase in the air gap resulted in a reduction in the UTS of the printed samples. Notably, an air gap of -0.05 mm consistently exhibited the highest strength across all raster angles due to its positive influence on bonding between adjacent rasters [78]. The negative air gap facilitated enhanced bonding, thereby improving the UTS at all raster angles. Achieving an optimal balance between air gap and raster width for all other thermoplastics is crucial to minimize air gap while ensuring effective bonding between consecutive rasters [64].

(e) Infill density and pattern

FDM enables the fabrication of parts with varying infill densities to optimize the material usage [64]. The infill density, referring to the internal structural density, can be customized with different patterns that define the construction of individual layers [68]. Considerable financial and savings can be achieved by employing reduced infill densities while maintaining the overall geometry [64]. In addition to specifying infill density, various patterns (**Figure 2.14**), including grid, quarter cubic, and tri-hexagon patterns, can influence the strength of printed parts [79]. Several studies on the flexural, tensile and impact resistance indicated that an increased infill corresponded to an enhanced load-bearing capacity [80]-[81].

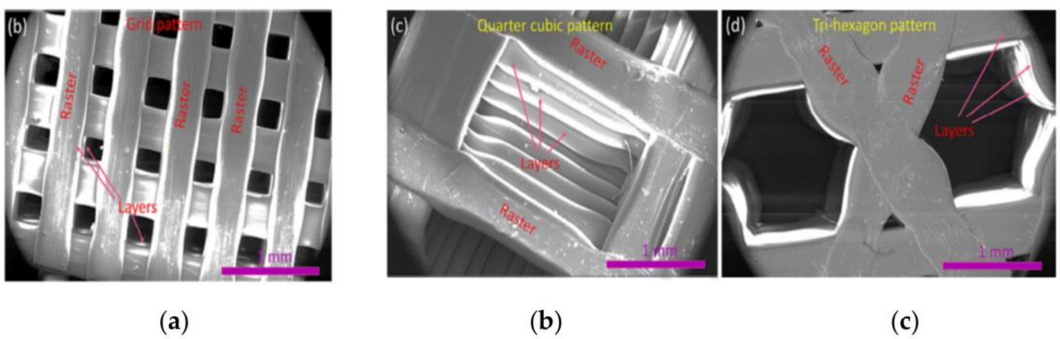

Figure 2.14: SEM images of various infill patterns: (a) Grid pattern; (b) Quarter cubic pattern; (c) Tri-hexagon pattern [79].

(f) Printing speed and extrusion temperature

A rise in printing speed is associated with a reduction in top surface hardness, and tensile strength, while concurrently increasing the porosity and average roughness in FDM parts [82]. Simultaneously, the extrusion temperature, influenced by the properties of the thermoplastic filament and print speed, plays a crucial role [83]. Extrusion temperature has also been identified as an important process parameter that affects the mechanical properties of FDM parts as optimal fusion between newly extruded layers and existing layers occurs before the extruded filament solidifies. However, printing speed has been identified in several studies as one of the most significant parameters due to its direct correlation to part quality [68]. Nevertheless, excessive temperature boosts molten plastic fluidity, leading to reduced viscosity and increased void formation, consequently weakening the mechanical properties.

2.3 Voids in FDM parts

Several defects are observed in FDM parts due to various factors including part design, processing, and environmental control of the FDM fabrication process. However, these defects can be minimized by careful optimization of print settings, proper material selection, and effective control of the printing environment [84]. Common defects/voids in FDM parts include delamination between layers, geometrical distortions, brittleness, and voids [43], [84].

Voids are one of the most unavoidable defects in any FDM part, posing challenges to the overall structural integrity and mechanical properties of the printed object [10]. Hence, special emphasis is placed to understand its significance and formation mechanisms as well as quantification methods in the next subsections.

2.3.1 Effect of voids on the mechanical properties

The desirability of voids in FDM parts is contingent upon the intended application, where favorable voids serve as 3D structural elements designed to enhance functionality or reduce weight [8]. Conversely, voids are undesirable in applications requiring optimal mechanical performance [85].

Several studies have focused on understanding the location and impact of porosity on the mechanical properties of AM materials, such as stiffness, strength, and toughness. **Figure 2.15** shows that AM parts can exhibit voids in various locations, including the surface, sub-surface, among deposited layers, and internal bulk material [86]. In addition, each type of void leads to a different type of failure. For example, the presence of inter-layer pores can affect the toughness of FDM parts, particularly when subjected to loads transverse to the layer orientation, as they can lead to delamination [16]. Whereas surface pores can affect the corrosion resistance characteristics [87]. Pores in other locations can act as damage initiation sites resulting in early failure under tensile and cyclic loading [88]-[89].

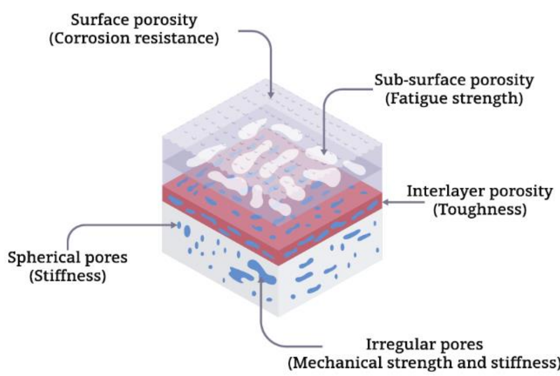

Figure 2.15: Porosity locations in AM parts [5].

The impact of porous structures or voids on the mechanical performance of FDM parts is notable, with stress concentrations formed around voids generally leading to a reduction in part performance [90]-[91]. Particularly, voids formed between deposited rasters adversely affect the stiffness, strength, and density of printed parts [91]-[94]. Porosity acts as a crack initiation site under load which results in premature failure [95]. Under loading, the stress is concentrated around voids, resulting in stress risers and stress concentration points. In addition, un-even presence of porosity results in anisotropic material properties [8]. Moreover, in FDM parts, porosity acts as a process-based defect which can only be mitigated. Currently, a pore free FDM part is not achievable using the current manufacturing processes. Therefore, the significance of quantifying porosity levels arises from the dependence of the static and cyclic mechanical properties of AM components on the microstructure, surface roughness, and density of FDM parts [96].

As porosity is undesirable for most FDM applications, researchers have proposed several methods to minimize the undesired impact of porosity: (i) controlling the pore distribution to increase the load-carrying capability of printed parts, (ii) modifications of existing AM machines, (iii) optimizing the process parameters and linking them with pore detection and quantification methods, and (iv) post-processing treatments [8].

2.3.2 Classifications of voids and formation mechanisms

Apparent and engineered porosities are the two main types of porosities observed in FDM parts. Apparent porosity refers to unintended porous defects that may occur in the structure or surface of the AM parts while, engineered porosity is intentionally created for specific functions and performance [8]. In FDM, porosity can be generated during printing or inherently present within the filament. Air trapped in the matrix, gaps between the beads and layers, uneven matrix distribution, and uneven filament diameters are some of the factors that can result in voids during printing [43]. Voids in FDM are classified into five main categories based on their formation mechanisms and are discussed below.

(a) Raster gap voids

The boundary of a complete layer is defined by its contour [97] (also denoted as shell [58], or wall [98]). This boundary is filled with rasters following a specified infill pattern as determined by the toolpaths generated in the slicing software. Raster gaps (also referred to as air gaps [77]) represent the spaces between adjacent rasters. This parameter assumes a negative value for overlapping rasters [99]. Generally, adopting an infill pattern with sparser raster spacings results in larger raster gaps, consequently leading to the formation of substantial internal voids (**Figure 2.16**). Undesirable voids caused by raster gaps have a detrimental impact on the mechanical performance of the printed parts. However, strategically employing larger raster gaps during printing could reduce the overall construction time and consumption of feedstock [100]. Thus, the choice of raster gap size plays a crucial role in balancing mechanical strength and printing efficiency.

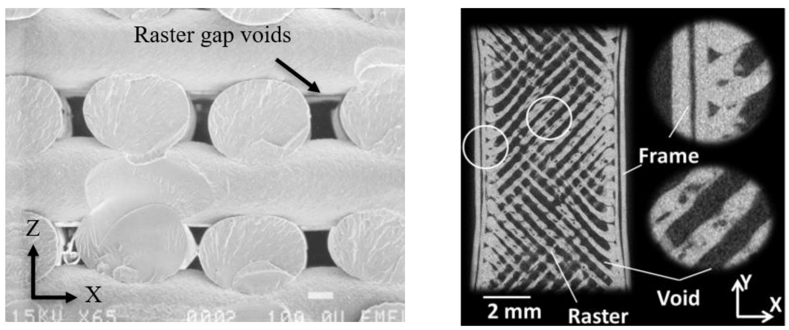

(a) (b)

Figure 2.16: (a) Raster gap voids in ABS parts [101] and (b) raster gap voids in nylon parts [102].

(b) Partial neck growth voids

Incomplete neck growth between adjacent layers can lead to the formation of internal voids in FDM parts. As illustrated in **Figure 2.17,** these voids arise from the insufficient coalescence between adjacent intra-layer and inter-layer rasters [103]. The occurrence of voids is intricately linked to the process of viscous sintering, where the creation of voids depends on the extent of neck growth between neighboring rasters. In an ideal scenario with full coalescence between two neighboring rasters, the formation of these voids would be physically impossible. However, rasters solidify before completing the coalescence process resulting in an incomplete neck growth [104]-[105]. Hence, due to inherent and unavoidable characteristics of the FDM process, such as incomplete filling and inconsistent material flow [106], it is impossible to entirely eliminate partial neck growth voids formed between rasters. Consequently, these partial neck growth voids emerge as significant contributors to the presence of porosity in FDM prints.

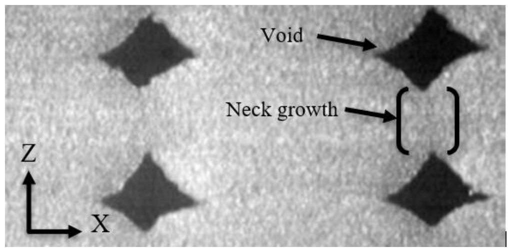

Figure 2.17: Partial neck growth voids in ABS parts [107].

(c) Sub-perimeter voids

The creation of sub-perimeter voids occurs between turning rasters along the contour of a FDM layer due to inherent physical limitations [9]. Traditional print paths address the filling of a print layer area by reversing the raster direction at the perimeter. However, achieving more comprehensive raster fillings necessitates sharper turns, inevitably leading to higher acceleration. To mitigate the adverse impact of centrifugal forces on stepper motors without significant compromises in build time, FDM printers must offset this by substituting all sharp corners with approximated curves [9]. Consequently, the adoption of these smoother curves results in insufficient material flow during deposition, leaving gaps and voids within FDM layers. Despite maintaining a 100% infill density, voids were observed between the wall lines and the infill zones [98], as shown in **Figure 2.18**.

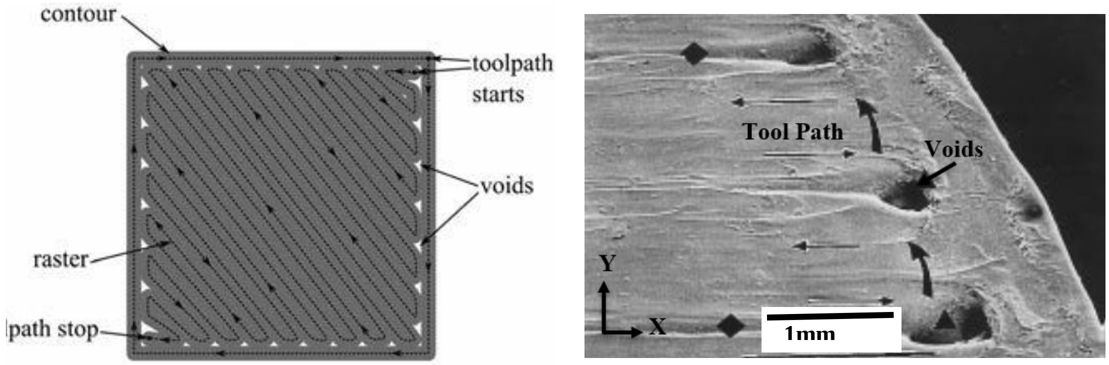

(a) (b)

Figure 2.18: (a) Sub-perimeter void formation [100] and (b) Sub-perimeter voids in FDM parts [108].

(d) Intra-bead voids

Internal gaps within beads are unique to FDM components made from composite materials [9], [91]. The type of voids observed in a full dense pure thermoplastic sample are characterized by partial neck growth voids (**Figure 2.19a**). Conversely, in composite feedstock filaments, apart from the triangular partial neck growth voids, there are additional porous structures at smaller scales that can be identified due to poor fiber–matrix interfacial adhesion (**Figure 2.19b)**.

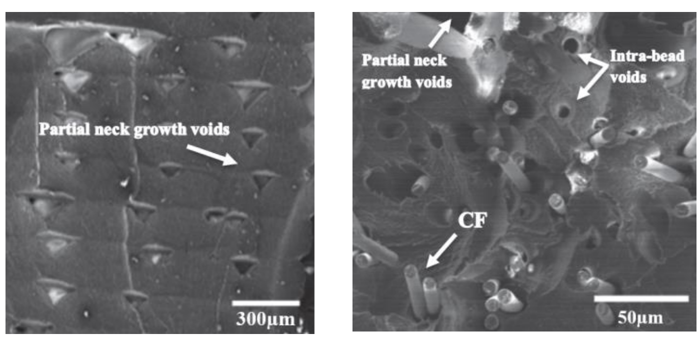

(a) (b)

Figure 2.19: (a) SEM of FDM parts with partial neck growth voids and (b) Intra-bead voids in ABS parts [109].

(e) Infill voids

Infill voids represent intentionally induced and manageable void formations. Slicing software designed for FDM typically integrates customizable infill densities and a range of selectable infill patterns, including grid, lines, triangles, concentric, zigzag, cross, and gyroid (**Figure 2.20**) [110]. Selecting lower infill densities proves advantageous in minimizing material consumption and shortening the overall build time. Conversely, higher infill densities yield more robust prints at the expense of increased material usage and a longer construction period [9].

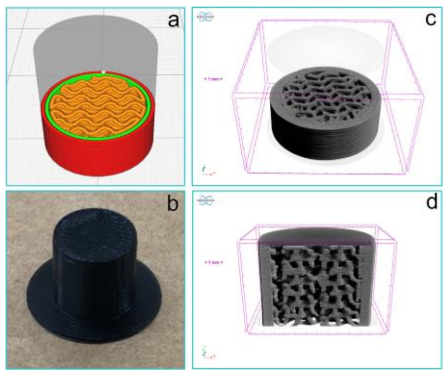

Figure 2.20: FDM part with gyroid infill type. (a) slicing software, (b) printed part, (c) μCT image, and (d) infill voids [110].

2.3.3 Effect of processing parameters on voids formation

The interplay of factors such as layer height, nozzle temperature, printing speed, and infill density significantly influence the structural integrity and voids observed in printed FDM parts. Investigating the impact of FDM process parameters on void formation not only enhances our comprehension of the printing process but also paves the way for improved print outcomes and quality. The effect of the most significant process parameters on void formation are explained below.

(a) Nozzle and bed temperature

Spoerk et al. [111] observed that elevated nozzle temperatures led to enhanced adhesion and resulted in the formation of smaller voids. The PLA component, illustrated in **Figure 2.21**, exhibited smaller voids when printed at 245 °C compared to the one printed at 205°C.

Beyond the impact on viscosity reduction and increased flowability, extreme nozzle temperatures also influence the dimensional accuracy and thermal degradation of FDM polymers. In Gao et al.'s [112] investigation, the void size in the cross-section of the PA 1012 component progressively decreased with rising nozzle temperature. However, the presence of air bubbles was observed as the printing temperature reached 260°C. Although the increased nozzle temperature significantly reduced void presence, the thermal degradation could have adverse effects on the mechanical properties of printed parts.

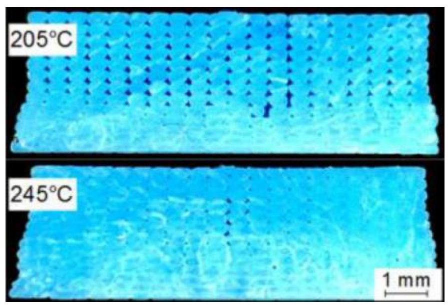

Figure 2.21: Effect of nozzle temperature on void size. Void sizes decrease with an increase in nozzle temperature [83].

In addition, the temperature of the print-bed has been identified as a significant parameter that affects the void formation along the print height [113]. Results show a reduction in voids near the heated print-bed (**Figure 2.21**). As the underside of the part is in proximity with the print-bed, it experiences a higher temperature resulting in continuous adhesion of the printed layers. However, the effectiveness of print-bed temperature weakens further away from the print-bed resulting in larger voids.

(b) Printing speed

Maintaining a consistent filament feed and nozzle temperature in FDM is influenced by the printing speed. Faster printing speed creates shorter intervals for heat transfer, leading to the extrusion of partially melted material [82]. This, in turn, may compromise interface adhesion due to reduced contact time. Abbott et al. [114] observed an increase in voids at a print speed of 50 mm/s compared a print speed of 10 mm/s (**Figure 2.22**).

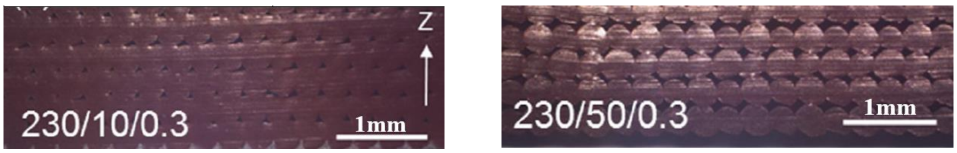

(a) (b)

Figure 2.22: Parts printed with parameters shown as nozzle temperature/printing speed/layer height. Variation in void size with (a) 10 mm/s and (b) 50 mm/s printing speeds [114].

Higher printing speeds were correlated with higher void quantities and compromised interlayer bonding. Additionally, high speeds impact polymer crystallization, where partially melted polymer particles serve as nucleation sites, limiting interface diffusion [115]. In essence, while decreasing void fraction and enhancing interlayer bonding, lowering printing speed may result in extended build time and reduced printing efficiency. Therefore, a balance between print productivity and quality is essential when adjusting printing speed.

(c) Layer size

Maintaining all other process parameters, Aliheidari et al. [113] discovered that altering the layer height of ABS parts led to larger voids due to the effect of layer height on the heating history of rasters and the bonding between layers. Specifically, their research revealed that utilizing a layer height of 0.2 mm resulted in superior mechanical performance compared to layer heights of 0.1 mm and 0.3 mm. Similar correlations between void morphology and layer height were observed in PLA [116], PP [117], and ABS [114] parts (**Figure 2.23a-b)**. The observed phenomenon in printed FDM parts with thicker layers can be rationalized by the reduction in contact pressure applied to the bottom layer which leads to shorter neck length and void enlargement [118].

(a) (b)

Figure 2.23: Parts printed with parameters shown as nozzle temperature/printing speed/layer height. Variation in void size with (a) 0.3 mm, and (b) 0.1 mm layer height [114].

(d) Infill pattern and density

Current FDM slicers offer a selection of infill patterns that aim to reduce the material usage and print weight. As mentioned previously, the internal geometry of FDM parts can be modified by adjusting the infill patterns and infill densities. In addition, the infill pattern determines the void distribution and morphology in parts with the same infill density (**Figure 2.24)**. Samples printed with 100% infill density contained the minimal void size. Therefore, increasing the infill density has been identified as a promising method for reducing void fraction in FDM parts [119].

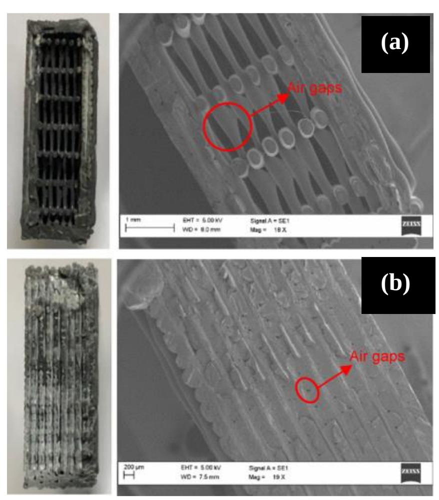

Figure 2.24: SEM images of voids (air gaps in red) in PLA samples with (a) 25% infill density and (b) 100% infill density [119].

2.3.4 Quantification methodologies

Quantifying voids in FDM is crucial for ensuring the structural integrity and quality of the printed parts. This process involves assessing the presence and distribution of voids within the printed material. Direct measurement methods and imaging techniques are some of the most commonly used techniques for quantifying the porosity in FDM parts. Utilizing these methods contributes to a comprehensive quantitative analysis of voids in FDM structures, enabling manufacturers and researchers to optimize printing parameters and enhance the overall quality of printed parts.

(a) Direct measurement methods

Part density provides a direct quantification of the void's presence in structures. Archimedes density measurement, and gas pycnometry are the most commonly used non-destructive methods for direct density evaluation [120]. The Archimedes method involves immersing the part in a fluid and measuring the buoyancy force exerted on the part. The displaced fluid volume is then used to calculate the density of the part. This method is straightforward and is used for its accuracy [121]. The density of the object can be calculated relative to the density of water without the need for volume measurements using the following reformulation of the Archimedes' principle [122]:

$$\rho = \frac{\rho_w}{1 - \left({}^{W_w}\!/_{W_a} \right)} \tag{2.1}$$

where ρ is the density of the object, ρ_w is the density of water = 1.00 g/cm^3, W_w is the weight of object in water, and W_a is the weight of object in air. On the other hand, gas pycnometry relies on the principle of gas displacement to measure the volume of the FDM sample. An inert gas, typically helium, is introduced into a chamber containing the sample.

The change in pressure after gas expansion is used to determine the volume of the sample which is then used to calculate its density. Gas pycnometry is commonly used for its precision in measuring small volumes [123]. The density of a sample can be calculated as [124]:

$$\rho = \frac{m}{(V_s - V_r) \cdot (P_2/P_1 - 1)} \quad \textbf{(2.2)}$$

where m is the mass of the sample, V_s is the volume of the sample's chamber, V_r is the volume of the reference chamber, P_1 is the pressure measured with the sample chamber only, and P_2 is the pressure measured with both chambers connected.

Finally, the bulk porosity is determined by comparing the measured densities (ρ_{porous}) to that of the solid material (ρ_{solid}) as per the following relation [94], [125]:

$$Porosity\ \% = \frac{\rho_{solid} - \rho_{porous}}{\rho_{solid}} \times 100 \quad \textbf{(2.3)}$$

It is important to note that while Archimedes is relatively simple to perform and standardized, cracks that allow for water-infiltration may lead to incorrect values [126]. High surface roughness typically found in AM parts may capture water bubbles and can result in erroneous measurements [127]. Similarly, gas pycnometry is limited by small sample size and inter-connected pores [126]. Despite these minor drawbacks, both Archimedes and gas pycnometry instrumentations are used to capture the overall porosity in printed AM samples. However, both techniques are unable to quantify the porosity distribution and morphology [128].

(b) Imaging-based techniques

In addition to density measurement, various imaging techniques are commonly employed to enhance the study of FDM voids. OM utilizes visible light and a system of lenses to generate magnified images [111]. SEM offers an image-based approach that uses a focused beam of electrons to produce high-resolution images [79]. Additionally, X-Ray CT is also utilized to analyze porous structures [129]-[130]. The X-Ray beam is passed through the object onto a detector that creates 2D images which are reconstructed into a 3D volume [131].

OM is commonly applied for investigating the meso-structures of printed parts [132], while SEM is often utilized for microstructural analysis [119]. Both OM and SEM have the capability to capture 2D data. Furthermore, they can be used for analyzing raster gap voids [101], partial neck growth voids [107], and intra-bead voids [109]. Similarly, OM and SEM can also be used to study sub-perimeter voids [108]. Likewise, X-ray CT serves as a valuable tool for observing and investigating the effects of FDM voids in three dimensions. In addition, CT enables the quantification of porosity distribution and morphologies in a more comprehensive manner [133]. This technique can be used to study the void size, density, connectivity, shape, and distribution. The analysis of the CT data is based on the pixilated images collected from the device. The porosity content or voids fraction can be calculated as [134]:

$$Voids\ fraction = \frac{pixels\ (or\ voxels)\ of\ voids\ space}{total\ pixels\ (or\ voxels)\ of\ image} \quad \textbf{(2.4)}$$

Lastly, some recent works have also proposed in-situ systems with machine learning based models to predict porosity [50]-[51]. However, porosity measurements using such real time methods is complex and requires further development [137].

2.4 Simulation methods of voids

Imaging-based methodologies serve as the major experimental approach to examine and analyze voids in FDM parts [9]. However, it is essential to gain a comprehensive understanding of void formation due to FDM process parameters. This poses a significant challenge in realizing specific hierarchical structures and attaining optimal mechanical performance of FDM parts. As experimental approaches (Section 3.1) require extensive time and resources, numerical and analytical techniques are commonly used to quantify the effect of porosity in FDM parts.

2.4.1 Analytical approaches

Analytical approaches can be used to predict the effective properties (such as its E, Poisson's ratio, and UTS of AM parts [138]. These properties can then be used to simulate the behavior of AM parts under different loading conditions. This allows designers and engineers to optimize the design of AM parts with in-built porosity by predicting their mechanical behavior and identifying potential failure modes.

Over the last four decades, researchers have proposed several analytical approaches for quantifying the effect of porosity in AM parts. Isida and Igawa [139] conducted a theoretical analysis on a uniform zigzag array of circular voids under uniaxial tension by using complex stress potentials. They suggested an effective modulus approach with a dimensionless parameter. Gibson and Ashby [140] also proposed a model to determine the properties of porous samples. Their model predicted the E and YS of the porous material as a function of the relative density of the solid material. The Gurson model has also been used to simulate the mechanical properties of ductile metals with voids [141]-[142]. The Gurson model assumes that the material is composed of a solid matrix and spherical voids. The model predicts the effective stress as a function of the volume fraction, size, and shape of the voids. Eshelby inclusion model has also been used to study the elastic behavior of composite materials containing inclusions of arbitrary shapes and orientations [143]-[144]. It assumes linear elastic inclusions and can also be used to study the effect of porosity.

Researchers have presented several fundamental correlations, which can be employed for AM parts, between the stiffness of a porous (E_p) and solid (E_o) phase [145]-[153]. These correlations usually involve comparing the porous structure to a composite material with two phases. The initial model shown in **Table 2.1** is an over simplification and assumes a linear relationship between the net porosity (p) and total volume. However, several other models have been proposed that capture the non-linear behavior between the porosity and material stiffness, as detailed in **Table 2.1**.

Table 2.1: Relationships for estimating the effective E of a porous material [138].

Source	Type	Equation	Constants
Dewey [147]	Linear	$\frac{E_p}{E_o} = 1 - aP$	***a***: Poisson's ratio dependent constant.
Spriggs [146]	Exponential	$\frac{E_p}{E_o} = \exp{(-mP)}$	***m***: material dependent constant.
Wang [148]		$\frac{E_p}{E_o} = \exp{[-(\mathrm{nP} + \mathrm{q}P^2)]}$	***n* and *q***: nonnegative numbers dictated by shape of theoretical curves.
McAdam [154]		$\frac{E_p}{E_o} = (1 - jP)^i$	***i***: Pore's morphology dependent constant, ***j***: The reciprocal of the critical porosity.
Martin & Haynes [155]	Power	$\frac{E_p}{E_o} = 1 - uP^{2/3}$	***u***: Average void properties dependent constant.
Bert [151]		$\frac{E_p}{E_o} = (1 - \frac{P}{Q})^{KQ}$	k: Stress concentration factor, Q: maximum possible porosity.
Ramakrishnan & Arunachalam [152]	Rational	$\frac{E_p}{E_o} = \frac{(1-P)^2}{(1+yP)}$	**y:** Poisson's ratio dependent constant.
Hashin [156]		$\frac{E_p}{E_o} = \frac{(1-P)}{(1+wP)}$	**w:** Poisson's ratio dependent constant.

2.4.2 Numerical modeling approaches

FEM is considered an effective tool to investigate the effect of process parameters on the mechanical properties of FDM parts [138], [157]. Results from FEA models are used for numerical optimization of process parameters with experimental validations [132]. Sheikh et al. [158] presented a hierarchical multiscale model to analyze the effect of FDM process parameters on the elastic and shear moduli of printed parts. Their model involved generating RVEs (**Figure 2.25**) and solving them using FEA with periodic boundary conditions. Their study investigated raster orientation (0º, 0º/90º, and 45º/-45º), layer height (0.1, 0.2, and 0.3mm), and porosity in terms of infill density (100%, 75%, 50%, and 25%). Their findings were validated with experimental results for PLA samples which revealed that porosity had the greatest influence on the mechanical properties, followed by layer height, and raster orientation.

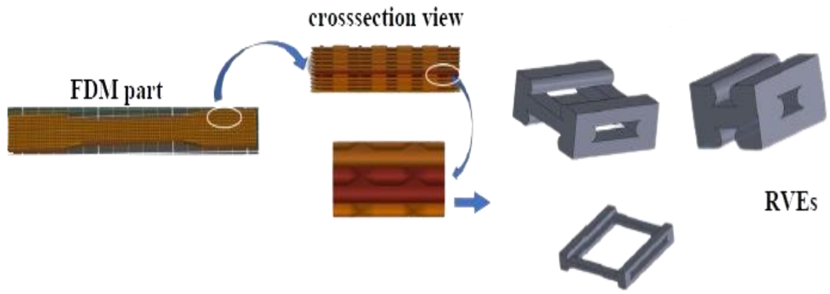

Figure 2.25: RVEs used for analyzing the effect of various process parameters [158].

Anoop and Senthil [159] performed a similar study and highlighted the microscale models that capture the directional disparity using the RVE approach (**Figure 2.26**) by investigating raster orientation (0^o, $0^o/22.5^o$, and $45^o/-45^o$), layer height (0.1, 0.2, and 0.3mm), and porosity in term of infill density (100%, 75%, and 50%). Their FEA model enforced boundary conditions for six independent directional strains. Using statistical tools, they reported infill density as the most significant factor in determining the elastic properties of FDM parts.

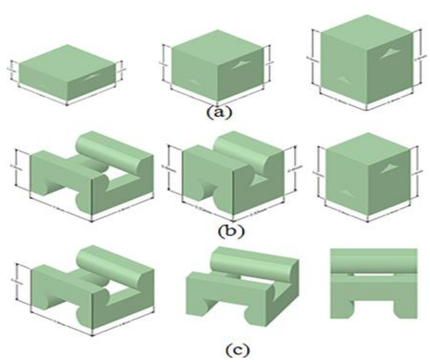

Figure 2.26: RVEs (a) with 100% infill density for 3 levels of layer height, (b) with 3mm layer height for 3 levels of infill density, and (c) with 50% infill density for 3 levels of raster orientations [159].

Balanzar et al. [160] presented a computational homogenization and multiscale FEM model to determine the stiffness tensors of the proposed RVEs to predict the mechanical properties of printed FDM parts. Their RVE idealized random real pores from CT images

(**Figure 2.27**) and the mesostructured geometry with various raster angles (0^o, 45^o/-45^o, and 0^o/90^o) and build orientations (flat, edge, and upright). They also performed FEM with periodic boundary conditions and validated their results.

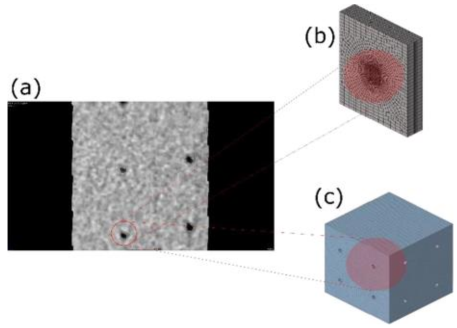

Figure 2.27: (a) CT image from FDM sample, (b) unidirectional RVE, and (c) 0^o/90^o RVE with idealized random real pores [160].

Ferretti et al. [161] presented a linear RVE model to predict the macroscopic tensile behavior of PLA FDM parts. The microstructure for their proposed RVE model was based on OM images from unidirectional raster orientation (0°). They treated the FDM part as a fiber composite composed of PLA and Air (**Figure 2.28**). Three different void dimensions were considered with different RVE's (**Figure 2.28a-c)**. Their model assumed good adhesion between layers and was only valid for small deformations.

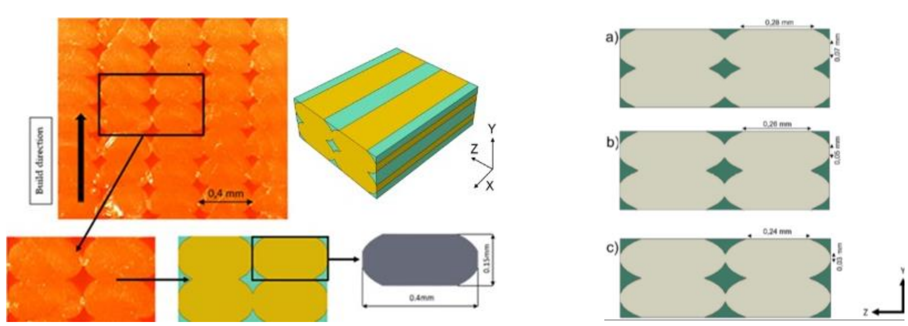

Figure 2.28: RVE model where PLA is indicated in yellow, and air is indicated in green, idealized using OM image, with void dimensions (a) lengths of 0.07 and 0.28 mm, (b) 0.05 and 0.26 mm, and (c) 0.03 and 0.24 mm [161].

Wang et al. [162] fabricated PLA tensile test specimens using FDM with varying raster orientations (0°, 90°, 45°/-45°, and 0°/90°) and extrusion widths (0.48, and 0.24 mm). The internal pores were characterized using X-Ray CT and a MATLAB® script was used to develop the RVE. The RVE was modeled as a 2D elastic plate with random circular pores (**Figure 2.29**). Their FEM model predicted the elastic properties and showed good agreement with experimental data.

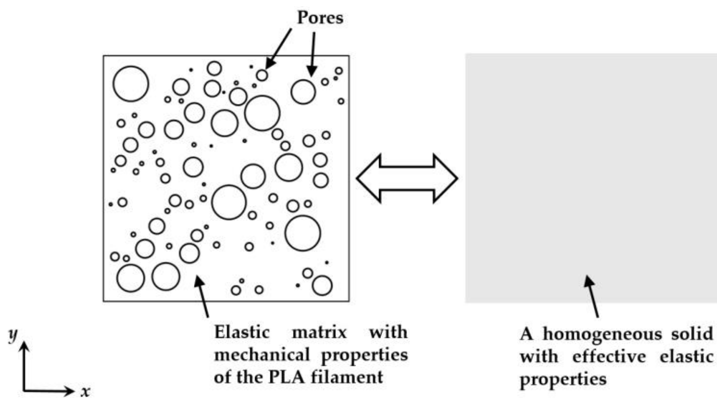

Figure 2.29: 2D RVE model with randomly distributed pores [162].

Ferrano et al. [163] also presented a macroscale FEM study to investigate the mechanical properties of FDM PLA full-dense components with different raster orientations (0°, 90°, 45°, 45°/-45°, and 0°/90°). X-Ray CT was used to enable a realistic prediction of deformation behavior and strength. Their analysis idealized a full geometrical tensile sample with a solid model (**Figure 2.30**). The material behavior assumed isotropic elastoplastic model and employed a hardening equation with failure criterion.

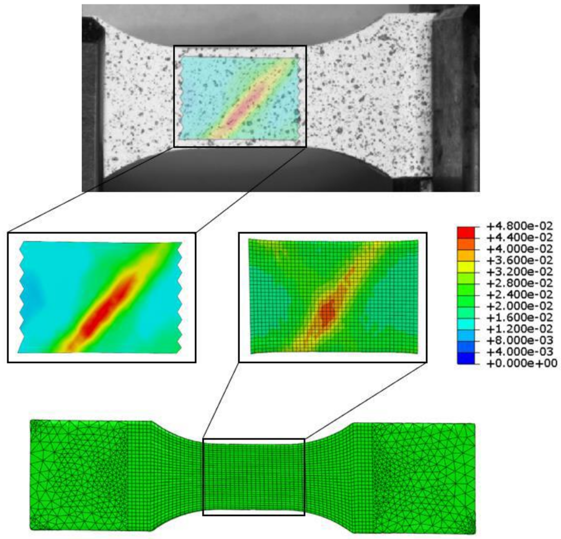

Figure 2.30: Comparison of a FDM FEA macroscale model and test results[163].

Kerekes et al. [164] studied the impact of FDM process parameters on mechanical properties with varying infill density (low, medium, and solid) and layer thickness (0.254, and 0.330 mm) for ABS samples. They used their experimental results to validate a macroscale FEA model with Gurson-Tvergaard (GT) porous plasticity model to predict the elastoplastic damage behavior (**Figure 2.31**). They assumed a solid homogeneous isotropic model with varying material definitions for the infill and borders. Their study validated the GT porous plasticity model in combination with a 3D FEM model to predict the macroscopic elastoplastic damage behavior of FDM specimens. An inverse identification analysis was also conducted to establish the process–property relationship using the GT porous plasticity model. However, the macroscale continuum modeling approach failed to accurately predict non-uniform strains observed in the experimental results.

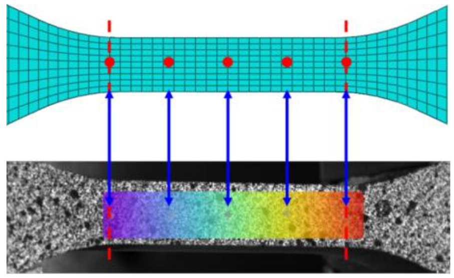

Figure 2.31: Macroscale FEM model with experimental results for FDM ABS parts [164].

Garg and Bhattacharya [15] followed a similar approach and presented a realistic FEM model of an FDM ABS tensile test specimen that was derived from OM images (**Figure 32**). Multiple printing process variables were integrated into the model, including raster orientations (0^o, 90^o, 45^o, and $0^o/90^o$), layer thickness (0.178, 0.254, and 0.330), overlap interval, and air gap. The model assumed isotropic and homogeneous material properties. Their simulated results were validated with experimental analysis and gave comparable observations. A summary of the mentioned models across different approaches is given in **Table 2.2**.

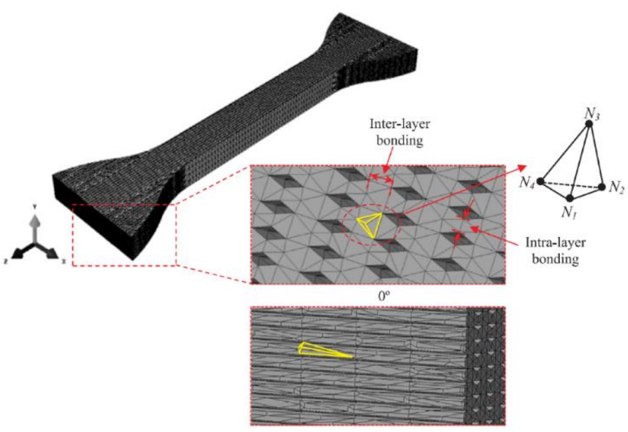

Figure 2.32: Macroscale FEM model for FDM tensile samples with 0^o and 90^o raster orientations [15].

Table 2.2: Summary of the FEM studies that consider porosity simulation in FDM process.

Reference	Material	FE Model	Software	Involved parameters	Objectives
Sheikh et al. [158]	PLA	3D RVE	Ansys® APDL	Raster orientation, layer height, and infill density	Effects on the elastic and shear moduli
Anoop & Senthil [159]	-	3D RVE	ANSYS® Workbench	Raster orientation, layer height, and infill density	Effects on elastic properties
Balanzar et al. [160]	ABS	3D RVE	-	Raster orientation, and printing orientations	Stiffness tensors prediction
Ferretti et al. [161]	PLA	3D RVE	ANSYS®	Raster orientation with void dimensions	Effects on elastic properties
Wang et al. [162]	PLA	2D RVE	ABAQUS®	Raster orientations, and extrusion widths	Elastic properties predictions
Ferrano et al. [163]	PLA	3D Full geometry	ABAQUS®	Raster orientations	Effects on tensile properties
Kerekes et al. [164]	ABS	3D Full geometry	ABAQUS®	Infill density and layer thickness	Effects on tensile properties
Garg & Bhattacharya [15]	ABS	3D Full geometry	ABAQUS®	Raster orientations, and layer thickness	Effects on tensile properties

2.4.3 Research gaps

Literature lacks exhaustive analytical studies or predictive equations that describe the correlation between various types of porosities and mechanical properties for FDM parts [138], [165]. Hence, a definitive analytical model that establishes a clear relationship between material porosity and mechanical properties for FDM is needed.

As presence of voids impacts the part performance, FEM models should consider voids in the macroscale geometry [166]. However, due to computational resource challenges, the shape, size, number, and orientation of the pores are normally defined in microscale model as a RVE [138]. Notably, most of the relevant studies used for macroscale and microscale FEM models simulate the effect of voids on the mechanical properties of FDM parts based on several simplification assumptions. Hence, an in-depth analysis is required into the possible combination or modification of existing models to predict the effect of process parameters and voids on the mechanical properties of FDM parts.

FEM models can also be used to predict the mechanical properties of FDM parts and offer higher accuracy than analytical models but demand extensive resources. However, the accuracy of FEM can be improved by utilizing advanced models and experimental data [167]. Therefore, it is crucial to predict the impact of voids in FDM parts by using accurate and refined FEA models to establish the link between infill density and mechanical properties of printed parts.

CHAPTER 3

METHODOLOGY

3.1 Experimental work

3.1.1 Sample preparation and printing

In this work, PLA filament from Raise3D was used for manufacturing the FDM samples (**Table 3.1)**. A Raise3D E2 FDM printer (**Figure 3.1a)** was used to print the FDM samples while the CAD models were sliced using IdeaMaker®.

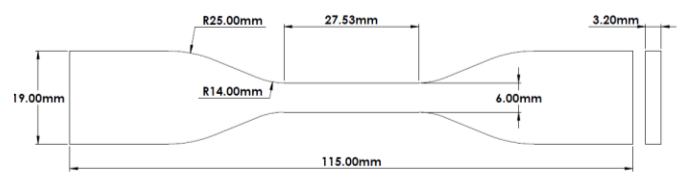

Figure 3.1: (a) Raise3D E2 FDM Printer, and (b) dimensions of tensile samples.

Table 3.1: PLA specifications [168]

Property	**Testing Method**	**Typical Value**
Product name	Raise3D Premium PLA	
Manufacturer	Shanghai Fusion Tech Co., Ltd. (for raise3D)	
Density (21.5 °C)	ASTM D792 (ISO 1183, GB/T 1033)	1.2 g/cm³
Glass transition temperature	DSC, 10 °C/min	61 °C
Crystallization temperature	DSC, 10 °C/min	114 °C
Melting temperature	DSC, 10 °C/min	150 °C
Young's modulus (X -Y)	ASTM D638 (ISO 527, GB/T 1040)	2636 ± 330 MPa
Tensile strength (X-Y)	ASTM D638 (ISO 527, GB/T 1040)	46.6 ± 0.9 MPa
Elongation at break (X -Y)	ASTM D638 (ISO 527, GB/T 1040)	1.90 ± 0.2 %

The tensile samples printed in this work were designed according to ASTM D638-10 type IV geometry for both the dense and porous samples (**Figure 3.1b)**. The same processing parameters were used to print the dense and porous tensile samples with three repetitions (**Table 3.2)**. The use of alternating raster angles combined with an infill pattern of lines was used to mitigate the anisotropy in the mechanical properties of FDM PLA printed parts. Several studies have shown that alternating the orientation of the infill lines result in even stress distribution throughout the material [169]. Consequently, it enhances the mechanical uniformity across different directions, leading to improved strength and durability of the printed parts [79], [169], [170]. Additionally, using line infill patterns can enhance printing speed as they allow for continuous, uninterrupted extrusion paths. This reduces the need for frequent interruptions during the print process and results in an efficient printing operation with better surface finish [166].

Table 3.2: Processing parameters used to print the FDM PLA samples.

Parameter	**Value**
Build orientation	Horizontal (X-Y)
Nozzle temperature	205 °C
Bed temperature	60 °C
Infill speed	70 mm/s
Nozzle diameter	0.2 mm
Layer height	0.2 mm
Raster width	0.4 mm
Raster angle	+45°/-45°
Infill density	50%, 60%, 70%, 80%, 90%, and 100%
Infill pattern	Lines

Five levels of infill density from 50% to 90% were used. Full dense samples were also printed for calibrating the FEM and analytical models. An example of a printed sample with 50% infill density is shown in **Figure 3.2a**. The predefined toolpaths used to manufacture the FDM samples are shown in **Figure 3.2b**.

(a) **(b)**

Figure 3.2: (a) Printed PLA FDM sample with 50% infill density and (b) toolpath for internal rasters.

3.1.2 SEM imaging

FEI™ Quanta FEG 250 SEM (**Figure 3.3**) was used at 20 kV to analyze the voids formation as well as the dimensional accuracy of the printed samples. All samples were gold coated for 20 s prior to analysis. The as-built and fractured surfaces from tensile samples were analyzed to reveal the microstructural features across various infill densities.

Figure 3.3: FEI™ Quanta FEG 250 SEM machine.

3.1.3 Tensile testing

The uniaxial tensile tests were conducted using an Instron® 3367 Universal Testing System with a load cell of 30 kN and a crosshead velocity of 2 mm/min (**Figure 3.4a**). An Instron® 12 mm extensometer with a range of ±5 mm (**Figure 3.4b**) was also used. The analysis of the experimental data provided essential mechanical properties, including UTS and E. The engineering stress-strain curves were generated according to the acquired force and extensometer data from the tensile experiments. The engineering curves were thrn converted into true stress-strain data before using them in the FEA simulations.

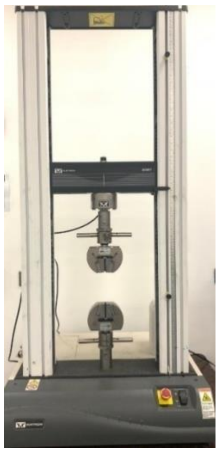

(a)

(b)

Figure 3.4: (a) Instron® 3367 Universal Testing System for tensile tests and (b) Instron® Catalogue 2620-601 12 mm extensometer.

3.2 Analytical models

Analytical models provide a faster and efficient approach for predicting the material behavior. Various analytical models (Chapter 2) were used to predict the effective tensile modulus ($\boldsymbol{E_e}$) of solid parts with inherent pores. Constants for each model were calculated based on the experimental results. $\boldsymbol{E_o}$ was calculated from the full-dense sample whereas the material or geometrical constants ($\boldsymbol{a}$, $\boldsymbol{m}$, $\boldsymbol{u}$..etc.) were calculated using the tensile test results of 50%, 70% and 90% infill densities. The results from the 60% and 80% FDM samples were used for validating the proposed models. A new model was also proposed and calibrated with the optimum constants. All the analytical models used in this work are provided in **Table 3.3.** The relationship between the proposed effective tensile modulus and the porous structure was used to represent the elastic material model in the numerical simulation approaches used in this work.

Table 3.3: Analytical relations for E predictions of porous samples.

Type	Equation	Source of origin
Linear	$E_p = E_o(1 - bp)$	[147]
Exponential	$E_p = E_o[\exp(-mp)]$	[146]
Power	$E_p = E_o(1 - up^{2/3})$	[155]
Rational	$E_p = E_o[\frac{(1-p)^2}{(1+yp)}]$	[152]
Proposed model	$E_p = E_o[\exp(-ap^b) + p^n]$	Proposed

3.3 Computational modeling

The tensile properties (E and UTS) of the FDM samples with in-built voids were predicted using FEA. ANSYS® Workbench 2023 R1 was used to create a nonlinear static structural FEA model. Dense and porous samples were simulated under uniaxial tensile loading to assess the strength and stiffness variation with different porosity levels. Multiple simulation approaches were proposed, including combinations of numerical and analytical models, to analyze the tensile behavior of FDM parts with different void fractions. Next, the simulated results were verified and validated with experimental results.

3.3.1 Governing equations

In this work, nonlinear FEA for structural mechanics was used, for both the 3D and 2D simulations. Typically, the equilibrium equations and constitutive equations are required to derive the governing equations. The equilibrium equations express the balance of forces acting on the body. In a nonlinear static analysis, they are usually given by [171]:

$$\nabla . \sigma + F = 0 \qquad \textbf{(3.1)}$$

where σ is the stress tensor, and F represents the external forces. The full form for 3D static analysis can be given as:

$$\begin{aligned} \frac{\partial \sigma_x}{\partial x} + \frac{\partial \tau_{xy}}{\partial y} + \frac{\partial \tau_{xz}}{\partial z} + F_x = 0 \\ \frac{\partial \tau_{xy}}{\partial x} + \frac{\partial \sigma_y}{\partial y} + \frac{\partial \tau_{yz}}{\partial z} + F_y = 0 \\ \frac{\partial \tau_{xz}}{\partial x} + \frac{\partial \tau_{yz}}{\partial y} + \frac{\partial \sigma_z}{\partial z} + F_z = 0 \end{aligned} \tag{3.2}$$

where σ_x, σ_y and σ_z are the normal stresses in the x, y, and z directions respectively, τ_{xy} ,τ_{xz}, and τ_{yz} are the shear stresses in the xy, xz, and yz planes respectively, and F_x, F_y, and F_z are the external forces in the x, y, and z directions respectively. Additionally, the constitutive relation for materials undergoing plastic deformation is typically represented by the stress-strain relationship. It can be expressed in the simplest form as [171]:

$$\sigma = D\!:\epsilon \tag{3.3}$$

where ϵ is the strain tensor, and D is the constitutive matrix. However, for large deformations that cause geometric nonlinearity, strains are not simply related to the displacements. A common way to handle this is by using the Green-Lagrange strain tensor [171]:

$$\epsilon = \frac{1}{2}(\nabla \boldsymbol{u} + \nabla \boldsymbol{u}^T) \tag{3.4}$$

where $\boldsymbol{u}$ is the displacement vector. Combining the equilibrium equations, constitutive equations, and geometric nonlinearity (**Equations 3.1 – 3.4**), gives the equation for the full nonlinear static analysis for 3D problems:

$$\nabla . \left\{D\!:\left[\frac{1}{2}(\nabla \boldsymbol{u} + \nabla \boldsymbol{u}^T)\right]\right\} + \boldsymbol{F} = 0 \tag{3.5}$$

The assumption of 2D plane stress implies that the stresses and strains in the thickness direction are negligible compared to those in the plane of interest. The equations remain essentially the same, with slight modifications. The equilibrium equation for the 2D problem is given as:

$$\frac{\partial \sigma_x}{\partial x} + \frac{\partial \tau_{xy}}{\partial y} + F_x = 0$$
$$\frac{\partial \tau_{xy}}{\partial x} + \frac{\partial \sigma_y}{\partial y} + F_y = 0 \quad \textbf{(3.6)}$$

These are transformed to the so-called weak form using the principle of virtual work or energy minimization principles. The elemental formulation for stiffness matrix and force vector are derived from the weak form. The stiffness matrix relates the nodal displacements to the internal forces within each element and is derived from the material properties and geometry of the element in linear analysis. In nonlinear analysis, it varies with the current state of deformation. It represents the relationship between the applied forces and the resulting deformations, and it can be defined as [172]:

$$K = \int B^T D B dV \quad \textbf{(3.7)}$$

where V is the volume, and B is the strain-displacement matrix. Matrix B would typically be a 6×3n matrix (where n is the number of nodes) and D is a 6×6 constitutive matrix for the 3D case. On the other hand, B (Strain-displacement matrix) would be a 3×2n matrix and D would be a 3×3 constitutive matrix for the 2D (plane stress) case. The global stiffness matrix is represented by assembling the elements stiffness matrices according to the node connectivity. In static analysis, this assembly also accounts for the applied boundary conditions and is represented as:

$$[\boldsymbol{K}]\{u\} = \{\boldsymbol{F}\} \quad \textbf{(3.8)}$$

where $\boldsymbol{K}$ is the global stiffness matrix, and **F** is the force vector. These nonlinear algebraic equations are then solved for equilibrium using iterative methods like Newton-Raphson [173].

3.3.2 Material models

PLA is often categorized as an elastoplastic material as it exhibits both elastic and plastic behavior under stress [174]-[175]. However, some studies modeled PLA as visco-elastic-visco-plastic material for analyzing the effect of strain-rate [176]. While PLA can exhibit some plastic behavior, it is generally considered more brittle compared to true elastoplastic materials [67]. Since this analysis considers uniaxial tensile loading with constant strain-rate, an elastoplastic material model was defined for PLA.

An Isotropic Linear Elastic model was configured for all approaches and E was defined according to the predictions from the optimum analytical relation at each porosity level. The Isotropy assumption was attributed to the infill pattern (45°/-45°) used in this work. Stiffness was updated for each porosity level with its corresponding effective stiffness used to relate the material density to material stiffness. Poisson's ratio was fixed as 0.36 across all approaches [177].

Additionally, the plastic behavior was defined using a Multilinear Isotropic Hardening model which simulated the nonlinear strain hardening response until necking. The model was defined based on the experimental true plastic stress-strain results. As behavior after necking cannot be predicted accurately, data after the UTS was neglected. The default material hardening behavior was based on the plastic behavior of the full-dense sample (100%) for specific modeling approaches. Alternatively, an extended model was also used that was based on multiple hardening curves (50%, 70%, and 90%). In this approach, a porosity dependent user-defined function was defined. Results from the 60%, and 80% samples were used for validation to assure the predictability of the hardening behavior across random infill densities.

Lastly, material density was the only required physical property of the user defined material model which was required for all numerical approaches used in this work. The material density was set as as 1.2 g/cm³ according to the PLA's supplier technical data sheet.

3.3.3 Geometrical models and boundary conditions

In all geometrical models used in this study, only the gauge length of the tensile samples was modeled for computational efficiency. The gauge length for various CAD models namely: (a) 2D dense, (b) 2D porous, (c) 3D dense and (d) 3D porous were created in Solidworks®. The 2D (**Figure 3.5a**) and 3D (**Figure 3.5b**) dense models were defined as rectangles that represented the gauge length of the samples.

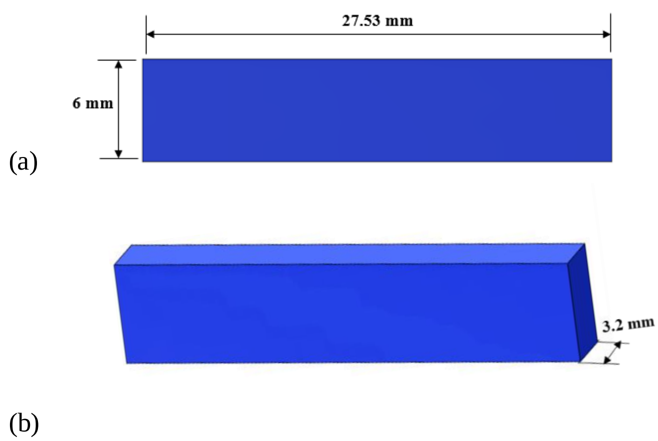

Figure 3.5: The CAD model for (a) 2D dense and (b) 3D dense FEA models.

In addition, 2D and 3D porous models were also constructed to model the material behavior under tensile loading. The 2D porous geometrical models were projected by representative models of stacking subsequent layers. These geometrical models were verified by the average dimensions across all infill densities using optical and SEM analysis. The effect of infill density on void fractions was captured by the raster gaps variation, as shown in **Figure 3.6**.

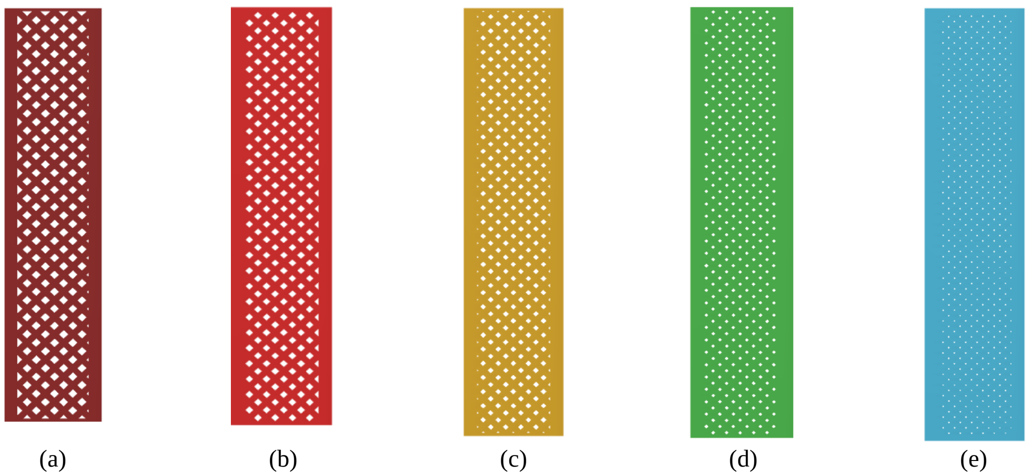

Figure 3.6: 2D CAD porous models for (a) 50%, (b) 60%, (c) 70%, (d) 80%, and (e) 90% infill densities.

For the 3D porous models, CADs were generated in alignment with the designated infill pattern and other predefined processing parameters and part dimensions. To generate the 3D porous models, the inner infill layers were constructed with a partial overlap between the stacked layers (**Figure 3.7 Steps 1-3**). Then, the shells (boundaries) were added around the inner infill layers (**Figure 3.7 Step 4**). Lastly, the first (bottom) and last (top) layers were attached to the overall model (**Figure 3.7 Step 5**). The first and last layers were built as full-dense parts in accordance with the slicing software.

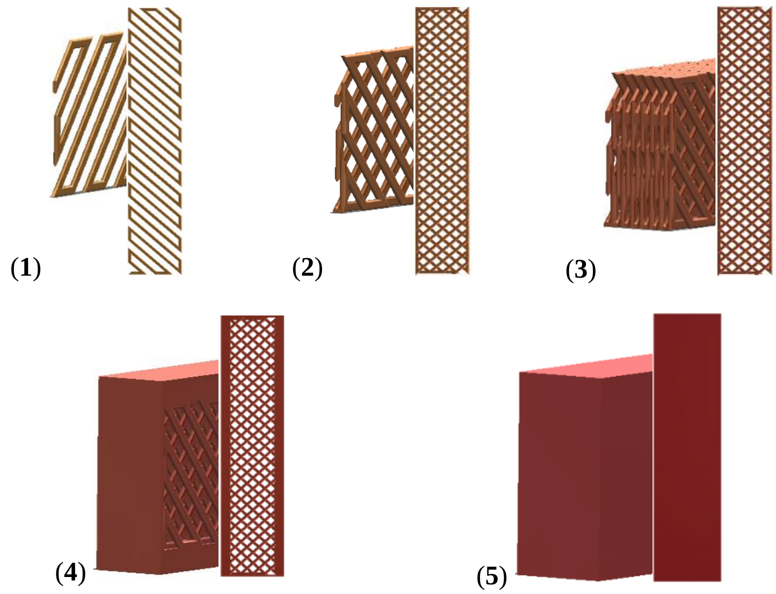

Figure 3.7: 3D porous model's construction steps for 50% infill density.

The same steps were then used to generate the CAD geometry for all infill densities. **Figure 3.8** shows the corresponding CAD models for 60%, 70%, 80% and 90% infill densities with partial view of the internal infill rasters.

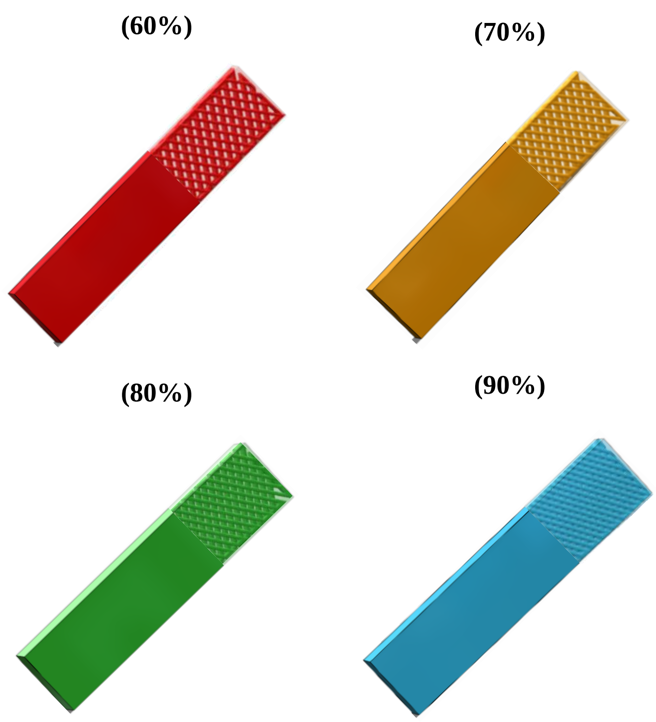

Figure 3.8: 3D porous CAD models for various infill density levels (60%, 70%, 80%, and 90%).

Lastly, a displacement and fixed boundary condition (**Figure 3.9**) were applied on all samples to predict the tensile response with various void fractions. Geometric nonlinearity was accounted by enabling large deflections in the analysis along with automatic time stepping to achieve convergence. The final displacement was applied in multiple load steps to mimic the experimental setup and avoid erroneous stress concentrations.

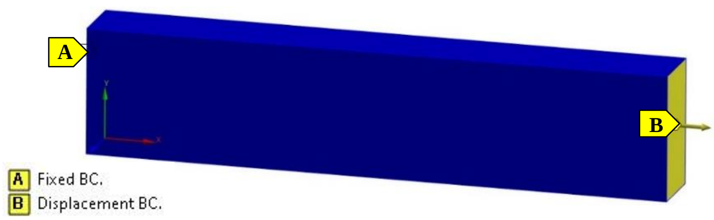

Figure 3.9: Applied boundary conditions.

3.3.4 Meshing

Part discretization for FEM analysis was carried out for all parts. **Figure 3.10** shows a typical Quadrilateral and Hexahedron mesh for the full-dense 2D and 3D parts, respectively. The final mesh size was based on a mesh sensitivity analysis for the 2D and 3D parts (**Table 3.4**). The maximum stress results showed a mesh convergence near 4000 and 70,000 elements for the dense 2D and 3D parts, respectively.

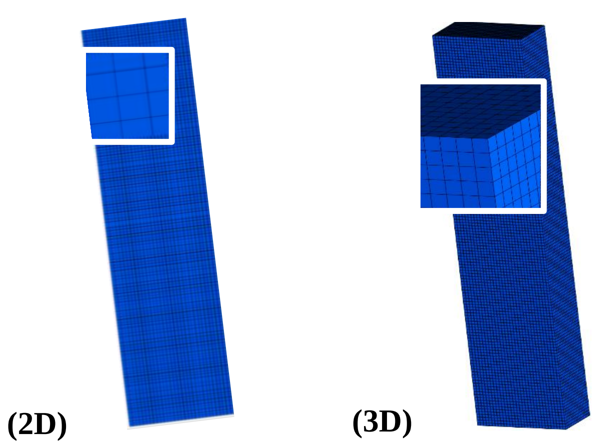

Figure 3.10: Mesh for 2D and 3D dense models.

As the porous models required finer mesh, the 2D and 3D porous geometrical models were meshed using Triangular and Tetrahedron elements with finer mesh. A mesh refinement tool was also used to enable efficient discretization around the voids. **Figure 3.11** shows a sample of the meshed shells, voids, and rasters in the 80% 3D porous model. A similar approach was adopted for the 2D porous models. A finer mesh was used around the infill to capture the void geometry while a course mesh was used in the shells (**Figure 3.12**). Based on the mesh sensitivity analysis (**Table 3.4**), a final mesh of 25473, 28459, 38868, 77976, and 98075 elements was used for 50%, 60%, 70%, 80% and 90% samples in 2D porous models. Also, 834234, 872472, 1129870, 1270985, and 1750687 elements were used for 50%, 60%, 70%, 80% and 90% 3D porous models.

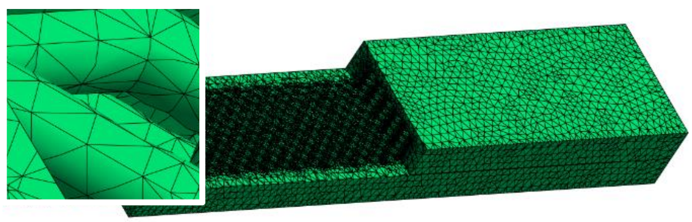

Figure 3.11: Mesh for the 3D porous models.

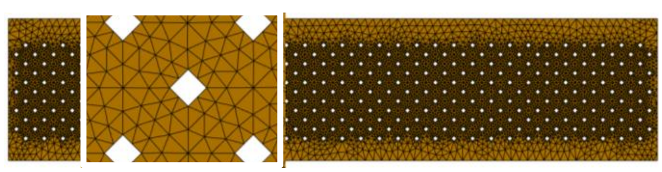

Figure 3.12: Mesh for the 70% 2D porous model.

Table 3.4: Mesh convergence analysis with respect to Error% of UTS predictions.

Approach	No. of elements	Error %
2D-D	1103	9.80
	1840	4.74
	4140	**0.94**
	14720	0.94
2D-P*	6007	7.11
	7590	3.39
	25473	**0.66**
	63887	0.66
3D-D	15490	5.75
	34632	2.71
	70890	**0.43**
	113998	0.43
3D-P*	102933	14.18
	515601	9.11
	834234	**1.68**
	1392516	1.68

*Results are based on 50% infill density.

3.3.5 Modeling approaches

A total of four approaches were used according to the variations in the material and geometrical definitions as described in the preceding subsections. The proposed approaches are detailed and summarized in **Table 3.5**. It should be noted that D and P represent dense and porous structures, respectively. Additionally, the hardening models are presented as 100 and 100+ and denote the full-dense multilinear hardening behavior and the extended porosity based hardening model, respectively. The stiffness was defined similarly for all approaches using the proposed analytical model. For example, 3D-P-100 approach simulated a 3D porous model with a hardening behavior defined by full-dense parts. On the other hand, a 2D-D-100+ approach simulated a 2D full-dense model with a hardening behavior defined by a multilinear hardening function described by multiple hardening curves.

Table 3.5: Summary of the proposed modelling approaches

Approach	Dimension	Structure	Stiffness	Hardening
3D-P-100	3D	Porous	Analytical estimate	100% behavior
3D-D-100+	3D	Dense	Analytical estimate	Multiple behaviors (50%-70%-90%-100%)
2D-P-100	2D	Porous	Analytical estimate	100% behavior
2D-D-100+	2D	Dense	Analytical estimate	Multiple behaviors (50%-70%-90%-100%)

The data from numerical simulations was used to generate the stress-strain curves for various infill densities. The process involved extracting the numerical data from FEM models. The results from the FEM models were utilized to predict the maximum normal stress along the displacement direction. This was accomplished by averaging the normal stress results across the sample. A user-defined function (EPTOX) was also used to calculate the total elastic and plastic strains along the uniaxial test direction. The stress and strain values were averaged across all the points to mitigate the effects of local anomalies or outliers. The averaged data sets were then used to construct the final predicted true stress-strain curves for all infill densities. The FEA results were used to represent the material response under tensile loading up to the UTS.

Since the FEM material models were defined up to UTS point, a perfectly plastic behavior was assumed beyond the UTS. Thus, the model was not used to predict any material behavior after the UTS. This approach ensured accurate prediction up to the maximum load-bearing capacity of the material.

CHAPTER 4

RESULTS AND DISCUSSION

This section offers a detailed examination of the mechanical properties of FDM parts, focusing on void formation, tensile behavior, and the effectiveness of analytical and computational modeling approaches. The experimental analyses presented in this work investigates the void formation in PLA FDM samples with varying infill densities. Tensile tests were also conducted to assess the mechanical properties. Analytical models were evaluated, and a new model was proposed and validated with experimental data. Computational models, employing 2D and 3D representations were also employed to simulate the mechanical behavior across various infill densities. Through comparison of computational approaches, insights were gained into optimizing the part quality and performance in FDM manufacturing.

4.1 Voids formation

The internal architecture of FDM components can be tuned by adjusting the infill pattern and density [68]. Slicing software tailored for FDM processes typically incorporates customizable infill densities and a variety of selectable infill patterns during the preprocessing phase. This allows the users to craft the final part with a desired internal structure that optimizes factors such as printing time, material costs, and part quality [64]. Generally, lower infill densities are associated with expedited and cost-effective prints, whereas higher densities are chosen to enhance part quality and structural integrity [178]. The infill density dictates the volume of material used to fill the entire part, while the infill pattern determines the toolpath through which this material is deposited. In this study, infill density serves as the primary independent variable for all parts. All other process parameters such as infill pattern, layer height, raster width, building orientation, printing speed, nozzle, and bed temperatures were maintained for all PLA FDM parts. This approach facilitates the investigation of void formation across varying infill densities.

SEM is an excellent tool to examine the voids within FDM structure with different infill densities. Specifically, samples with infill densities of 50%, 70%, and 100% were printed without shells to reveal the internal structure (**Figure 4.1**). Then, they were examined to explain the influence of infill on void morphology, size, and distribution within FDM PLA structures.

(a) (b) (c)

Figure 4.1: Printed FDM PLA samples with (a) 100%, (b)70%, and (c) 50% infill densities

Since the infill pattern was fixed, a similar trend was observed for the void distribution in all samples. All samples exhibited a periodic arrangement of skewed rectangles due to the prescribed raster angles of 45^o and -45^o for each successive layer with similar void shape and configuration. Only the air gap/void size varied between samples of different infill densities. **Figure 4.2a** illustrates the full-dense FDM PLA part without any noticeable voids in the microstructure**. Figures 4.2b-c** show the SEM images from 70% and 50% infill densities, respectively with presence of porosity between rasters.

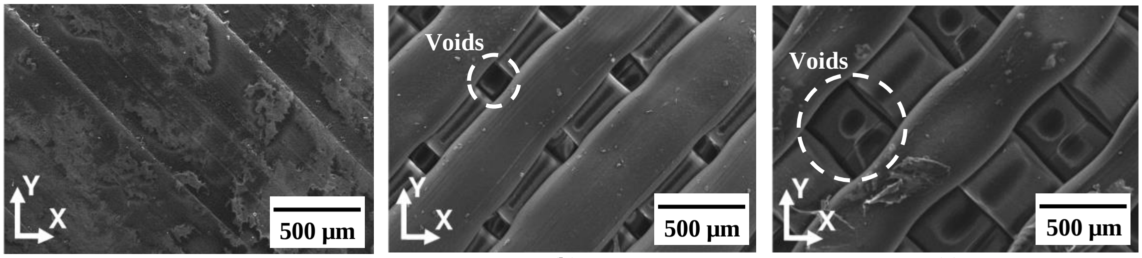

(a) (b) (c)

Figure 4.2: SEM images showing increasing voids area fractions with decreasing infill densities for (a) 100%, (b) 70%, and (c) 50% samples.

The microstructural analysis revealed three different types of void types (raster gap, sub-perimeter, and partial neck growth voids) in the printed samples. The raster gap voids are clearly visible between the rasters of each layer in **Figures 4.2 b-c**. The results show that as the infill increased, the air gaps decreased. Therefore, more rasters were printed in each layer for higher infills as shown in **Figure 4.2a**. On the other hand, sub-perimeter voids were visible around the intersection of the shells and inner infill along the toolpath direction change. These defects were also observed in the full-dense parts (**Figure 4.3**). The presence of sub-perimeter voids cannot be avoided as they are attributed to the FDM process and selected parameters [108], [179]-[180].

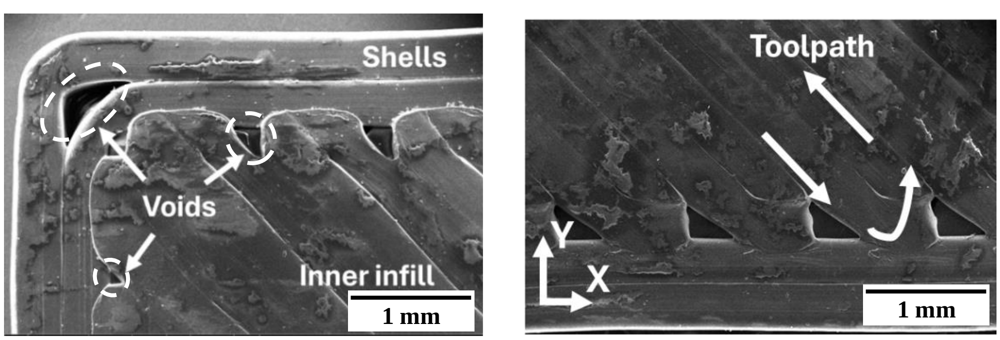

Figure 4.3: SEM images showing sub-perimeter voids between toolpath changes at contact area of shells and inner infill for full-dense parts.

Partial neck voids were also observed in the full-dense and porous samples. Cross-sectional images from the full-dense fractured tensile samples (**Figure 4.4)** show the partial neck growth between adjacent rasters and layers in full-dense parts. As voids were observed in full-dense parts, it can be concluded that a similar behavior will be observed in porous samples. On the other hand, intra-bead voids were not detected since pure PLA filament was used and intra-bead voids are commonly found in composite materials [43], [179]. In addition, infill voids were not observed in this study since complex internal architectures, such as the gyroid etc., were not used in this work [181]-[182].

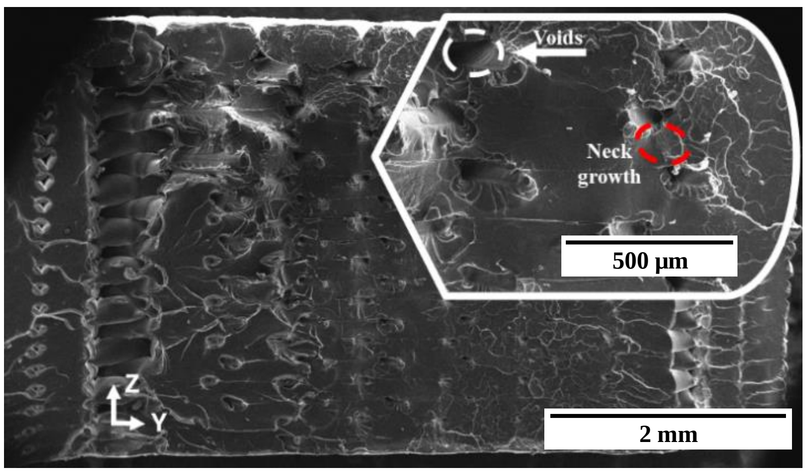

Figure 4.4: SEM image showing partial neck growth voids between adjacent rasters and layers of full-dense fractured tensile sample.

It should be mentioned that even though all samples were printed with the same raster width, it was observed that the raster width was not consistent for all samples. Only samples with higher infill density showed similar raster width. This can be seen in the SEM images from the 50%, and 70% samples (**Figure 4.2**). The SEM results from the porous 50% samples exhibited rasters with non-straight edges while the rasters from the 70% samples showed almost straight edges. This can be rationalized by the fact that as the infill density decreased, the air gap between the adjacent rasters increased. Consequently, while printing a raster on top of an air gap from a previous layer, the filament descends due to lack of support from the previous layer resulting in non-uniform edges.

In order to verify the dimensions of the generated CAD models, ImageJ® was used to quantify the average void area fractions from the SEM images. SEM images from random locations (**Figure 4.5a**) were smoothened and sharpened (**Figure 4.5b**). They were then converted into gray scale images (**Figure 4.5c)** to isolate the voids from the printed rasters. Lastly, the average area of voids for each density level was calculated (**Figure 4.5d**). The results from this image analysis were used to create the CAD models used in the FEA.

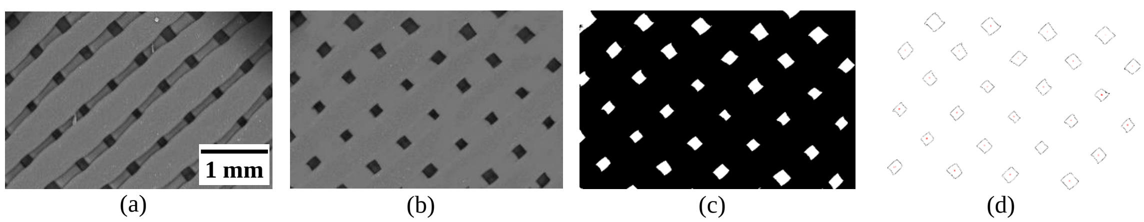

Figure 4.5: Image processing steps (a) Original SEM images, (b) enhanced image, (c) converting to gray scale, and (d) voids area fraction.

4.2 Tensile results

The tensile test results obtained from the specimens printed with infill densities of 100%, 90%, 80%, 70%, 60%, and 50% are shown in **Figure 4.6.** The tensile results reveal significant insights into the mechanical behavior of FDM parts printed with varying internal structures. As expected, specimens printed with higher infill densities exhibited increased tensile strength compared to those with lower infill densities. This trend can be attributed to the denser internal structure, which provided enhanced interlayer adhesion and resistance to deformation under tensile loading. Specifically, the specimens printed with 100% infill density exhibited the highest tensile strength, followed by the 90%, and 80 %

infill density specimens. The generated engineering stress-strain curves (**Figure 4.6**) for all infill densities were also converted into true stress-strain curves for the FEA formulation (**Figure 4.7)**. Furthermore, stiffness of the printed specimens was significantly influenced by the infill density. Lower infill densities contributed to reduced stiffness due to the presence of voids, and hence less material that could resist the tensile deformation. Conversely, similar to other FDM PLA materials, higher infill densities enhanced the stiffness [170], [183].

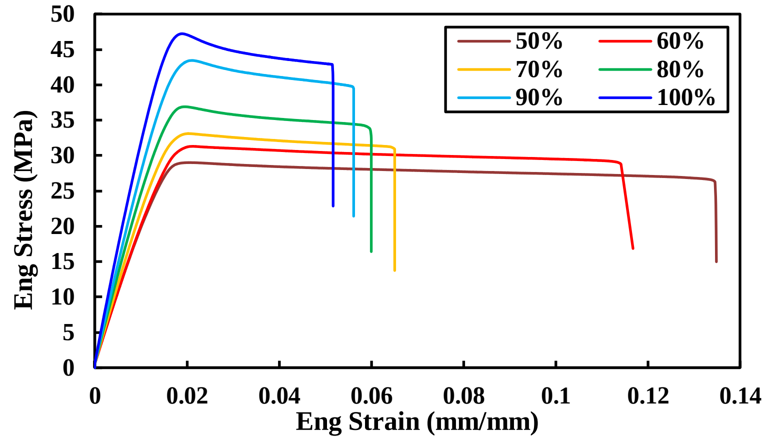

Figure 4.6: Uniaxial tensile engineering stress-strain curves for samples with varying infill densities.

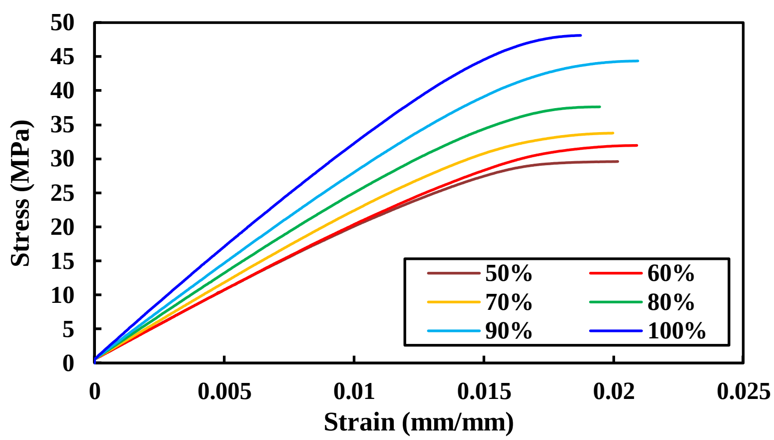

Figure 4.7: Uniaxial tensile true stress-strain curves for samples with varying infill densities.

The tensile response from the FDM PLA samples are in-line with other studies. Kasim and Owed [178] investigated PLA specimens with different speeds and infill ratios and found that increasing the infill ratio and slower speeds improved the tensile properties (UTS and E) at 100% infill.

In contrast to tensile strength, the elongation at break (**EB**) displayed a converse relationship with infill density. Specimens printed with lower infill densities exhibited a higher EB compared to those with higher infill densities. On the other hand, ductility increased with lower infill densities. This was also reported for other thermoplastic materials printed using FDM [170], [184]. This behavior can be attributed to the presence of voids and lower material density within the specimen that allowed for higher deformation before failure. Consequently, specimens with 50% infill density demonstrated the highest EB, followed by the 60% and 70% specimens.

The fracture surfaces for the printed samples were also analyzed. **Figure 4.8** shows the fracture surface of a full-dense sample. Results show a brittle fracture without the presence of any ductile features in the fracture surface (**Figure 4.8b)** or macroscopic (**Figure 4.8a)** sample. The fracture surface revealed a smooth morphology of the fracture sample with no necking due to the brittleness exhibited by pure PLA FDM samples.

(a)

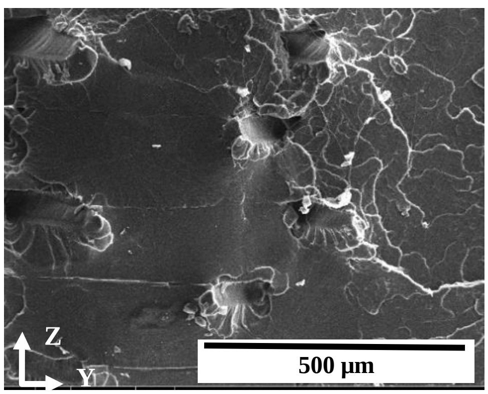

(b)

Figure 4.8: (a) Fractured full-dense tensile sample and (b) Fracture surface of a full-dense sample.

On the other hand, the 50% infill density sample showed a nonuniform fracture edge that was reflected in the noticeable increase in ductility of porous samples (**Figure 4.9a)**. The SEM analysis of the 50% infill density fracture surface demonstrated similar morphological characteristics as of the higher infill densities. However, analysis of raster failure showed elongation followed by brittle failure along the individual rasters as seen in **Figure 4.9b** [15].

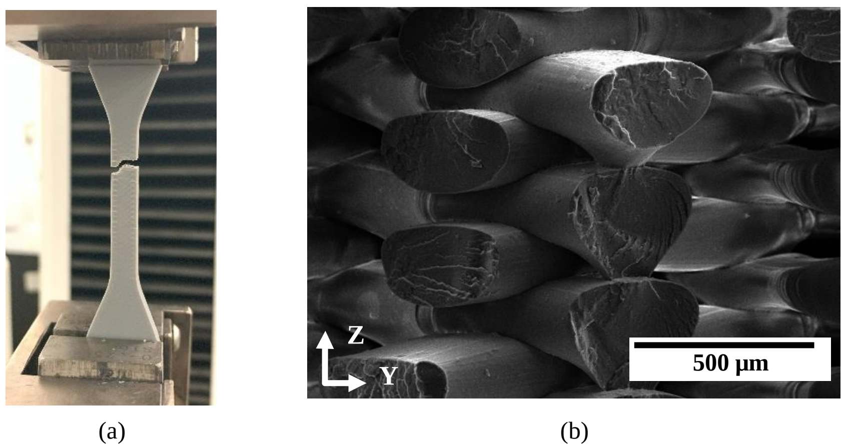

Figure 4.9: (a) Fractured 50% tensile sample and (b) Fracture surface of a 50% sample.

Although brittle fracture occurred on individual rasters in porous samples, the voids in porous samples allowed for higher localized deformations. Accordingly, samples with lower infill densities exhibited larger amount of fracture paths which elevated the ductility of printed parts. The fracture mechanics of pure PLA with other raster angles and infill pattern were also reported with similar conclusions. However, when considering PLA with reinforcements the fracture surface exhibited rough surfaces [185]-[186].

A summary of the average true UTS, YS, E, and EB are presented in **Figures 4.10a-d**. The observed experimental trends from the tensile results of FDM PLA samples highlight the importance of infill density in achieving the desired mechanical properties. Higher infill densities are favorable for applications requiring superior mechanical strength and stiffness, such as structural components or load-bearing parts. Conversely, lower infill densities may be preferred for applications that prioritize flexibility and resilience, such as soft robotics or wearable devices. By understanding the relationship between infill density and mechanical properties, designers and engineers can optimize part performance while minimizing material usage and production time.

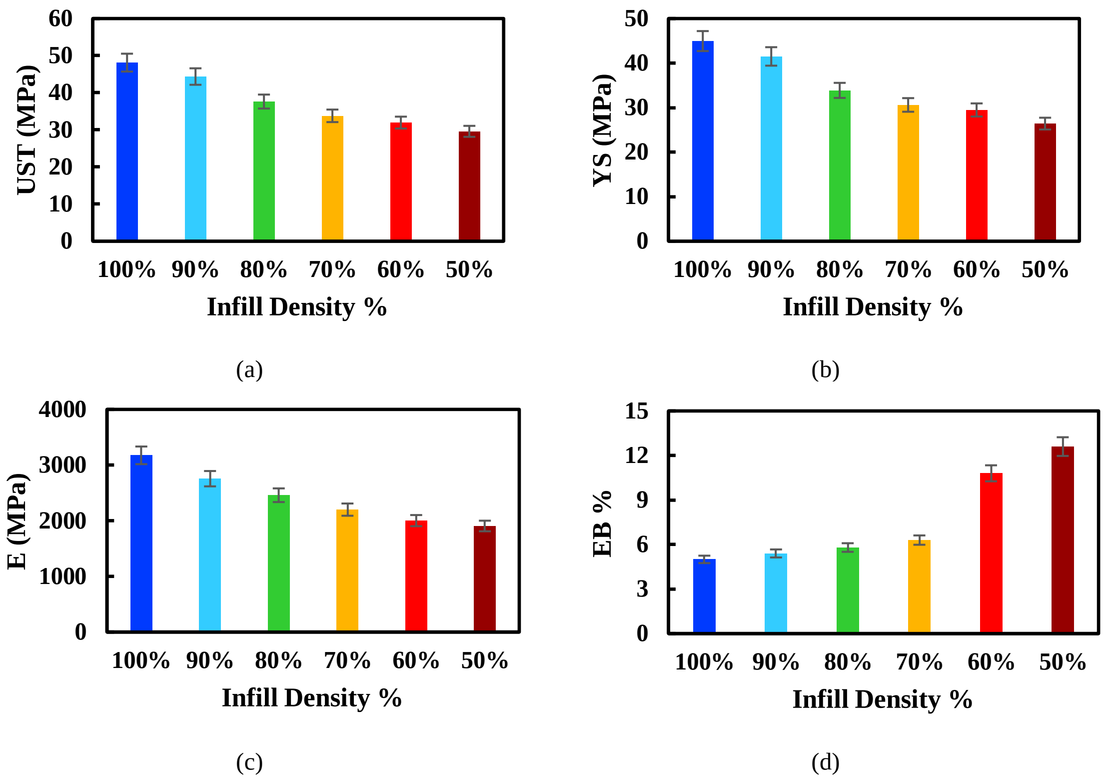

Figure 4.10: Average true results for (a) UTS, (b) YS, (c) E, and (d) EB for samples with different infill densities.

4.3 Analytical predictions of stiffness

This study investigated the predictive capabilities of existing analytical models used for estimating the stiffness of FDM parts across varying porosity levels. As discussed previously, literature presents various models to predict the stiffness of FDM parts (Section 2.4.1). Therefore, some commonly used models were assessed in this work. In addition, a new power-exponential model was proposed. To calibrate the models, the model constants were fitted using experimental data from infill densities of 90%, 70%, and 50%. Results from the 80% and 60% samples were reserved for validation. The models used in this work are summarized in **Table 4.1**.

Table 4.1: Proposed and commonly used analysis models.

Author	Equation type	Fitted Equation
Dewey [147]	Linear	$E_p = E_o(1 - 1.0483p)$
Spriggs [146]	Exponential	$E_p = E_o[exp(-1.2205p)]$
Martin and Haynes [155]	Power	$E_p = E_o(1 - 0.6445p^{2/3})$
Ramakrishnan [152]	Rational	$E_p = E_o[\frac{(1-p)^2}{(1+(-0.9364)p)}]$
Proposed equation	Power- Exponential	$E_p = E_o[exp(-1.1p^{0.91}) + p^{4.5}]$

Figure 4.11 illustrates the predictive performance of all utilized existing models against experimental results. It was observed that while all models exhibited inaccuracies for infill densities below 65%. This observation is in-agreement with other findings in literature that highlight the inaccuracies in predictions from analytical models for parts with high porosities [138]. Their results indicate that analytical models exhibit higher errors with highly porous parts, leading to inaccurate stiffness predictions.

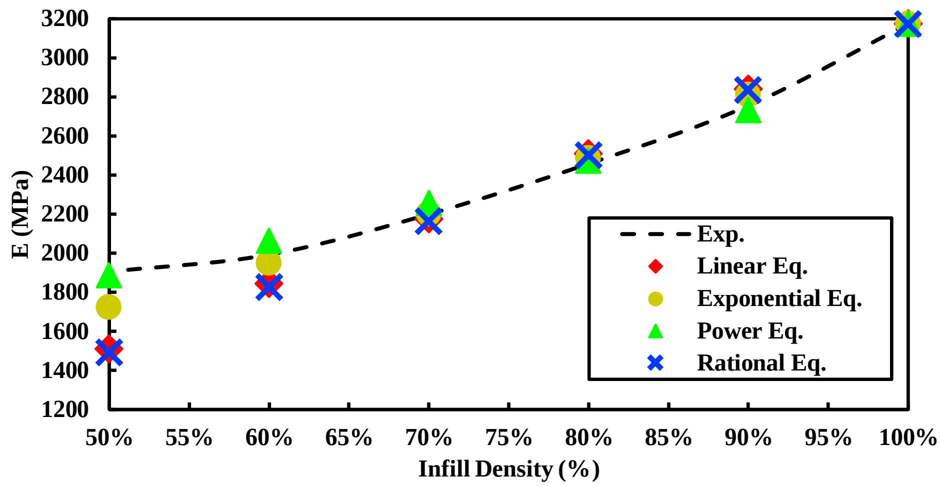

Figure 4.11: Predictions of material stiffness from commonly used analytical models for various infill densities.

The experimental results revealed a nonlinear relationship between stiffness and infill density. Notably, power, and exponential relations demonstrated superior performance compared to other models. Therefore, a power-exponential model was proposed. **Figure 4.12** illustrates the predictive capabilities of the proposed model, showcasing its alignment with the experimental data. The 50%, 70%, and 90% results were used to calibrate the model while 60% and 80% were used for validation.

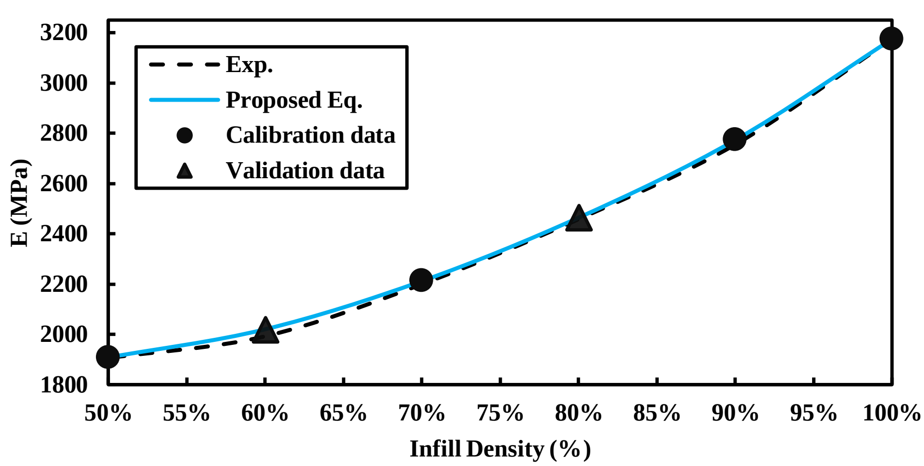

Figure 4.12: Predictions of material stiffness from the proposed analytical model for various infill densities.

Table 4.2 shows a quantitative assessment of the various models used to predict the part stiffness with varying infill densities. Analysis of the percentage errors from all models shows decent agreement with experimental results. All models exhibited high errors with 50% infill densities with the linear and rational equations showing the highest errors (20%). Analysis of the average error showed that the power equation resulted in the least average error (0.9%). However, the power relation shows a 3% error with 60% parts. It should be noted that all models show underestimation for certain infills which could lead to early failure.

The percentage errors for the proposed power-exponential relation were also calculated and are shown in **Table 4.2.** The proposed model shows the least average error (0.5%). In addition, the proposed model shows minimal errors across all infill densities. Finally, the minimal errors from the proposed model showed overestimations to assure safer predictions. Therefore, it can be concluded that the proposed model can be used to predict the stiffness of the FDM PLA parts accurately.

Table 4.2: Percentage errors from the existing and proposed analytical models for varying infill densities.

Equation	100%	90%	80%	70%	60%	50%	AVG Er%
Linear Eq.	0	3.15	2.07	-1.05	-7.91	-20.73	-4.89
Exponential Eq.	0	1.99	1.18	0.09	-2.67	-9.51	-1.78
Power Eq.	0	-0.77	0.69	2.66	3.11	-1.05	0.93
Rational Eq.	0	2.98	1.71	-1.63	-8.71	-21.69	-5.47
Proposed Eq.	0	0.65	0.25	0.57	0.92	0.13	**0.50**

This superior predictive accuracy positions the proposed model as a reliable tool for estimating the E in PLA materials printed with comparable settings. By providing rapid estimations of stiffness degradation associated with reduced infill densities, the proposed model empowers the decision-making processes in FDM. Practitioners can utilize this model as a rapid quantification method to assess the trade-offs between infill density, print speed, material usage, and part stiffness, thereby optimizing the printing strategies required to meet specific requirements. Its accuracy, ease of implementation, and potential for rapid estimation make it applicable to be used in defining the material elasticity in FEA modeling. The details of the various 2D and 3D models used in this work are given in the next section.

4.4 Computational modeling of tensile properties

4.4.1 Material models

The material inputs for the different FEM approaches are presented in this section. A combination of different elasticity and different models was used in this work. While considering the elasticity behavior, the stiffness (E) for each infill density was analytically predicted using the proposed validated power-exponential relation (**Figure 4.12)**.

Additionally, two approaches (100 and 100+) were used to describe the material hardening behavior. The 100-approach incorporated a Multilinear Isotropic Hardening model based on the full-dense samples (**Figure 4.13**). For porous models, the effect of voids was adjusted according to the plastic behavior. The 100+ approach used a porosity dependent linearly interpolating function for defining the material hardening behavior under various infill densities. The experimental results from 90%, 70%, and 50% were used to define the 100+ model (**Figure 4.13**). As the effect of porosity was captured by the porosity dependent hardening function, this enabled the simulation of porous samples without any voids in the geometry.

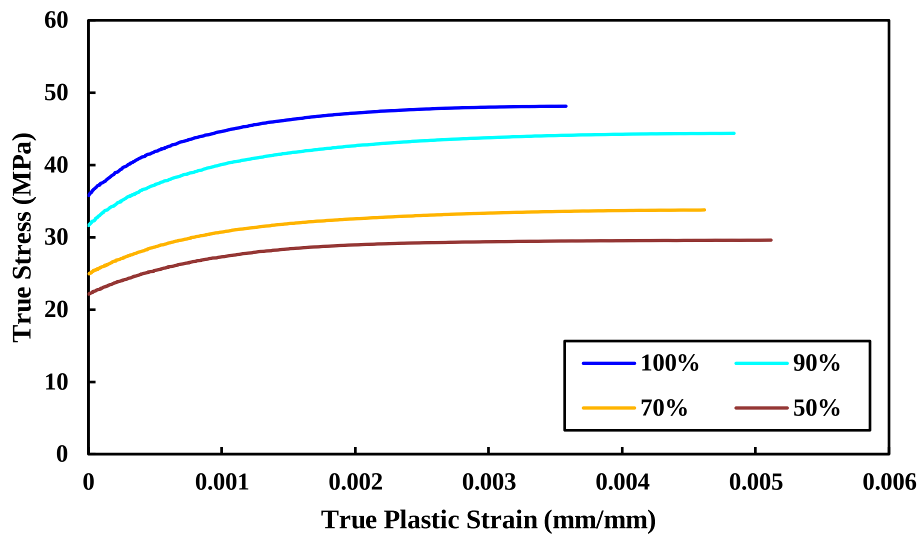

Figure 4.13: Multilinear Isotropic Hardening models used for the 100%, 90%, 70%, and 50% infill densities in 100 and 100+ approaches.

The proposed model used a linear interpolation to define the hardening behavior of a randomly selected porosity level. The hardening data from a lower (P_1) and higher (P_2) porosity level was used to interpolate the hardening value (σ) at each strain (ε) as shown in Equation 4.1.

$$\sigma(P) = \sigma(P_1) + \frac{P - P_1}{P_2 - P_1} \cdot [\sigma(P_2) - \sigma(P_1)] \tag{4.1}$$

where P_1 and P_2 are the porosity levels with defined hardening, and P is the porosity level of interest. In addition, at P_1, the hardening values are given as [($\boldsymbol{\varepsilon_1}$,$\boldsymbol{\sigma_1}$), ($\boldsymbol{\varepsilon_2}$,$\boldsymbol{\sigma_2}$), ...etc.] and at P_2, the hardening values are given as [($\boldsymbol{\varepsilon_1}$,$\boldsymbol{\sigma'_1}$), ($\boldsymbol{\varepsilon_2}$, $\boldsymbol{\sigma'_2}$), ...etc.]. If a porosity level was selected beyond the defined range, the hardening behavior from the 50% porosity level was assumed. This process ensured that the material properties reflected the appropriate porosity-dependent behavior.

The various approaches employed in this work offer flexibility in simulating the mechanical behavior of FDM parts across varying infill densities. These material models lay the foundation for conducting comprehensive computational analyses to evaluate the structural response and performance of FDM components under tensile loads.

4.4.2 Model verification

The proposed FEM models were verified based on the experimental stress-strain results from full-dense parts for the 100-type models, and from 100%, 90%, 70%, and 50% for 100+ models. A perfectly calibrated model is expected to produce perfect predictions from the verification dataset. However, as the tensile response offers a non-linear behavior, it is important to analyze the model response from the calibrated data. It should be noted that all models were used to predict the material stress-strain behavior till UTS as material softening or failure was not incorporated.

Results from all 2D and 3D models **(Figures 4.14 – 4.17)** show good agreement with experimental stress-strain results. Some variation was anticipated, as the plastic behaviors were defined based on average values from multiple tensile tests. The 2D-P-100 and 3D-P-100 approaches were verified with results from full-dense parts since (**Figures 4.14 and 4.16**). Moreover, 2D-D-100+ and 3D-D-100+ approaches were verified with 100%, 90%, 70%, and 50% data since they were used for the material definition (**Figures 4.15 and 4.17**).

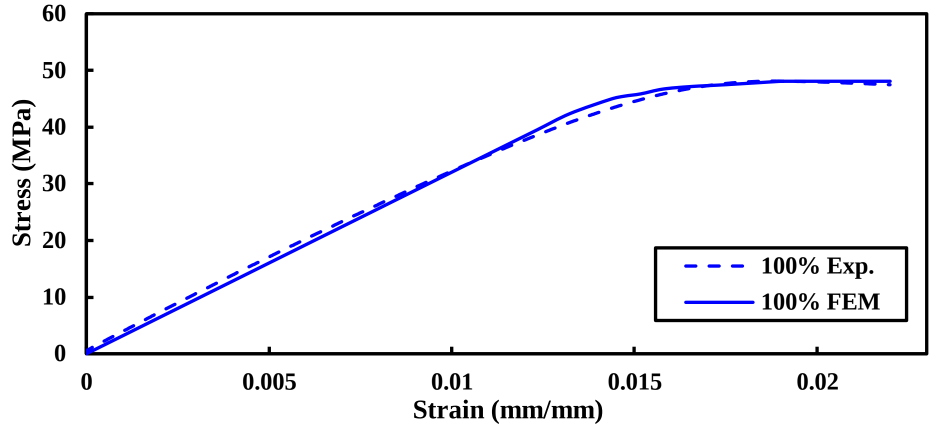

Figure 4.14: Verification results from the 2D-P-100 model for full-dense parts.

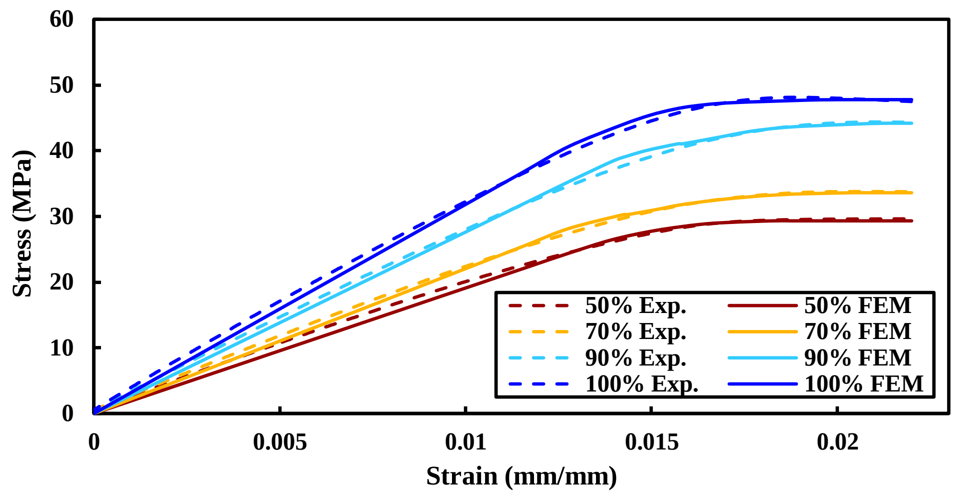

Figure 4.15: Verification results from the 2D-P-100+ model for the 50%, 70%, 90%, and 100% infill densities.

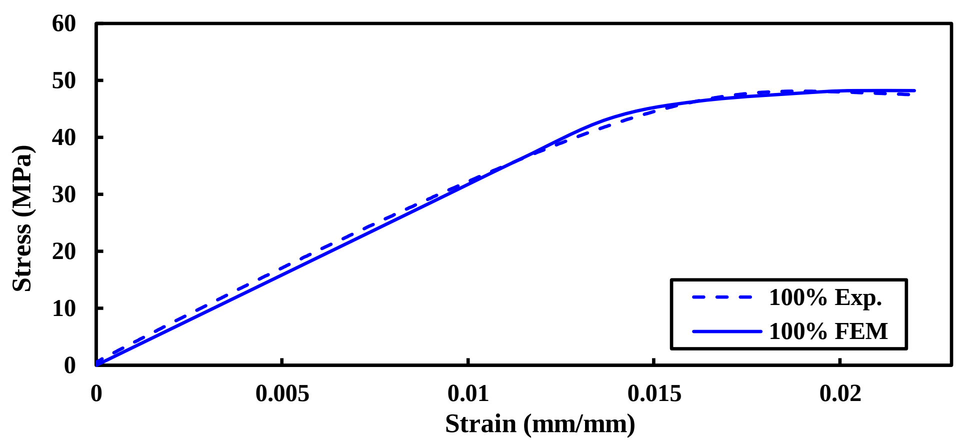

Figure 4.16: Verification results from the 3D-P-100 model for full-dense parts.

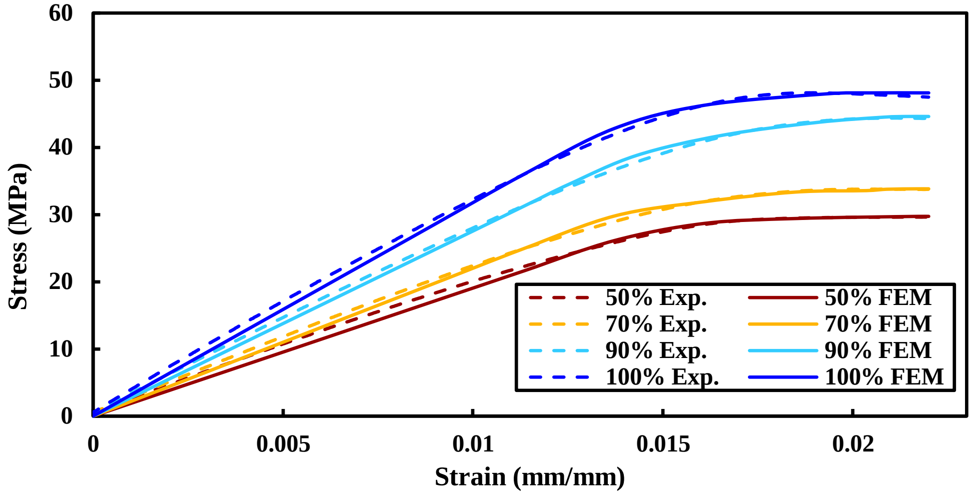

Figure 4.17: Verification results from the 2D-P-100 model for the 50%, 70%, 90%, and 100% infill densities.

A slight difference was observed between the 100 and 100+ approaches, indicating that the extended built-in function for plastic behavior altered the material's plastic response slightly. Moreover, the 3D models were reported to give slightly higher predictions in all approaches compared with the 2D models, which is generally desirable but with the expense of more computational time.

Overall, this verification of FEM models demonstrates their capability to accurately predict the tensile response of FDM parts under various infill densities. The consistency and reliability of the predictions across different modeling approaches verify their applicability in simulating the tensile structural behavior of printed components.

4.4.3 Model predictions

In this section, the predictive capabilities of the proposed FEM approaches across a range of infill densities from the 2D and 3D models are presented (**Figures 4.18 – 4.21**). The stress-strain response from all infill densities other than 100% were used to validate the 2D-P-100 and 3D-P-100 models (**Figures 4.18, and 4.20**). Whereas 60% and 80% infill densities were used to validate the 2D-D-100+ and 3D-D-100+ models (**Figures 4.19, and 4.21)**. This investigation provides valuable insights into the reliability of the proposed FEM approaches for simulating the structural response of FDM parts.

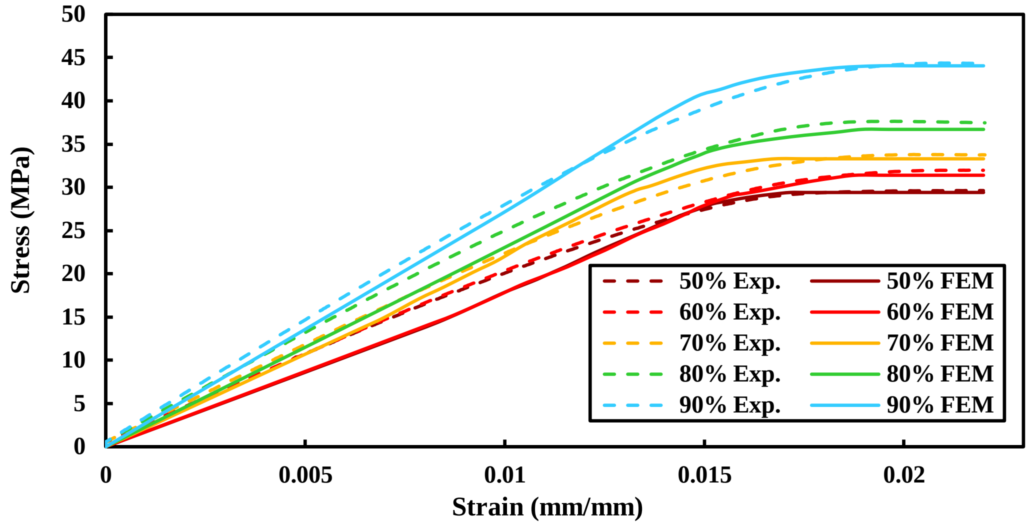

Figure 4.18: 2D-P-100 modeling approach validation results for the 50%, 60%, 70%, 80%, and 90% infill densities.

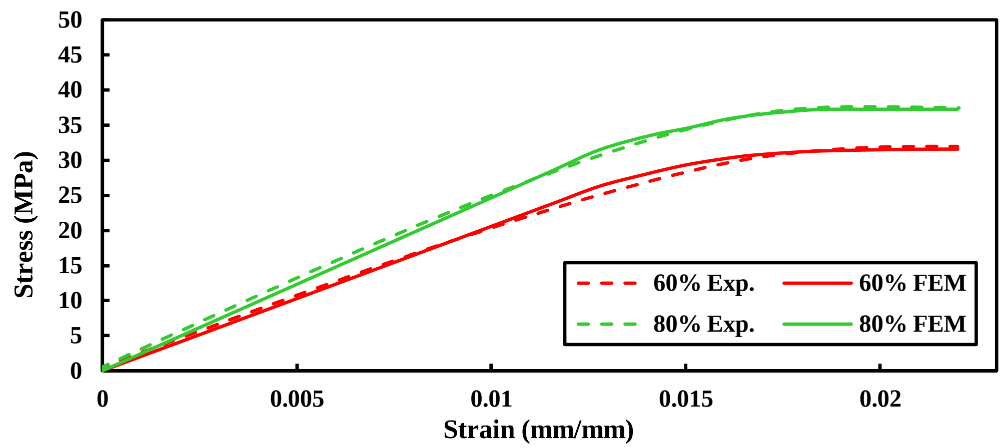

Figure 4.19: 2D-D-100+ modeling approach validation results for the 60%, and 80% infill densities.

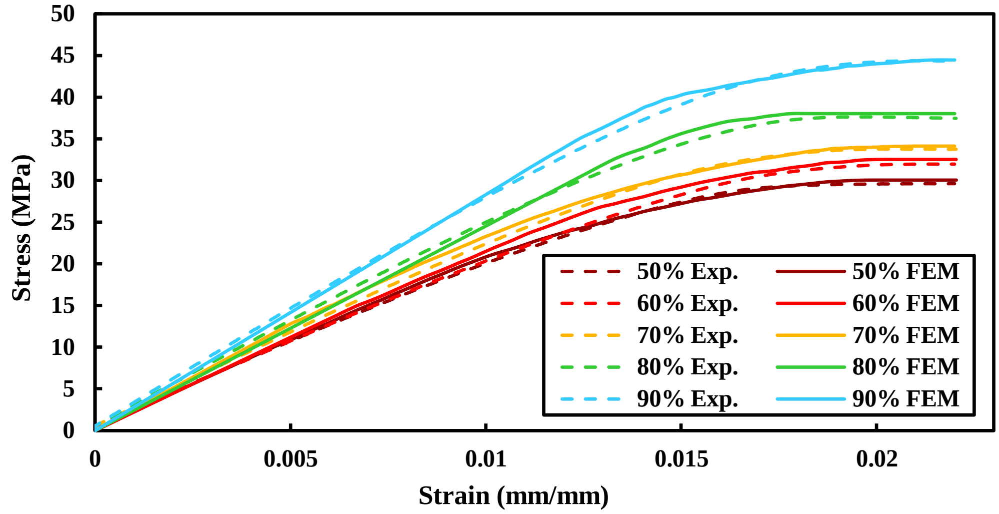

Figure 4.20: 3D-P-100 modeling approach validation results for the 50%, 60%, 70%, 80%, and 90% infill densities.

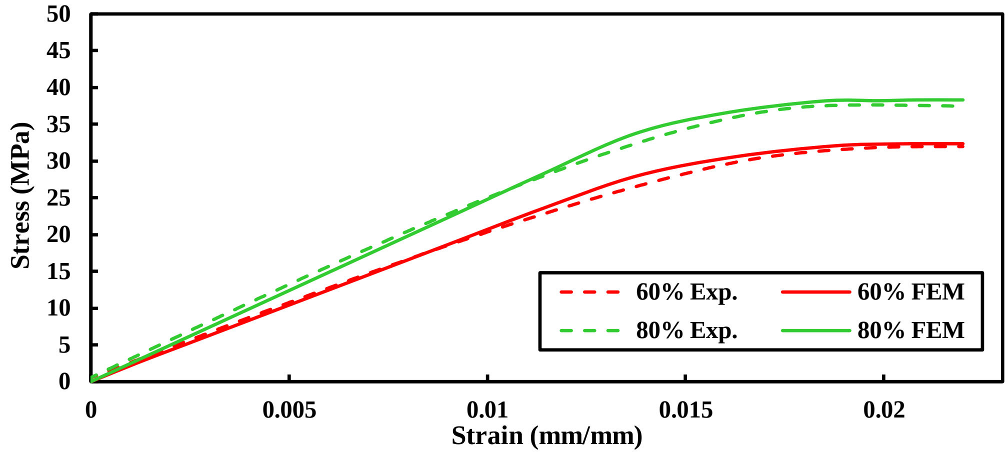

Figure 4.21: 3D-D-100+ modeling approach validation results for the 60%, and 80% infill densities.

Notably, the results from both 2D-D-100+ and 3D-D-100+ approaches demonstrated close alignment with minimal errors. Therefore, it can be concluded that the response of porous parts can be predicted with dense parts if the inputs to the material models are defined properly. The results from the 2D-P-100 and 3D-P-100 also confirmed the accuracy of the suggested approaches. **Figure 4.22** demonstrates the deformation configurations from the 2D and 3D models for dense and porous structures at 50% infill density. The results show a similar configuration across all infill densities with uniform deformation throughout the samples without any necking or stress raisers.

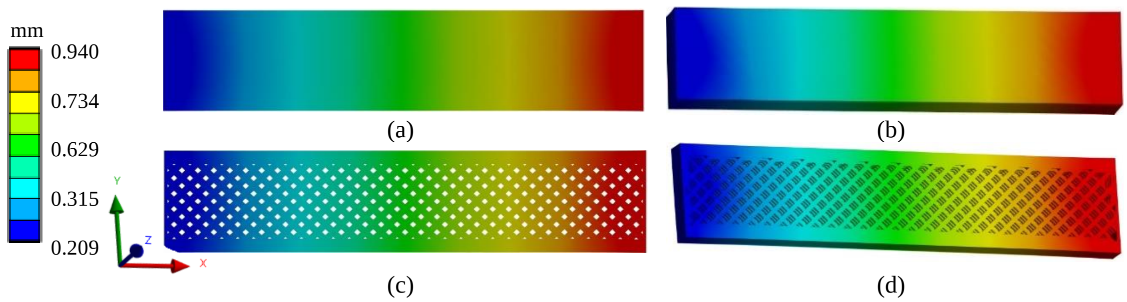

Figure 4.22: Deformation configurations for (a) 2D-Dense, (b) 3D-Dense, (c) 2D-Porous, and (d) 3D-Porous models.

In addition, the maximum normal stress distributions were obtained for both the dense and porous structures from 2D and 3D models. **Figure 4.23** presents the normal stress distribution at 50% infill densities. Results show a similar trend across all numerical models with a uniform quasi-static stress distribution that aligns with the experimental results (Section 3.1.1). This uniformity in the normal stress indicates that the proposed model distributes the applied load evenly across the structure. Thus, minimizing any stress concentrations and singularities in the simulated results. Comparable stress distributions were also reported by other researchers who observed localized stresses around the pores [64], [187]-[188]. It should be noted that Garg and Bhattacharya [15] observed localized stress concentrations due to necking.

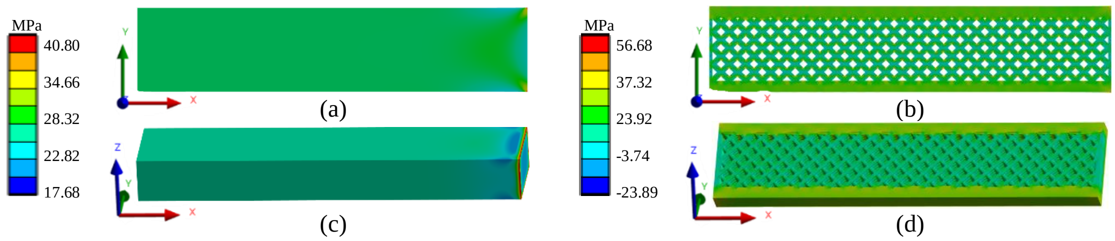

Figure 4.23: Maximum normal stress distribution for (a) 2D-Dense, (b) 2D-Porous, (c) 3D-Dense, and (d) cross section of 3D-Porous models.

Overall, the simulation results showed a good agreement with experimental data. In addition, the proposed numerical models highlight the accuracy of the FEM models in replicating the actual stress-strain response of FDM PLA parts without any erroneous errors in stress predictions due to mesh inconsistencies. Hence, the predictions from both the 2D and 3D models demonstrated robust and consistent performance across varying infill densities, verifying the applicability of the proposed modeling approaches in capturing the tensile response of FDM parts under different infill densities.

4.5 Comparison between the proposed FEM approaches

The E and UTS predictions across various FEM approaches and infill densities are compared in this section. The average percentage errors for all approaches across various infill densities for both E and UTS are summarized in **Figure 4.24**. The 3D-D-100+ model showed superiority in predicting the E (0.5%) and UTS (0.7%). The 2D-D-100+ model also showed excellent predictions but with slightly higher errors for both E (0.8) and UTS (0.8). Also, 3D models resulted in overestimations for E and UTS assuring conservative predictions. Furthermore, the 3D-P-100 and 2D-P-100 approaches gave acceptable estimations with higher average errors for both E and UTS. Interestingly, 3D-P-100 presented better predictions of E (2.5%) and UTS (1%) than the 2D-P-100 model due to geometric effects.

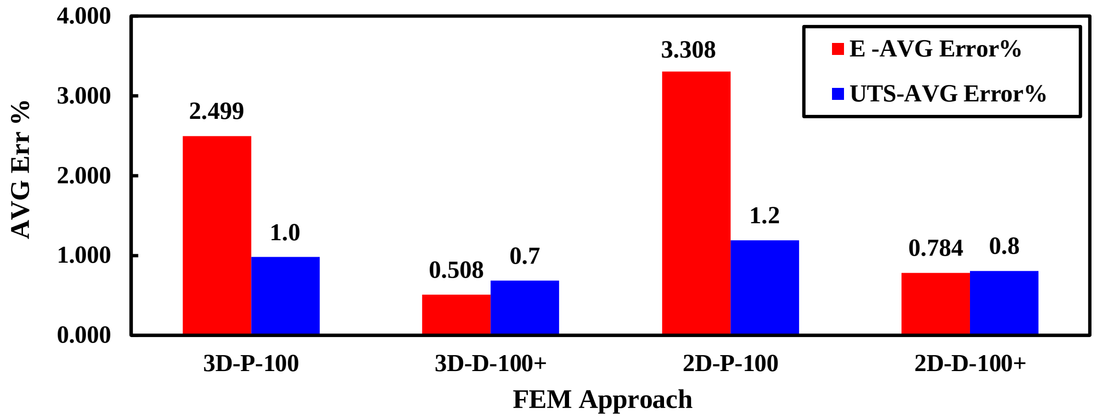

Figure 4.24: Average percentage errors from the proposed FEM approaches for E and UTS.

Table 4.3 shows the errors from all numerical simulations to analyze the individual predictions. All 100+ models outperformed the 100 models, exhibiting lower errors in stiffness predictions across both 2D and 3D models. This indicates that the extended plasticity model provided accurate estimations for E and can effectively lead to accurate estimations without incorporating voids. Generally, 3D models yield acceptable overestimations in stiffness predictions while enabling safer design considerations. The use of 2D models might be desired when quick estimations are desired. Ultimately, the lowest errors were exhibited by the 3D-D-100+ models.

In comparison with existing FEM models, the proposed approaches in this work demonstrated enhanced accuracy. For example, Kumar and Narayan [189] compared the tensile strength of PLA FDM samples with their FEM model and revealed around 15% error while the RVE model proposed by Wang et al. [162] showed around 7% percentage error.

Table 4.3: Percentage errors from the proposed models for all infill densities.

Infill %	100%		90%		80%		70%		60%		50%	
Exp. E (MPa)	3174.6	**Err%**	2755.10	**Err%**	2458.00	**Err%**	2199.20	**Err%**	1992.20	**Err%**	1905.70	**Err%**
3D-P-100	3174.0	0.02	2807.90	-1.92	2452.90	0.21	2248.00	-2.22	2127.60	-6.80	1978.80	-3.84
3D-D-100+	3174.2	0.01	2754.80	0.01	2476.80	-0.76	2198.90	0.01	2036.70	-2.23	1905.50	0.01
2D-P-100	3173.6	0.03	2718.50	1.33	2302.40	6.33	2140.80	2.66	1853.60	6.96	1857.20	2.54
2D-D-100+	3173.9	0.02	2761.20	-0.22	2463.50	-0.22	2204.10	-0.22	2048.80	-2.84	1883.40	1.17
Exp. UTS (MPa)	48.12	**Err%**	44.37	**Err%**	37.63	**Err%**	33.78	**Err%**	31.97	**Err%**	29.60	**Err%**
3D-P-100	48.21	-0.18	44.46	-0.20	38.02	-1.04	34.13	-1.02	32.53	-1.76	30.10	-1.68
3D-D-100+	48.11	0.02	44.60	-0.51	38.31	-1.80	33.83	-0.14	32.35	-1.20	29.73	-0.43
2D-P-100	48.09	0.07	44.05	0.73	36.70	2.48	33.30	1.44	31.39	1.79	29.41	0.67
2D-D-100+	47.77	0.74	44.18	0.44	37.26	0.99	33.60	0.54	31.58	1.20	29.32	0.94

Based on the findings, the 3D porous models (3D-P-100) should be selected as a suitable choice for applications where detailed experimental data is not available, providing a baseline for mechanical property estimation in FDM parts. Its simplicity and ease of implementation make it a practical option for quick assessments as only the results from the full-dense samples are required to calibrate the model. However, for enhanced accuracy and reliability, particularly in critical applications, the 3D model with modified hardening (3D-D-100+) stands out as well as the 2D-D-100+. However, the 2D-D-100+ leads to underestimations. While the 100+ approaches require additional experimental data for calibration and verification, its ability to capture the mechanical behavior of FDM parts makes it a viable option for comprehensive analyses. Therefore, depending on the specific requirements, the 2D dense approach can serve as a quick tool for estimating the material properties. On the other hand, the 3D dense model with modified hardening offers a more robust solution, albeit with the need for additional experimental validation. **Table 4.4** gives a summary of the proposed approaches.

Table 4.4: Methodology to select the modelling approaches.

Factor	Recommendation(s)	Objective(s)
Presence of Internal Voids	D-type model	Voids are neglected in design, but infill density effect is important.
	P-type model	Study of porosity evolution
Accuracy vs. Speed	3D simulation	More safe and accurate predictions.
	2D simulation	Faster with lower complexity for initial estimates.
Prediction Priority	100+ plasticity model	Prioritize accuracy
	100 plasticity model	Acceptable for most cases, offers a good balance.

CHAPTER 5

CONCLUSIONS AND RECOMMENDATIONS

5.1 Conclusions

The advancement in AM technologies has revolutionized the production of complex components with intricate geometries. In this study, various analytical and FEM were developed and validated with experimental data to simulate the tensile behavior of printed FDM PLA parts under varying infill densities (50%, 60%, 70%, 80%, 90%, and 100%). The research aimed to provide insights into the effects of voids on the tensile response of FDM parts. In addition, this work focused on enhancing the capabilities of qualifying the structural reliability of printed components with varying levels of porosity. The key findings from this research are as follows:

- Higher infill densities resulted in fewer voids. Raster gap, sub-perimeter, and partial neck growth voids were minimized with 100% infill density but could not be avoided due to process-based limitations.
- Analysis of tensile results showed that higher infill densities resulted in increased tensile strength and stiffness due to fewer voids. The UTS for 60%, 80%, and 100% infill densities were reported as 32.0, 37.6, and 48.1 MPa, respectively. While the E values for 50%, 70%, and 90% samples were recorded as 1905.7, 2199.2, and 2755 MPa, respectively.
- A reduction in infill density resulted in an increase in ductility. The reported elongation at break for 60%, 80%, and 100% were 10.8, 5.8, and 5%, respectively. Therefore, it is

suggested that engineers and designers should adjust the infill density based on the desired balance between strength and material usage.

- Several analytical models were compared to the proposed model to predict the stiffness of printed FDM parts with varying densities. Analysis of the proposed and current analytical models from literature showed the superior predictive capabilities of the proposed model. The proposed model showed an average percentage error of 0.5% across all infill densities.
- Various 2D and 3D FEA approaches were used to predict the tensile response of FDM parts. The 3D geometrical models with density-dependent multilinear hardening function (3D-D-100+) achieved a 0.5% error for E and 0.7% error for UTS. While the 2D dense model with single multilinear hardening (2D-P-100) achieved the highest errors for E (3.3%) and UTS (1.2%) predictions.
- It is proposed that dense models (D-type) are ideal for scenarios where internal voids can be neglected, while porous models (P-type) can be used for examining the effects of porosity in FDM parts. The FEM approaches proposed in this work provide valuable insights for accurate and rapid estimations of stiffness and UTS associated with the presence of voids.

5.2 Recommendations

The findings of this study offer advanced modeling approaches for predicting the mechanical behavior of FDM parts. The FEM approaches presented in this work provide a robust framework for optimizing printing strategies, enhancing part quality, and improving the overall performance of AM processes. Some recommendations for future work are given below:

- Experimental and numerical analysis on the effect of FDM process parameters and void shapes on the tensile strength of FDM parts.
- Exploring the incorporation of fracture mechanics models to simulate crack initiation and propagation in FDM parts.
- Development of analytical models to predict the material behavior under other non-proportional loading conditions.

REFERENCES

[1] M. Seifi *et al.*, “Progress Towards Metal Additive Manufacturing Standardization to Support Qualification and Certification,” *JOM*, vol. 69, no. 3, pp. 439–455, Mar. 2017, doi: 10.1007/s11837-017-2265-2.

[2] M. Seifi, A. Salem, J. Beuth, O. Harrysson, and J. J. Lewandowski, “Overview of Materials Qualification Needs for Metal Additive Manufacturing,” *JOM*, vol. 68, no. 3, pp. 747–764, Mar. 2016, doi: 10.1007/s11837-015-1810-0.

[3] D. Mahmoud, M. Magolon, J. Boer, M. A. Elbestawi, and M. G. Mohammadi, “Applications of machine learning in process monitoring and controls of l-pbf additive manufacturing: A review,” *Applied Sciences (Switzerland)*, vol. 11, no. 24. MDPI, Dec. 01, 2021. doi: 10.3390/app112411910.

[4] S. C. Altıparmak and B. Xiao, “A market assessment of additive manufacturing potential for the aerospace industry,” *J Manuf Process*, vol. 68, pp. 728–738, Aug. 2021, doi: 10.1016/j.jmapro.2021.05.072.

[5] F. Wang, “Mechanical property study on rapid additive layer manufacture Hastelloy® X alloy by selective laser melting technology,” *The International Journal of Advanced Manufacturing Technology*, vol. 58, no. 5–8, pp. 545–551, Jan. 2012, doi: 10.1007/s00170-011-3423-2.

[6] D. Popescu, A. Zapciu, C. Amza, F. Baciu, and R. Marinescu, “FDM process parameters influence over the mechanical properties of polymer specimens: A review,” *Polym Test*, vol. 69, pp. 157–166, Aug. 2018, doi: 10.1016/j.polymertesting.2018.05.020.

[7] C. U. Brown *et al.*, “The effects of laser powder bed fusion process parameters on material hardness and density for nickel alloy 625,” Gaithersburg, MD, Aug. 2018. doi: 10.6028/NIST.AMS.100-19.

[8] A. Y. Al-Maharma, S. P. Patil, and B. Markert, “Effects of porosity on the mechanical properties of additively manufactured components: a critical review,” *Mater Res Express*, vol. 7, no. 12, p. 122001, Dec. 2020, doi: 10.1088/2053-1591/abcc5d.

[9] Y. Tao *et al.*, “A review on voids of 3D printed parts by fused filament fabrication,” *Journal of Materials Research and Technology*, vol. 15, pp. 4860–4879, Nov. 2021, doi: 10.1016/j.jmrt.2021.10.108.

[10] S. A. Tronvoll, T. Welo, and C. W. Elverum, “The effects of voids on structural properties of fused deposition modelled parts: a probabilistic approach,” *The International Journal of Advanced Manufacturing Technology*, vol. 97, no. 9–12, pp. 3607–3618, Aug. 2018, doi: 10.1007/s00170-018-2148-x.

[11] J. Ghorbani, P. Koirala, Y.-L. Shen, and M. Tehrani, “Eliminating voids and reducing mechanical anisotropy in fused filament fabrication parts by adjusting the filament extrusion rate,” *J Manuf Process*, vol. 80, pp. 651–658, Aug. 2022, doi: 10.1016/j.jmapro.2022.06.026.

[12] A. Alafaghani, A. Qattawi, B. Alrawi, and A. Guzman, “Experimental Optimization of Fused Deposition Modelling Processing Parameters: A Design-for-Manufacturing Approach,” *Procedia Manuf*, vol. 10, pp. 791–803, 2017, doi: 10.1016/j.promfg.2017.07.079.

[13] Y. Zhao, Y. Chen, and Y. Zhou, “Novel mechanical models of tensile strength and elastic property of FDM AM PLA materials: Experimental and theoretical analyses,” *Mater Des*, vol. 181, p. 108089, Nov. 2019, doi: 10.1016/j.matdes.2019.108089.

[14] N. K. Maurya, V. Rastogi, and P. Singh, “Experimental and Computational Investigation on Mechanical Properties of Reinforced Additive Manufactured Component,” *Evergreen*, vol. 6, no. 3, pp. 207–214, Sep. 2019, doi: 10.5109/2349296.

[15] A. Garg and A. Bhattacharya, “An insight to the failure of FDM parts under tensile loading: finite element analysis and experimental study,” *Int J Mech Sci*, vol. 120, pp. 225–236, Jan. 2017, doi: 10.1016/j.ijmecsci.2016.11.032.

[16] P. N. B. Reis, J. A. M. Ferreira, F. V. Antunes, and M. O. W. Richardson, “Effect of Interlayer Delamination on Mechanical Behavior of Carbon/Epoxy Laminates,” *J Compos Mater*, vol. 43, no. 22, pp. 2609–2621, Oct. 2009, doi: 10.1177/0021998309344649.

[17] P. Robles Martinez, A. W. Basit, and S. Gaisford, “The History, Developments and Opportunities of Stereolithography,” 2018, pp. 55–79. doi: 10.1007/978-3-319-90755-0_4.

[18] S. Halassi, J. Semeijn, and N. Kiratli, “From consumer to prosumer: a supply chain revolution in 3D printing,” *International Journal of Physical Distribution & Logistics Management*, vol. 49, no. 2, pp. 200–216, Mar. 2019, doi: 10.1108/IJPDLM-03-2018-0139.

[19] A. K. K. Padinjareveetil and M. Pumera, “Advances in Designing 3D-Printed Systems for CO2 Reduction,” *Adv Mater Interfaces*, vol. 10, no. 8, Mar. 2023, doi: 10.1002/admi.202201734.

[20] S. Rouf *et al.*, “Additive manufacturing technologies: Industrial and medical applications,” *Sustainable Operations and Computers*, vol. 3, pp. 258–274, 2022, doi: 10.1016/j.susoc.2022.05.001.

[21] S. A. M. Tofail, E. P. Koumoulos, A. Bandyopadhyay, S. Bose, L. O’Donoghue, and C. Charitidis, “Additive manufacturing: scientific and technological challenges, market uptake and opportunities,” *Materials Today*, vol. 21, no. 1, pp. 22–37, Jan. 2018, doi: 10.1016/j.mattod.2017.07.001.

[22] B. Blakey-Milner *et al.*, “Metal additive manufacturing in aerospace: A review,” *Mater Des*, vol. 209, p. 110008, Nov. 2021, doi: 10.1016/j.matdes.2021.110008.

[23] S. Salifu, D. Desai, O. Ogunbiyi, and K. Mwale, “Recent development in the additive manufacturing of polymer-based composites for automotive structures—a review,” *The International Journal of Advanced Manufacturing Technology*, vol. 119, no. 11–12, pp. 6877–6891, Apr. 2022, doi: 10.1007/s00170-021-08569-z.

[24] B. Sun, Q. Ma, X. Wang, J. Liu, and M. R. M. Rejab, “Additive manufacturing in medical applications: A brief review,” *IOP Conf Ser Mater Sci Eng*, vol. 1078, no. 1, p. 012007, Feb. 2021, doi: 10.1088/1757-899X/1078/1/012007.

[25] A. Razavykia, E. Brusa, C. Delprete, and R. Yavari, “An Overview of Additive Manufacturing Technologies—A Review to Technical Synthesis in Numerical Study of Selective Laser Melting,” *Materials*, vol. 13, no. 17, p. 3895, Sep. 2020, doi: 10.3390/ma13173895.

[26] A. Azarniya *et al.*, “Additive manufacturing of Ti–6Al–4V parts through laser metal deposition (LMD): Process, microstructure, and mechanical properties,” *J Alloys Compd*, vol. 804, pp. 163–191, Oct. 2019, doi: 10.1016/j.jallcom.2019.04.255.

[27] J. E. Smugeresky, D. M. Keicher, J. A. Romero, M. L. Griffith, and L. D. Harwell, “Laser engineered net shaping (LENS) process: Optimization of surface finish and microstructural properties,” Albuquerque, NM, and Livermore, CA (United States), Nov. 1997. doi: 10.2172/554828.

[28] Y. Li, Q. Mao, J. Yin, Y. Wang, J. Fu, and Y. Huang, “Theoretical prediction and experimental validation of the digital light processing (DLP) working curve for photocurable materials,” *Addit Manuf*, vol. 37, p. 101716, Jan. 2021, doi: 10.1016/j.addma.2020.101716.

[29] I. Gibson, D. Rosen, B. Stucker, and M. Khorasani, *Additive Manufacturing Technologies*. Cham: Springer International Publishing, 2021. doi: 10.1007/978-3-030-56127-7.

[30] N. Guo and M. C. Leu, “Additive manufacturing: technology, applications and research needs,” *Frontiers of Mechanical Engineering*, vol. 8, no. 3, pp. 215–243, Sep. 2013, doi: 10.1007/s11465-013-0248-8.

[31] A. Keshavarzkermani *et al.*, “Controlling mechanical properties of additively manufactured hastelloy X by altering solidification pattern during laser powder-bed fusion,” *Materials Science and Engineering A*, vol. 762, Aug. 2019, doi: 10.1016/J.MSEA.2019.138081.

[32] F. Fina, A. Goyanes, S. Gaisford, and A. W. Basit, “Selective laser sintering (SLS) 3D printing of medicines,” *Int J Pharm*, vol. 529, no. 1–2, pp. 285–293, Aug. 2017, doi: 10.1016/j.ijpharm.2017.06.082.

[33] F. Fina, S. Gaisford, and A. W. Basit, “Powder Bed Fusion: The Working Process, Current Applications and Opportunities,” 2018, pp. 81–105. doi: 10.1007/978-3-319-90755-0_5.

[34] M. Marrey, E. Malekipour, H. El-Mounayri, and E. J. Faierson, “A Framework for Optimizing Process Parameters in Powder Bed Fusion (PBF) Process Using Artificial Neural Network (ANN),” *Procedia Manuf*, vol. 34, pp. 505–515, 2019, doi: 10.1016/j.promfg.2019.06.214.

[35] S. J. Trenfield, C. M. Madla, A. W. Basit, and S. Gaisford, “Binder Jet Printing in Pharmaceutical Manufacturing,” 2018, pp. 41–54. doi: 10.1007/978-3-319-90755-0_3.

[36] O. Gülcan, K. Günaydın, and A. Tamer, “The State of the Art of Material Jetting—A Critical Review,” *Polymers (Basel)*, vol. 13, no. 16, p. 2829, Aug. 2021, doi: 10.3390/polym13162829.

[37] N. Muthuram, P. Sriram Madhav, D. Keerthi Vasan, M. E. Mohan, and G. Prajeeth, “A review of recent literatures in poly jet printing process,” *Mater Today Proc*, vol. 68, pp. 1906–1920, 2022, doi: 10.1016/j.matpr.2022.08.090.

[38] A. Alomarah, D. Ruan, S. Masood, and Z. Gao, “Compressive properties of a novel additively manufactured 3D auxetic structure,” *Smart Mater Struct*, vol. 28, no. 8, p. 085019, Aug. 2019, doi: 10.1088/1361-665X/ab0dd6.

[39] B. Y. Reddy, M. Siddhartha, P. S. R. Reddy, and A. A. Lakshmi, “Influence of Process Parameters on Sheet Lamination Method-based 3D printing: A Review,”

E3S Web of Conferences, vol. 430, p. 01251, Oct. 2023, doi: 10.1051/e3sconf/202343001251.

[40] B. G. Mekonnen, G. Bright, and A. Walker, "A Study on State of the Art Technology of Laminated Object Manufacturing (LOM)," 2016, pp. 207–216. doi: 10.1007/978-81-322-2740-3_21.

[41] A. Bournias-Varotsis, X. Han, R. A. Harris, and D. S. Engstrøm, "Ultrasonic additive manufacturing using feedstock with build-in circuitry for 3D metal embedded electronics," *Addit Manuf*, vol. 29, p. 100799, Oct. 2019, doi: 10.1016/j.addma.2019.100799.

[42] Md. H. Ali, S. Kurokawa, E. Shehab, and M. Mukhtarkhanov, "Development of a large-scale multi-extrusion FDM printer, and its challenges," *International Journal of Lightweight Materials and Manufacture*, vol. 6, no. 2, pp. 198–213, Jun. 2023, doi: 10.1016/j.ijlmm.2022.10.001.

[43] S. Wickramasinghe, T. Do, and P. Tran, "FDM-Based 3D Printing of Polymer and Associated Composite: A Review on Mechanical Properties, Defects and Treatments," *Polymers (Basel)*, vol. 12, no. 7, p. 1529, Jul. 2020, doi: 10.3390/polym12071529.

[44] Y. Tao, P. Li, and L. Pan, "Improving Tensile Properties of Polylactic Acid Parts by Adjusting Printing Parameters of Open Source 3D Printers," *Materials Science*, vol. 26, no. 1, pp. 83–87, Nov. 2019, doi: 10.5755/j01.ms.26.1.20952.

[45] J. Prakash, M. Shenoy, A. Alhasmi, A. A. Al Saleh, S. G. C, and S. Shivakumar, "Biocompatibility of 3D-Printed Dental Resins: A Systematic Review," *Cureus*, Jan. 2024, doi: 10.7759/cureus.51721.

[46] J. Muñiz-Lerma, A. Nommeots-Nomm, K. Waters, and M. Brochu, "A Comprehensive Approach to Powder Feedstock Characterization for Powder Bed Fusion Additive Manufacturing: A Case Study on AlSi7Mg," *Materials*, vol. 11, no. 12, p. 2386, Nov. 2018, doi: 10.3390/ma11122386.

[47] M. Dinovitzer, X. Chen, J. Laliberte, X. Huang, and H. Frei, "Effect of wire and arc additive manufacturing (WAAM) process parameters on bead geometry and microstructure," *Addit Manuf*, vol. 26, pp. 138–146, Mar. 2019, doi: 10.1016/j.addma.2018.12.013.

[48] S. Park and K. (Kelvin) Fu, "Polymer-based filament feedstock for additive manufacturing," *Compos Sci Technol*, vol. 213, p. 108876, Sep. 2021, doi: 10.1016/j.compscitech.2021.108876.

[49] H. A. Derazkola, F. Khodabakhshi, and A. Simchi, "Evaluation of a polymer-steel laminated sheet composite structure produced by friction stir additive manufacturing (FSAM) technology," *Polym Test*, vol. 90, p. 106690, Oct. 2020, doi: 10.1016/j.polymertesting.2020.106690.

[50] J. R. C. Dizon, A. H. Espera, Q. Chen, and R. C. Advincula, "Mechanical characterization of 3D-printed polymers," *Addit Manuf*, vol. 20, pp. 44–67, Mar. 2018, doi: 10.1016/j.addma.2017.12.002.

[51] P. Charalampous, I. Kostavelis, and D. Tzovaras, "Non-destructive quality control methods in additive manufacturing: a survey," *Rapid Prototyp J*, vol. 26, no. 4, pp. 777–790, Mar. 2020, doi: 10.1108/RPJ-08-2019-0224.

[52] G. Ameta, J. Fox, and P. Witherell, "Tolerancing and Verification of Additive Manufactured Lattice with Supplemental Surfaces," *Procedia CIRP*, vol. 75, pp. 69–74, 2018, doi: 10.1016/j.procir.2018.02.023.

[53] R. G. Kim, M. Abisado, J. Villaverde, and G. A. Sampedro, "A Survey of Image-Based Fault Monitoring in Additive Manufacturing: Recent Developments and Future Directions," *Sensors*, vol. 23, no. 15, p. 6821, Jul. 2023, doi: 10.3390/s23156821.

[54] M. Pérez, D. Carou, E. M. Rubio, and R. Teti, "Current advances in additive manufacturing," *Procedia CIRP*, vol. 88, pp. 439–444, 2020, doi: 10.1016/j.procir.2020.05.076.

[55] Md. H. Ali, N. Mir-Nasiri, and W. L. Ko, "Multi-nozzle extrusion system for 3D printer and its control mechanism," *The International Journal of Advanced Manufacturing Technology*, vol. 86, no. 1–4, pp. 999–1010, Sep. 2016, doi: 10.1007/s00170-015-8205-9.

[56] M. Ramesh and K. Panneerselvam, "Mechanical investigation and optimization of parameter selection for Nylon material processed by FDM," *Mater Today Proc*, vol. 46, pp. 9303–9307, 2021, doi: 10.1016/j.matpr.2020.02.697.

[57] X. Fu, X. Zhang, and Z. Huang, "Axial crushing of Nylon and Al/Nylon hybrid tubes by FDM 3D printing," *Compos Struct*, vol. 256, p. 113055, Jan. 2021, doi: 10.1016/j.compstruct.2020.113055.

[58] T. N. A. T. Rahim, A. M. Abdullah, and H. Md Akil, "Recent Developments in Fused Deposition Modeling-Based 3D Printing of Polymers and Their Composites," *Polymer Reviews*, vol. 59, no. 4, pp. 589–624, Oct. 2019, doi: 10.1080/15583724.2019.1597883.

[59] A. Dey, I. N. Roan Eagle, and N. Yodo, "A Review on Filament Materials for Fused Filament Fabrication," *Journal of Manufacturing and Materials Processing*, vol. 5, no. 3, p. 69, Jun. 2021, doi: 10.3390/jmmp5030069.

[60] Y. Zhao, K. Zhao, Y. Li, and F. Chen, "Mechanical characterization of biocompatible PEEK by FDM," *J Manuf Process*, vol. 56, pp. 28–42, Aug. 2020, doi: 10.1016/j.jmapro.2020.04.063.

[61] S. Olivera, H. B. Muralidhara, K. Venkatesh, K. Gopalakrishna, and C. S. Vivek, "Plating on acrylonitrile–butadiene–styrene (ABS) plastic: a review," *J Mater Sci*, vol. 51, no. 8, pp. 3657–3674, Apr. 2016, doi: 10.1007/s10853-015-9668-7.

[62] Z. Liu, Y. Wang, B. Wu, C. Cui, Y. Guo, and C. Yan, "A critical review of fused deposition modeling 3D printing technology in manufacturing polylactic acid parts," *The International Journal of Advanced Manufacturing Technology*, vol. 102, no. 9–12, pp. 2877–2889, Jun. 2019, doi: 10.1007/s00170-019-03332-x.

[63] M. T. Sepahi, H. Abusalma, V. Jovanovic, and H. Eisazadeh, "Mechanical Properties of 3D-Printed Parts Made of Polyethylene Terephthalate Glycol," *J Mater Eng Perform*, vol. 30, no. 9, pp. 6851–6861, Sep. 2021, doi: 10.1007/s11665-021-06032-4.

[64] T. J. Gordelier, P. R. Thies, L. Turner, and L. Johanning, "Optimising the FDM additive manufacturing process to achieve maximum tensile strength: a state-of-the-art review," *Rapid Prototyp J*, vol. 25, no. 6, pp. 953–971, Jul. 2019, doi: 10.1108/RPJ-07-2018-0183.

[65] T. Makki *et al.*, "3D and 4D Printing: A Review of Virgin Polymers Used in Fused Deposition Modeling," *Composites Part C: Open Access*, p. 100472, May 2024, doi: 10.1016/j.jcomc.2024.100472.

[66] I. Durgun and R. Ertan, "Experimental investigation of FDM process for improvement of mechanical properties and production cost," *Rapid Prototyp J*, vol. 20, no. 3, pp. 228–235, Apr. 2014, doi: 10.1108/RPJ-10-2012-0091.

[67] J. M. Chacón, M. A. Caminero, E. García-Plaza, and P. J. Núñez, "Additive manufacturing of PLA structures using fused deposition modelling: Effect of process parameters on mechanical properties and their optimal selection," *Mater Des*, vol. 124, pp. 143–157, Jun. 2017, doi: 10.1016/j.matdes.2017.03.065.

[68] D. Syrlybayev, B. Zharylkassyn, A. Seisekulova, M. Akhmetov, A. Perveen, and D. Talamona, "Optimisation of Strength Properties of FDM Printed Parts—A Critical Review," *Polymers (Basel)*, vol. 13, no. 10, p. 1587, May 2021, doi: 10.3390/polym13101587.

[69] A. Chadha, M. I. Ul Haq, A. Raina, R. R. Singh, N. B. Penumarti, and M. S. Bishnoi, "Effect of fused deposition modelling process parameters on mechanical properties of 3D printed parts," *World Journal of Engineering*, vol. 16, no. 4, pp. 550–559, Jul. 2019, doi: 10.1108/WJE-09-2018-0329.

[70] B. Rankouhi, S. Javadpour, F. Delfanian, and T. Letcher, "Failure Analysis and Mechanical Characterization of 3D Printed ABS With Respect to Layer Thickness and Orientation," *Journal of Failure Analysis and Prevention*, vol. 16, no. 3, pp. 467–481, Jun. 2016, doi: 10.1007/s11668-016-0113-2.

[71] A. K. Sood, R. K. Ohdar, and S. S. Mahapatra, "Parametric appraisal of mechanical property of fused deposition modelling processed parts," *Mater Des*, vol. 31, no. 1, pp. 287–295, Jan. 2010, doi: 10.1016/j.matdes.2009.06.016.

[72] J. C. Najmon, S. Raeisi, and A. Tovar, "Review of additive manufacturing technologies and applications in the aerospace industry," in *Additive Manufacturing for the Aerospace Industry*, Elsevier, 2019, pp. 7–31. doi: 10.1016/B978-0-12-814062-8.00002-9.

[73] S. Ahn, M. Montero, D. Odell, S. Roundy, and P. K. Wright, "Anisotropic material properties of fused deposition modeling ABS," *Rapid Prototyp J*, vol. 8, no. 4, pp. 248–257, Oct. 2002, doi: 10.1108/13552540210441166.

[74] M. F. Afrose, S. H. Masood, P. Iovenitti, M. Nikzad, and I. Sbarski, "Effects of part build orientations on fatigue behaviour of FDM-processed PLA material," *Progress in Additive Manufacturing*, vol. 1, no. 1–2, pp. 21–28, Jun. 2016, doi: 10.1007/s40964-015-0002-3.

[75] W. Wu, P. Geng, G. Li, D. Zhao, H. Zhang, and J. Zhao, "Influence of Layer Thickness and Raster Angle on the Mechanical Properties of 3D-Printed PEEK and a Comparative Mechanical Study between PEEK and ABS," *Materials*, vol. 8, no. 9, pp. 5834–5846, Sep. 2015, doi: 10.3390/ma8095271.

[76] N. Hill and M. Haghi, "Deposition direction-dependent failure criteria for fused deposition modeling polycarbonate," *Rapid Prototyp J*, vol. 20, no. 3, pp. 221–227, Apr. 2014, doi: 10.1108/RPJ-04-2013-0039.

[77] H. Rezayat, W. Zhou, A. Siriruk, D. Penumadu, and S. S. Babu, "Structure–mechanical property relationship in fused deposition modelling," *Materials Science and Technology*, vol. 31, no. 8, pp. 895–903, Jun. 2015, doi: 10.1179/1743284715Y.0000000010.

[78] F. Rayegani and G. C. Onwubolu, "Fused deposition modelling (FDM) process parameter prediction and optimization using group method for data handling

(GMDH) and differential evolution (DE)," *The International Journal of Advanced Manufacturing Technology*, vol. 73, no. 1–4, pp. 509–519, Jul. 2014, doi: 10.1007/s00170-014-5835-2.

[79] B. Aloyaydi, S. Sivasankaran, and A. Mustafa, "Investigation of infill-patterns on mechanical response of 3D printed poly-lactic-acid," *Polym Test*, vol. 87, p. 106557, Jul. 2020, doi: 10.1016/j.polymertesting.2020.106557.

[80] G. W. Melenka, J. S. Schofield, M. R. Dawson, and J. P. Carey, "Evaluation of dimensional accuracy and material properties of the MakerBot 3D desktop printer," *Rapid Prototyp J*, vol. 21, no. 5, pp. 618–627, Aug. 2015, doi: 10.1108/RPJ-09-2013-0093.

[81] P. Ramkumar, "Investigation on the Effect of Process Parameters on Impact Strength of Fused Deposition Modelling Specimens," *IOP Conf Ser Mater Sci Eng*, vol. 491, p. 012026, Mar. 2019, doi: 10.1088/1757-899X/491/1/012026.

[82] M. S. Kamer, Ş. Temiz, H. Yaykaşli, A. Kaya, and O. AKAY, "Effect of Printing Speed on FDM 3D-Printed PLA Samples Produced Using Different Two Printers," *International Journal of 3D Printing Technologies and Digital Industry*, vol. 6, no. 3, pp. 438–448, Dec. 2022, doi: 10.46519/ij3dptdi.1088805.

[83] P. Wolszczak, K. Lygas, M. Paszko, and R. A. Wach, "Heat distribution in material during fused deposition modelling," *Rapid Prototyp J*, vol. 24, no. 3, pp. 615–622, Apr. 2018, doi: 10.1108/RPJ-04-2017-0062.

[84] M. Baechle-Clayton, E. Loos, M. Taheri, and H. Taheri, "Failures and Flaws in Fused Deposition Modeling (FDM) Additively Manufactured Polymers and Composites," *Journal of Composites Science*, vol. 6, no. 7, p. 202, Jul. 2022, doi: 10.3390/jcs6070202.

[85] S. Tammas-Williams, P. J. Withers, I. Todd, and P. B. Prangnell, "The Influence of Porosity on Fatigue Crack Initiation in Additively Manufactured Titanium Components," *Sci Rep*, vol. 7, no. 1, Dec. 2017, doi: 10.1038/s41598-017-06504-5.

[86] T. Hofstätter, D. B. Pedersen, G. Tosello, and H. N. Hansen, "State-of-the-art of fiber-reinforced polymers in additive manufacturing technologies," *Journal of Reinforced Plastics and Composites*, vol. 36, no. 15, pp. 1061–1073, Aug. 2017, doi: 10.1177/0731684417695648.

[87] S. Thuketana, C. Taute, H. Möller, and A. du Plessis, "Characterization of surface roughness and subsurface pores and their effect on corrosion in 3D-printed

AlSilOMg," *J South Afr Inst Min Metall*, vol. 120, no. 6, 2020, doi: 10.17159/2411-9717/1053/2020.

[88] A. R. Moustafa, R. B. Dinwiddie, A. E. Pawlowski, D. A. Splitter, A. Shyam, and Z. C. Cordero, "Mesostructure and porosity effects on the thermal conductivity of additively manufactured interpenetrating phase composites," *Addit Manuf*, vol. 22, pp. 223–229, Aug. 2018, doi: 10.1016/j.addma.2018.05.018.

[89] B. Brenken, E. Barocio, A. Favaloro, V. Kunc, and R. B. Pipes, "Fused filament fabrication of fiber-reinforced polymers: A review," *Addit Manuf*, vol. 21, pp. 1–16, May 2018, doi: 10.1016/j.addma.2018.01.002.

[90] C. Hu and Q.-H. Qin, "Advances in fused deposition modeling of discontinuous fiber/polymer composites," *Curr Opin Solid State Mater Sci*, vol. 24, no. 5, p. 100867, Oct. 2020, doi: 10.1016/j.cossms.2020.100867.

[91] N. van de Werken, H. Tekinalp, P. Khanbolouki, S. Ozcan, A. Williams, and M. Tehrani, "Additively manufactured carbon fiber-reinforced composites: State of the art and perspective," *Addit Manuf*, vol. 31, p. 100962, Jan. 2020, doi: 10.1016/j.addma.2019.100962.

[92] C. Bellehumeur, L. Li, Q. Sun, and P. Gu, "Modeling of Bond Formation Between Polymer Filaments in the Fused Deposition Modeling Process," *J Manuf Process*, vol. 6, no. 2, pp. 170–178, Jan. 2004, doi: 10.1016/S1526-6125(04)70071-7.

[93] P. K. Penumakala, J. Santo, and A. Thomas, "A critical review on the fused deposition modeling of thermoplastic polymer composites," *Compos B Eng*, vol. 201, p. 108336, Nov. 2020, doi: 10.1016/j.compositesb.2020.108336.

[94] X. Xiao, V. S. Chevali, P. Song, D. He, and H. Wang, "Polylactide/hemp hurd biocomposites as sustainable 3D printing feedstock," *Compos Sci Technol*, vol. 184, p. 107887, Nov. 2019, doi: 10.1016/j.compscitech.2019.107887.

[95] S.S. Balasubramanian, C. Philpott, J. Hyder, M. Corliss, B. Tai, and W. N. Hung, "Testing Techniques and Fatigue of Additively Manufactured Inconel 718 – A Review," *International Journal of Engineering Materials and Manufacture*, vol. 5, no. 4, pp. 156–194, Oct. 2020, doi: 10.26776/ijemm.05.04.2020.05.

[96] E. G. Gordeev, A. S. Galushko, and V. P. Ananikov, "Improvement of quality of 3D printed objects by elimination of microscopic structural defects in fused deposition modeling," *PLoS One*, vol. 13, no. 6, p. e0198370, Jun. 2018, doi: 10.1371/journal.pone.0198370.

[97] O. A. Mohamed, S. H. Masood, and J. L. Bhowmik, “Optimization of fused deposition modeling process parameters: a review of current research and future prospects,” *Adv Manuf*, vol. 3, no. 1, pp. 42–53, Mar. 2015, doi: 10.1007/s40436-014-0097-7.

[98] Y. Tao, L. Pan, D. Liu, and P. Li, “A case study: Mechanical modeling optimization of cellular structure fabricated using wood flour-filled polylactic acid composites with fused deposition modeling,” *Compos Struct*, vol. 216, pp. 360–365, May 2019, doi: 10.1016/j.compstruct.2019.03.010.

[99] L. Li, Q. Sun, C. Bellehumeur, and P. Gu, “Composite Modeling and Analysis for Fabrication of FDM Prototypes with Locally Controlled Properties,” *J Manuf Process*, vol. 4, no. 2, pp. 129–141, Jan. 2002, doi: 10.1016/S1526-6125(02)70139-4.

[100] B. N. Turner and S. A. Gold, “A review of melt extrusion additive manufacturing processes: II. Materials, dimensional accuracy, and surface roughness,” *Rapid Prototyp J*, vol. 21, no. 3, pp. 250–261, Apr. 2015, doi: 10.1108/RPJ-02-2013-0017.

[101] A. Bellini and S. Güçeri, “Mechanical characterization of parts fabricated using fused deposition modeling,” *Rapid Prototyp J*, vol. 9, no. 4, pp. 252–264, Oct. 2003, doi: 10.1108/13552540310489631.

[102] S. Guessasma, S. Belhabib, and H. Nouri, “Effect of printing temperature on microstructure, thermal behavior and tensile properties of 3D printed nylon using fused deposition modeling,” *J Appl Polym Sci*, vol. 138, no. 14, Apr. 2021, doi: 10.1002/app.50162.

[103] P. K. Gurrala and S. P. Regalla, “Part strength evolution with bonding between filaments in fused deposition modelling,” *Virtual Phys Prototyp*, vol. 9, no. 3, pp. 141–149, Jul. 2014, doi: 10.1080/17452759.2014.913400.

[104] N. D. Polychronopoulos and J. Vlachopoulos, “The role of heating and cooling in viscous sintering of pairs of spheres and pairs of cylinders,” *Rapid Prototyp J*, vol. 26, no. 4, pp. 719–726, Jan. 2020, doi: 10.1108/RPJ-06-2019-0162.

[105] D. Bhalodi, K. Zalavadiya, and P. K. Gurrala, “Influence of temperature on polymer parts manufactured by fused deposition modeling process,” *Journal of the Brazilian Society of Mechanical Sciences and Engineering*, vol. 41, no. 3, p. 113, Mar. 2019, doi: 10.1007/s40430-019-1616-z.

[106] B. Huang and S. Singamneni, “Raster angle mechanics in fused deposition modelling,” *J Compos Mater*, vol. 49, no. 3, pp. 363–383, Feb. 2015, doi: 10.1177/0021998313519153.

[107] Q. Sun, G. M. Rizvi, C. T. Bellehumeur, and P. Gu, “Effect of processing conditions on the bonding quality of FDM polymer filaments,” *Rapid Prototyp J*, vol. 14, no. 2, pp. 72–80, Mar. 2008, doi: 10.1108/13552540810862028.

[108] M. K. Agarwala, V. R. Jamalabad, N. A. Langrana, A. Safari, P. J. Whalen, and S. C. Danforth, “Structural quality of parts processed by fused deposition,” *Rapid Prototyp J*, vol. 2, no. 4, pp. 4–19, Dec. 1996, doi: 10.1108/13552549610732034.

[109] H. L. Tekinalp *et al.*, “Highly oriented carbon fiber–polymer composites via additive manufacturing,” *Compos Sci Technol*, vol. 105, pp. 144–150, Dec. 2014, doi: 10.1016/j.compscitech.2014.10.009.

[110] D. Downing, A. Jones, M. Brandt, and M. Leary, “Increased efficiency gyroid structures by tailored material distribution,” *Mater Des*, vol. 197, p. 109096, Jan. 2021, doi: 10.1016/j.matdes.2020.109096.

[111] M. Spoerk, F. Arbeiter, H. Cajner, J. Sapkota, and C. Holzer, “Parametric optimization of intra- and inter-layer strengths in parts produced by extrusion-based additive manufacturing of poly(lactic acid),” *J Appl Polym Sci*, vol. 134, no. 41, Nov. 2017, doi: 10.1002/app.45401.

[112] X. Gao, S. Qi, D. Zhang, Y. Su, and D. Wang, “The role of poly (ethylene glycol) on crystallization, interlayer bond and mechanical performance of polylactide parts fabricated by fused filament fabrication,” *Addit Manuf*, vol. 35, p. 101414, Oct. 2020, doi: 10.1016/j.addma.2020.101414.

[113] N. Aliheidari, J. Christ, R. Tripuraneni, S. Nadimpalli, and A. Ameli, “Interlayer adhesion and fracture resistance of polymers printed through melt extrusion additive manufacturing process,” *Mater Des*, vol. 156, pp. 351–361, Oct. 2018, doi: 10.1016/j.matdes.2018.07.001.

[114] A. C. Abbott, G. P. Tandon, R. L. Bradford, H. Koerner, and J. W. Baur, “Process-structure-property effects on ABS bond strength in fused filament fabrication,” *Addit Manuf*, vol. 19, pp. 29–38, Jan. 2018, doi: 10.1016/j.addma.2017.11.002.

[115] D. Vaes and P. Van Puyvelde, “Semi-crystalline feedstock for filament-based 3D printing of polymers,” *Prog Polym Sci*, vol. 118, p. 101411, Jul. 2021, doi: 10.1016/j.progpolymsci.2021.101411.

[116] L. Wang, W. M. Gramlich, and D. J. Gardner, “Improving the impact strength of Poly(lactic acid) (PLA) in fused layer modeling (FLM),” *Polymer (Guildf)*, vol. 114, pp. 242–248, Apr. 2017, doi: 10.1016/j.polymer.2017.03.011.

[117] L. Wang and D. J. Gardner, “Effect of fused layer modeling (FLM) processing parameters on impact strength of cellular polypropylene,” *Polymer (Guildf)*, vol. 113, pp. 74–80, Mar. 2017, doi: 10.1016/j.polymer.2017.02.055.

[118] C. A. Butler, R. L. Mccullough, R. Pitchumani, and J. W. Gillespie, “An Analysis of Mechanisms Governing Fusion Bonding of Thermoplastic Composites,” *Journal of Thermoplastic Composite Materials*, vol. 11, no. 4, pp. 338–363, Jul. 1998, doi: 10.1177/089270579801100404.

[119] C. Abeykoon, P. Sri-Amphorn, and A. Fernando, “Optimization of fused deposition modeling parameters for improved PLA and ABS 3D printed structures,” *International Journal of Lightweight Materials and Manufacture*, vol. 3, no. 3, pp. 284–297, Sep. 2020, doi: 10.1016/j.ijlmm.2020.03.003.

[120] W. W. Wits, S. Carmignato, F. Zanini, and T. H. J. Vaneker, “Porosity testing methods for the quality assessment of selective laser melted parts,” *CIRP Annals*, vol. 65, no. 1, pp. 201–204, 2016, doi: 10.1016/j.cirp.2016.04.054.

[121] J. Laureto, J. Tomasi, J. A. King, and J. M. Pearce, “Thermal properties of 3-D printed polylactic acid-metal composites,” *Progress in Additive Manufacturing*, vol. 2, no. 1–2, pp. 57–71, Jun. 2017, doi: 10.1007/s40964-017-0019-x.

[122] J. J. Bensch and H. J. Brynard, “New Approach to Density Measurements using Archimedes’s Principle,” *Nature Physical Science*, vol. 239, no. 93, pp. 96–96, Oct. 1972, doi: 10.1038/physci239096a0.

[123] A.-F. Obaton *et al.*, “Investigation of new volumetric non-destructive techniques to characterise additive manufacturing parts,” *Welding in the World*, vol. 62, no. 5, pp. 1049–1057, Sep. 2018, doi: 10.1007/s40194-018-0593-7.

[124] A. M. Sereno, M. A. Silva, and L. Mayor, “Determination of Particle Density and Porosity in Foods and Porous Materials with High Moisture Content,” *Int J Food Prop*, vol. 10, no. 3, pp. 455–469, Jul. 2007, doi: 10.1080/10942910600880736.

[125] A. Le Duigou, M. Castro, R. Bevan, and N. Martin, “3D printing of wood fibre biocomposites: From mechanical to actuation functionality,” *Mater Des*, vol. 96, pp. 106–114, Apr. 2016, doi: 10.1016/j.matdes.2016.02.018.

[126] J. A. Slotwinski, E. J. Garboczi, and K. M. Hebenstreit, "Porosity measurements and analysis for metal additive manufacturing process control," *J Res Natl Inst Stand Technol*, vol. 119, pp. 494–528, 2014, doi: 10.6028/jres.119.019.

[127] A. du Plessis *et al.*, "Standard method for microCT-based additive manufacturing quality control 2: Density measurement," *MethodsX*, vol. 5, pp. 1117–1123, 2018, doi: 10.1016/j.mex.2018.09.006.

[128] S. Carmignato, W. Dewulf, and R. Leach, Eds., Industrial X-Ray Computed Tomography. Cham: Springer International Publishing, 2017. doi: 10.1007/978-3-319-59573-3.

[129] D. Yang, H. Zhang, J. Wu, and E. D. McCarthy, "Fibre flow and void formation in 3D printing of short-fibre reinforced thermoplastic composites: An experimental benchmark exercise," *Addit Manuf*, vol. 37, p. 101686, Jan. 2021, doi: 10.1016/j.addma.2020.101686.

[130] A. S. Mohammed, M. Almutahhar, K. Sattar, A. Alhajeri, A. Nazir, and U. Ali, "Deep learning based porosity prediction for additively manufactured laser powder-bed fusion parts," *Journal of Materials Research and Technology*, vol. 27, pp. 7330–7335, Nov. 2023, doi: 10.1016/j.jmrt.2023.11.130.

[131] H. Nouri, S. Guessasma, and S. Belhabib, "Structural imperfections in additive manufacturing perceived from the X-ray micro-tomography perspective," *J Mater Process Technol*, vol. 234, pp. 113–124, Aug. 2016, doi: 10.1016/j.jmatprotec.2016.03.019.

[132] M. P. Serdeczny, R. Comminal, D. B. Pedersen, and J. Spangenberg, "Numerical simulations of the mesostructure formation in material extrusion additive manufacturing," *Addit Manuf*, vol. 28, pp. 419–429, Aug. 2019, doi: 10.1016/j.addma.2019.05.024.

[133] S. Sommacal, A. Matschinski, K. Drechsler, and P. Compston, "Characterisation of void and fiber distribution in 3D printed carbon-fiber/PEEK using X-ray computed tomography," *Compos Part A Appl Sci Manuf*, vol. 149, p. 106487, Oct. 2021, doi: 10.1016/j.compositesa.2021.106487.

[134] N. P. Levenhagen and M. D. Dadmun, "Bimodal molecular weight samples improve the isotropy of 3D printed polymeric samples," *Polymer (Guildf)*, vol. 122, pp. 232–241, Jul. 2017, doi: 10.1016/j.polymer.2017.06.057.

[135] M. Wu, V. V. Phoha, Y. B. Moon, and A. K. Belman, "Detecting Malicious Defects in 3D Printing Process Using Machine Learning and Image Classification," in *Volume 14: Emerging Technologies; Materials: Genetics to*

Structures; Safety Engineering and Risk Analysis, American Society of Mechanical Engineers, Nov. 2016. doi: 10.1115/IMECE2016-67641.

[136] V. Kadam, S. Kumar, A. Bongale, S. Wazarkar, P. Kamat, and S. Patil, "Enhancing Surface Fault Detection Using Machine Learning for 3D Printed Products," *Applied System Innovation*, vol. 4, no. 2, p. 34, May 2021, doi: 10.3390/asi4020034.

[137] M. A. Ansari, A. Crampton, R. Garrard, B. Cai, and M. Attallah, "A Convolutional Neural Network (CNN) classification to identify the presence of pores in powder bed fusion images," *The International Journal of Advanced Manufacturing Technology*, vol. 120, no. 7–8, pp. 5133–5150, Jun. 2022, doi: 10.1007/s00170-022-08995-7.

[138] J. A. Choren, S. M. Heinrich, and M. B. Silver-Thorn, "Young's modulus and volume porosity relationships for additive manufacturing applications," *J Mater Sci*, vol. 48, no. 15, pp. 5103–5112, Aug. 2013, doi: 10.1007/s10853-013-7237-5.

[139] M. Isida and H. Igawa, "Analysis of a zig-zag array of circular holes in an infinite solid under uniaxial tension," *Int J Solids Struct*, vol. 27, no. 7, pp. 849–864, 1991, doi: 10.1016/0020-7683(91)90020-G.

[140] L. J. Gibson and M. F. Ashby, "The mechanics of three-dimensional cellular materials," *Proceedings of the Royal Society of London. A. Mathematical and Physical Sciences*, vol. 382, no. 1782, pp. 43–59, Jul. 1982, doi: 10.1098/rspa.1982.0088.

[141] Z. L. Zhang, C. Thaulow, and J. Ødegård, "A complete Gurson model approach for ductile fracture," *Eng Fract Mech*, vol. 67, no. 2, pp. 155–168, Sep. 2000, doi: 10.1016/S0013-7944(00)00055-2.

[142] Luiz. A. B. da Cunda and G. J. Creus, "Mechanical Response of Porous Materials: The Gurson Model," 2014, pp. 349–376. doi: 10.1007/978-3-642-40945-5_6.

[143] J. D. Eshelby, "The determination of the elastic field of an ellipsoidal inclusion, and related problems," *Proc R Soc Lond A Math Phys Sci*, vol. 241, no. 1226, pp. 376–396, Aug. 1957, doi: 10.1098/rspa.1957.0133.

[144] J. D. Eshelby, "The elastic field outside an ellipsoidal inclusion," *Proc R Soc Lond A Math Phys Sci*, vol. 252, no. 1271, pp. 561–569, Oct. 1959, doi: 10.1098/rspa.1959.0173.

[145] W. H. Duckworth, "Precise Tensile Properties of Ceramic Bodies," *Journal of the American Ceramic Society*, vol. 34, no. 1, pp. 1–9, Jun. 2006, doi: 10.1111/j.1542-734X.1998.00089.x-i1.

[146] R. M. Spriggs, "Expression for Effect of Porosity on Elastic Modulus of Polycrystalline Refractory Materials, Particularly Aluminum Oxide," *Journal of the American Ceramic Society*, vol. 44, no. 12, pp. 628–629, Dec. 1961, doi: 10.1111/j.1151-2916.1961.tb11671.x.

[147] J. M. Dewey, "The Elastic Constants of Materials Loaded with Non-Rigid Fillers," *J Appl Phys*, vol. 18, no. 6, pp. 578–581, Jun. 1947, doi: 10.1063/1.1697691.

[148] J. C. Wang, "Young's modulus of porous materials," *J Mater Sci*, vol. 19, no. 3, pp. 809–814, Mar. 1984, doi: 10.1007/BF00540452.

[149] A. S. Wagh, J. P. Singh, and R. B. Poeppel, "Dependence of ceramic fracture properties on porosity," *J Mater Sci*, vol. 28, no. 13, pp. 3589–3593, 1993, doi: 10.1007/BF01159841.

[150] C. T. Herakovich and S. C. Baxter, "Influence of pore geometry on the effective response of porous media," *J Mater Sci*, vol. 34, no. 7, pp. 1595–1609, 1999, doi: 10.1023/A:1004528600213.

[151] C. W. Bert, "Prediction of elastic moduli of solids with oriented porosity," *J Mater Sci*, vol. 20, no. 6, pp. 2220–2224, Jun. 1985, doi: 10.1007/BF01112307.

[152] N. Ramakrishnan and V. S. Arunachalam, "Effective elastic moduli of porous solids," *J Mater Sci*, vol. 25, no. 9, pp. 3930–3937, Sep. 1990, doi: 10.1007/BF00582462.

[153] L. Wang and K. K. Tseng, "A multi-scale framework for effective elastic properties of porous materials," *J Mater Sci*, vol. 38, no. 14, pp. 3019–3027, 2003, doi: 10.1023/A:1024736105732.

[154] G. D. McAdam, "Some relations of powder characteristics to the elastic modulus and shrinkage of sintered ferrous compacts," *J. Iron Steel Inst.*, vol. 168, pp. 346–358, 1951.

[155] R. B. Martin and R. R. Haynes, "Confirmation of Theoretical Relation Between Stiffness and Porosity in Ceramics," *Journal of the American Ceramic Society*, vol. 54, no. 8, pp. 410–411, Aug. 1971, doi: 10.1111/j.1151-2916.1971.tb12333.x.

[156] Z. Hashin, "The Elastic Moduli of Heterogeneous Materials," *J Appl Mech*, vol. 29, no. 1, pp. 143–150, Mar. 1962, doi: 10.1115/1.3636446.

[157] M. Almutahhar, K. Al-Athel, J. Albinmousa, and U. Ali, “Computational Modeling and Experimental Investigation of Additively Manufactured Fused Deposition Modeling Samples with In-Built Porosity,” 2024, pp. 213–223. doi: 10.1007/978-3-031-50349-8_20.

[158] T. Sheikh and K. Behdinan, “The effect of process parameters on the mechanical properties of additively manufactured parts using a hierarchical multiscale model,” *Rapid Prototyp J*, vol. 29, no. 5, pp. 1029–1043, May 2023, doi: 10.1108/RPJ-08-2022-0248.

[159] M. S. Anoop and P. Senthil, “Homogenisation of elastic properties in FDM components using microscale RVE numerical analysis,” *Journal of the Brazilian Society of Mechanical Sciences and Engineering*, vol. 41, no. 12, p. 540, Dec. 2019, doi: 10.1007/s40430-019-2037-8.

[160] L. Sánchez-Balanzar, F. Velázquez-Villegas, L. Ruiz-Huerta, and A. Caballero-Ruiz, “A multiscale analysis approach to predict mechanical properties in fused deposition modeling parts,” *The International Journal of Advanced Manufacturing Technology*, vol. 115, no. 7–8, pp. 2269–2279, Aug. 2021, doi: 10.1007/s00170-021-07287-w.

[161] P. Ferretti, G. M. Santi, C. Leon-Cardenas, E. Fusari, G. Donnici, and L. Frizziero, “Representative Volume Element (RVE) Analysis for Mechanical Characterization of Fused Deposition Modeled Components,” *Polymers (Basel)*, vol. 13, no. 20, p. 3555, Oct. 2021, doi: 10.3390/polym13203555.

[162] Wang, Zhao, Fuh, and Lee, “Effect of Porosity on Mechanical Properties of 3D Printed Polymers: Experiments and Micromechanical Modeling Based on X-Ray Computed Tomography Analysis,” *Polymers (Basel)*, vol. 11, no. 7, p. 1154, Jul. 2019, doi: 10.3390/polym11071154.

[163] F. Ferrano, T. Wachter, M. Fateri, and M. Schmiedt, “Process-Structure Coupled Simulation of Additive Manufactured Components,” *Polymers (Basel)*, vol. 15, no. 4, p. 949, Feb. 2023, doi: 10.3390/polym15040949.

[164] T. Webbe Kerekes, H. Lim, W. Y. Joe, and G. J. Yun, “Characterization of process–deformation/damage property relationship of fused deposition modeling (FDM) 3D-printed specimens,” *Addit Manuf*, vol. 25, pp. 532–544, Jan. 2019, doi: 10.1016/j.addma.2018.11.008.

[165] G. Vastola, Q. X. Pei, and Y.-W. Zhang, “Predictive model for porosity in powder-bed fusion additive manufacturing at high beam energy regime,” *Addit Manuf*, vol. 22, pp. 817–822, Aug. 2018, doi: 10.1016/j.addma.2018.05.042.

[166] P. Parandoush and D. Lin, “A review on additive manufacturing of polymer-fiber composites,” *Compos Struct*, vol. 182, pp. 36–53, Dec. 2017, doi: 10.1016/j.compstruct.2017.08.088.

[167] R. Biswal *et al.*, “Interrupted fatigue testing with periodic tomography to monitor porosity defects in wire + arc additive manufactured Ti-6Al-4V,” *Addit Manuf*, vol. 28, pp. 517–527, Aug. 2019, doi: 10.1016/j.addma.2019.04.026.

[168] Inc. Raise 3D Technologies, “Raise3D Premium PLA Technical Data Sheet,” https://www.raise3d.com/products/raise3d-premium-pla-filament/.

[169] M. T. Birosz, D. Ledenyák, and M. Andó, “Effect of FDM infill patterns on mechanical properties,” *Polym Test*, vol. 113, p. 107654, Sep. 2022, doi: 10.1016/j.polymertesting.2022.107654.

[170] A. P. Agrawal, V. Kumar, J. Kumar, P. Paramasivam, S. Dhanasekaran, and L. Prasad, “An investigation of combined effect of infill pattern, density, and layer thickness on mechanical properties of 3D printed ABS by fused filament fabrication,” *Heliyon*, vol. 9, no. 6, p. e16531, Jun. 2023, doi: 10.1016/j.heliyon.2023.e16531.

[171] C. Basaran, “Stress and Strain in Continuum,” in *Introduction to Unified Mechanics Theory with Applications*, Cham: Springer International Publishing, 2021, pp. 5–71. doi: 10.1007/978-3-030-57772-8_2.

[172] F. Hartmann, “The Derivation of Stiffness Matrices from Integral Equations,” in *Boundary Element Methods*, Berlin, Heidelberg: Springer Berlin Heidelberg, 1981, pp. 552–566. doi: 10.1007/978-3-662-11270-0_35.

[173] V. V. Mehtre, “Review on Newton Raphson Method,” *Int J Res Appl Sci Eng Technol*, vol. 7, no. 11, pp. 669–671, Nov. 2019, doi: 10.22214/ijraset.2019.11107.

[174] D. Rodrigues, J. Belinha, R. N. Jorge, and L. Dinis, “Development of a Constitutive Model to Predict the Elasto-Plastic Behaviour of 3D-Printed Thermoplastics: A Meshless Formulation,” 2020, pp. 311–329. doi: 10.1007/978-3-030-44522-5_10.

[175] F. Bandinelli, L. Peroni, and A. Morena, “Elasto-Plastic Mechanical Modeling of Fused Deposition 3D Printing Materials,” *Polymers (Basel)*, vol. 15, no. 1, p. 234, Jan. 2023, doi: 10.3390/polym15010234.

[176] D. Mrozik and Ł. Pejkowski, “Tensile constitutive behavior modeling of 3D printed polylactide (PLA) using visco-elastic-visco-plastic model,” 2023, p. 020018. doi: 10.1063/5.0165536.

[177] J. Torres, J. Cotelo, J. Karl, and A. P. Gordon, “Mechanical Property Optimization of FDM PLA in Shear with Multiple Objectives,” *JOM*, vol. 67, no. 5, pp. 1183–1193, May 2015, doi: 10.1007/s11837-015-1367-y.

[178] M. Kasim Mehdi and B. Owed, “The Influence of Infill Density and Speed of Printing on The Tensile Properties of The Three Dimension Printing Polylactic Acid Parts,” *Journal of Engineering and Sustainable Development*, vol. 27, no. 1, pp. 95–103, Jan. 2023, doi: 10.31272/jeasd.27.1.8.

[179] K. I. Ismail, T. C. Yap, and R. Ahmed, “3D-Printed Fiber-Reinforced Polymer Composites by Fused Deposition Modelling (FDM): Fiber Length and Fiber Implementation Techniques,” *Polymers (Basel)*, vol. 14, no. 21, p. 4659, Nov. 2022, doi: 10.3390/polym14214659.

[180] X. Sun, M. Mazur, and C.-T. Cheng, “A review of void reduction strategies in material extrusion-based additive manufacturing,” *Addit Manuf*, vol. 67, p. 103463, Apr. 2023, doi: 10.1016/j.addma.2023.103463.

[181] D. Godec, K. Križetić, and A. Pilipović, “Influence of Infill Pattern on 3D-Printed Parts Compression Strength,” *Tehnički glasnik*, vol. 16, no. 3, pp. 315–319, Jun. 2022, doi: 10.31803/tg-20220413112955.

[182] L. Lopes, D. Reis, A. Paula Junior, and M. Almeida, “Influence of 3D Microstructure Pattern and Infill Density on the Mechanical and Thermal Properties of PET-G Filaments,” *Polymers (Basel)*, vol. 15, no. 10, p. 2268, May 2023, doi: 10.3390/polym15102268.

[183] F. Ning, W. Cong, Y. Hu, and H. Wang, “Additive manufacturing of carbon fiber-reinforced plastic composites using fused deposition modeling: Effects of process parameters on tensile properties,” *J Compos Mater*, vol. 51, no. 4, pp. 451–462, Feb. 2017, doi: 10.1177/0021998316646169.

[184] H. Gonabadi, A. Yadav, and S. J. Bull, “The effect of processing parameters on the mechanical characteristics of PLA produced by a 3D FFF printer,” *The International Journal of Advanced Manufacturing Technology*, vol. 111, no. 3–4, pp. 695–709, Nov. 2020, doi: 10.1007/s00170-020-06138-4.

[185] M. Cao *et al.*, “Preparation and Characterization for the Thermal Stability and Mechanical Property of PLA and PLA/CF Samples Built by FFF Approach,” *Materials*, vol. 16, no. 14, p. 5023, Jul. 2023, doi: 10.3390/ma16145023.

[186] X. Zhang, L. Chen, T. Mulholland, and T. A. Osswald, “Characterization of mechanical properties and fracture mode of PLA and copper/PLA composite part

manufactured by fused deposition modeling," *SN Appl Sci*, vol. 1, no. 6, p. 616, Jun. 2019, doi: 10.1007/s42452-019-0639-5.

[187] J. Martínez, J. L. Diéguez, E. Ares, A. Pereira, P. Hernández, and J. A. Pérez, "Comparative between FEM Models for FDM Parts and their Approach to a Real Mechanical Behaviour," *Procedia Eng*, vol. 63, pp. 878–884, 2013, doi: 10.1016/j.proeng.2013.08.230.

[188] P. Baikerikar and C. J. Turner, "Comparison of FEA simulations and experimental results for as-built additively manufactured dogbone specimens," *The International Journal of Advanced Manufacturing Technology*, vol. 115, no. 9–10, pp. 2839–2851, Aug. 2021, doi: 10.1007/s00170-021-07307-9.

[189] S. Anand Kumar and Y. Shivraj Narayan, "Tensile Testing and Evaluation of 3D-Printed PLA Specimens as per ASTM D638 Type IV Standard," 2019, pp. 79–95. doi: 10.1007/978-981-13-2718-6_9.

VITAE

Name	**:** Mosa Eissa Almutahhar
Nationality	**:** Saudi
Date of Birth	**:** 7/19/1996
Email	**:** mosa.almutahhar@gmail.com
Address	**:** 7125 Doha Dist., Dhahran, PO.Box. 34452, Saudi Arabia
Academic Background	**:**
Jan 2015 – May 2019	BSc. in Mechanical Engineering, King Fahd University of Petroleum & Minerals, Dhahran, Saudi Arabia.
Industrial Experience	**:**
Oct 2019 – Sep 2021	Field Engineer, Testing & Subsea Department, Halliburton Energy Services Inc, Dammam, Saudi Arabia.
Research Experience	**:**
Aug 2022 – May 2024	Research Assistant, Rapid Prototyping and Reverse Engineering Lab, King Fahd University of Petroleum & Minerals, Dhahran, Saudi Arabia.

May 2022 – July 2022 Summer Research Intern, Clean Combustion Research Center, King Abdullah University of Science and Technology, Thuwal, Saudi Arabia.

Publications **:**

M. Almutahhar, K. Al-Athel, J. Albinmousa, U. Ali (2024). Computational Modeling and Experimental Investigation of Additively Manufactured Fused Deposition Modeling Samples with In-Built Porosity. TMS 2024 153rd Annual Meeting & Exhibition Supplemental Proceedings. The Minerals, Metals & Materials Series. DOI:10.1007/978-3-031-50349-8_20.

M. Almutahhar, A. Alhajeri, R. A. Laghari, S. S. Akhtar, U. Ali (2023) Prediction of tool failure in metal hot extrusion process using artificial neural networks. Materials Research Proceedings, Vol. 36. DOI:10.21741/9781644902790-2.

A. S. Mohammed, M. Almutahhar et al. (2023) Deep learning based porosity prediction for additively manufactured laser powder-bed fusion parts. JMR&T DOI:10.1016/j.jmrt.2023.11.130.

A. Alhajeri, O. Aremu, M. Almutahhar et al. (2024). On the effect of loading and printing parameters that influence the fatigue behavior of laser powder-bed fusion additively manufactured steels. Heliyon. DOI:10.1016/j.heliyon.2024.e29229.